

國立交通大學

應用化學系博士班

博士論文

生物官能基化奈米鑽石性質及其應用

Properties of Bio-functionalized Nanodiamond and Its
Applications

研究生：劉昱麟

指導教授：孫建文 博士

中華民國一百年九月

生物官能基化奈米鑽石性質及其應用

Properties of Bio-functionalized Nanodiamond and Its
Applications

研究生：劉昱麟

Student : Yu-Lin Liu

指導教授：孫建文 博士

Advisor : Dr. Kien-Wen Sun



A Thesis Submitted to Ph.D program, Department of Applied Chemistry
College of Science National Chiao Tung University
in Partial Fulfillment of the Requirements
for the Degree of Doctor of Philosophy
in
Applied Chemistry
September 2011
Hsinchu, Taiwan, Republic of China

中華民國 一 百 年 九 月

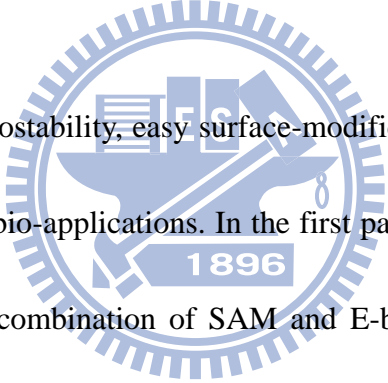
Properties of Bio-functionalized Nanodiamond and Its Applications

Student: Yu-Lin Liu

Advisor: Dr. Kien-wen Sun

Ph.D program, Department of Applied Chemistry
National Chiao Tung University

Abstract

The logo of National Chiao Tung University is a circular emblem. It features a central shield with a book, a lamp, and a gear. The year '1896' is inscribed at the bottom of the shield. The entire emblem is surrounded by a gear-like border.

Diamond with good photostability, easy surface-modification, and low cytotoxicity is a good nanomaterial for bio-applications. In the first part of this thesis, we develop a new technique which is combination of SAM and E-beam lithography to pattern nanodiamond on silicon base substrate. The technique which we demonstrated here is suitable for applications of bio-sensing chips and single bio-molecule patterning and detection. For the further works, we expect to develop for bio-chip base on bio-functionalized nanodiamond arrays.

In the second part of this thesis, we couple nanodiamond with gold nanoparticles of different sizes by using two complementary DNA sequences. After the gold nanoparticles were hybridized on the nanodiamonds, we observed enhancement of the photoluminescence (PL) signals originated from nanodiamond's nitrogen-vacancy

center. The enhancement was attributed to the plasmon field created by the gold nanoparticles. The shape of the enhanced PL spectra was also affected by the sizes of the attached nanoparticles due to their different resonant plasma frequency. The signal enhancement can be used as an indexing tool for bio-sensing purposes.



致謝

在交通大學五年多的博士生涯即將告一個段落，在這五年多的日子之中，一轉眼間就到了結束的時候，不管是生活上以及學業上，都受到許多人的幫助以及照顧，在此感謝所有對我有幫助的人。

首先，我要感謝我的指導教授孫建文教授，在研究上老師總是給我們很大的自由及發揮度，去激發出獨立思考以及解決問題的能力，並提供我們沒有後顧之憂的研究環境，並且在實驗上適時的給予指導，在最後不管是期刊還是論文給予適當的建議。

另外，我要感謝林諭男教授、張立教授、孫允武教授、黃振昌教授、廖奕翰教授，在百忙之中抽空擔任我的口試委員。

接著我要感謝奈米科技的工作人員們，感謝李良箴博士在不吝嗇的傳授實驗上的技術，使得我的實驗可以更輕易的完成。劉翊筑小姐，在許多的公務以及生活事務上給予大力的幫忙，另外還有徐武達先生、鍾宜娟小姐、賴良一先生...等，給予實驗上以及生活事務的幫助。

還有要感謝孫建文實驗室的伙伴們，克瑜、鏡堯、承翰，雖然跟你們自一起做實驗的時間不常，但是從一開始的盡心盡力儀器的教學，以及實驗室事務上的幫助。昭凱，感謝你在實驗上大力的幫忙、從一開始的 PECVD 以及後來的 FIB... 等的製程上都給予很大的幫忙，還

有在資格考上指點一條明路。以及老柯，在使用 Confocal、E-GUN 以及 PECVD... 等儀器上以及在理論的討論上給予很大的幫助。感謝昭凱與老柯在我博班生涯中一起相互努力成長。

還有實驗室其他的學弟妹，柏帆、宇涵及詩翔，感謝你們陪我一起掉進奈米鑽石這一條不歸路。政元除了在實驗上的幫忙之外。在球場上一起揮殺灑的日。子漢、建宏(KB)、忠儀、庭源(龍五)、晟嘉、琇雅、靜宜、文駿、志昇、新欽、夢勳、學亨、允中... 等其他學弟妹、在這五年的博士生活感謝與我一同成長

還有感謝在實驗上幫忙的實驗室: 交大應化李耀坤實驗室、交大電子李建平實驗室、中原物理沈志霖實驗室、交大生物張家靖實驗... 等。

還有感謝我的女朋友俊儀，感謝妳一路以來的包容與陪伴。

最後感謝我的父母，感謝他們一路的支持與關心，你們是支持我的一大力量。

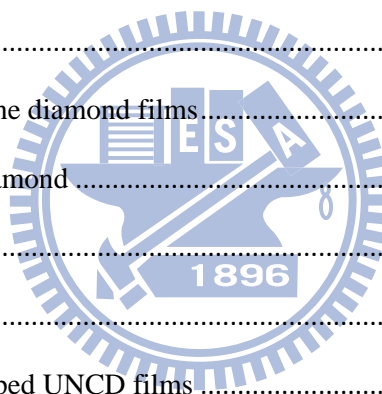
有太多太多的感謝是無法用筆墨寫出的，這一刻我只能用最簡單的文字，來回謝這些默默在我背后支持的你們，感謝你們。

Content

Abstract	I
致謝	III
Content	V
List of Figure	VIII
Chapter 1 Introduction and Background	1
1-1 Diamond	1
1-2 Synthesize of diamond	2
1-2-1 HTHP (high temperature and high pressure) diamond	2
1-2-2 CVD (chemical vapor deposition) diamond	3
1-2-3 Detonation of explosive	4
1-2-4 Ultrasound cavitation	5
1-3 Impurities in diamond	5
1-3-1 Classification of diamond	6
1-3-2 Analysis of defects in diamond	7
1-3-3 Color center of diamond	9
1-4 Application of diamond	12
1-4-1 Nanodiamond as bio-marks	12
1-4-2 CVD diamond for bio-chip applications	14
1-4-3 Diamond for Single-photon source	15
1-5 Research motivation and object	16
1-6 Reference	17
Chapter 2 Skeleton of this thesis and instrumentation	27
2-1 Description of the remaining chapters	27
2-1-1 Protein Functionalized Nanodiamond Arrays	27
2-1-2 Plasmon-enhanced photoluminescence from bioconjugated gold nanoparticle and nanodiamond assembly	28

2-2 Instrumentation	28
2-2-1 E-beam lithography.....	28
2-2-2 Confocal microscopes.....	29
2-2-3 Raman spectrum	30
2-2-4 Luminescence	32
2-3 Reference	34
Chapter 3 Application of bio-functionalized nanodiamond arrays.....	40
3-1 Literature review	40
3-1-1 Nanodiamond.....	40
3-1-2 Bio-chip	41
3-2 Fabrication of bio-functionalized nanodiamond arrays by self assemble monolayer .	43
3-2-1 Preparation of carboxylated nanodiamond solution	43
3-2-2 Fabrication of nanodiamond nanoarray by self assemble monolayer	44
3-2-3 Fabrication of PLL and FITC functionalized nanodiamond nanoarray	46
3-2-4 Fabrication of Lysozyme functionalized nanodiamond arrays	46
3-3 Results and discussion.....	47
3-3-1 Carboxylated nanodiamond	47
3-3-2 Nanodiamond nanoarray.....	48
3-3-3 PLL and FITC functionalized nanodiamond arrays.....	50
3-3-4 Lysozyme functionalized nanodiamond arrays	51
3-4 Summary	53
3-5 Reference	54
Chapter 4 Photoluminescence enhancement of bioconjugated gold nanoparticle and nanodiamond assembly	71
4-1 Literature review	71
4-2 Fabrication of bioconjugated gold nanoparticle and nanodiamond assembly.....	72
4-2-1 Preparation of nano assembly	72

4-2-2 Conjugation of gold nanoparticle with nanodiamond.....	74
4-3 Results and discussion.....	75
4-3-1 Gold nanoparticle and nanodiamond assembly	75
4-3-2 Optical properties.....	77
4-3-3 Photoluminescence enhancement of Au-DNA-ND assembly	78
4-4 Summary	82
4-5 Reference	82
Chapter 5 Conclusion	96
Publications	97
Appendix-Fluorescent defect centers in nitrogen-doped ultrananocrystalline diamond films generated by microwave plasma	98
A-1 Literature review	98
A-1-1 Ultrananocrystalline diamond films.....	98
A-1-2 Semiconductor diamond	99
A-1-3 Ion implantation.....	100
A-1-4 Silicon vacancies.....	102
A-2 Growth of nitrogen-doped UNCD films	103
A-3 Properties of nitrogen-doped UNCD films	104
A-4 Properties of nitrogen-doped UNCD films treated with microwave plasma.....	106
A-5 Summary	112
A-6 Reference.....	113



List of Figure

Figure 1-1(a): Raman spectra of three different CVD diamond films	24
Figure 1-1(b): The different spectra of various wavelength of laser excitation of diamond	24
Figure 1-2: Raman spectra of nanodiamonds of different size	25
Figure 1-3 (a): Photoluminescence spectra of different sizes nanodiamonds obtained by using 488nm laser excitation.....	25
Figure 1-3(b): Photoluminescence spectra of different sizes nanodiamonds obtained by using 532nm laser excitation.....	26
Figure 2-1: Overlay of electron beam system and the electron optical column of electron beam system.....	35
Figure 2-2: Illustration and simulation result of forward and back scattering effect and the charge effect during the electron beam process	36
Figure 2-3: Illumination of confocal microscope	37
Figure 2-4: Energy diagram for Rayleigh, Stokes, and anti-Stokes scattering	38
Figure 2-5: Simplified Jablonski diagram with absorbance, internal conversion, fluorescence, intersystem crossing, and phosphorescence	39
Figure 3-1: Cytotoxicity test of nanodiamonds	57
Figure 3-2: Photostability test of nanodiamond.....	57
Figure 3-3: Synthetic route for functionalized nanodiamonds	58
Figure 3-4: Electric properties of surface modified silicon nanowire were changed under the variation of pH value	58
Figure 3-5 (a): Schematics of the functionalized NDs bonded to the SAM substrates.....	59
Figure 3-5 (b): Schematics of flow chart of the template fabrication processes	59
Figure 3-6: Schematic proceeding of the FITC functionalized NDs	60
Figure 3-7 (a): Raman spectra of NDs with and without the acid treatment	61
Figure 3-7 (b): Raman spectra of NDs with and without the acid treatment	61
Figure 3-8: FTIR spectra of NDs with and without the acid treatment	62
Figure 3-9 (a): SEM images of one of the corners of the cross marks	63
Figure 3-9(b): SEM images of the nano holes array	63
Figure 3-10(a): SEM images of the cross-section of a patterned single	

nanodiamond.....	64
Figure 3-10(b): AFM images of patterned single nanodiamond arrays.....	64
Figure 3-11(a): Raman spectra of pattern-in and pattern-out area.....	65
Figure 3-11(b): PL spectra of pattern-in and pattern-out area.....	65
Figure 3-12(a): Optical image of the nanodiamond arrays of 1D mapping area, indicated by the straight line.....	66
Figure 3-12(b): Image of the 1D Raman intensity mapping.....	66
Figure 3-13(a): Optical image of nanodiamond arrays of the 2D mapping area, indicated by the square.....	67
Figure 3-13(b): Image of the 2D Raman intensity mapping.....	67
Figure 3-14(a): Optical image of the 1D mapping area, indicated by the straight line.....	68
Figure 3-14(b): Image of the 2D PL intensity mapping.....	68
Figure 3-15: IR spectra of three different samples (a) cND (b) lysozyme and (c) cND-lysozyme chip.....	69
Figure 3-16: Raman spectra of three different samples (a) lysozyme (b) lysozyme-cND complex in the solution (c) cND-lysozyme chip.....	69
Figure 3-17(a): SEM images of E.coli interaction with ND-lysozyme film on crossmark.....	70
Figure 3-17(b): SEM images of E.coli interaction with ND-lysozyme film on nanoarrays.....	70
Figure 4-1: ICG dye molecules were enhanced by metallic nanoparticles..	86
Figure 4-2: Spectra of Healthview Nucleic Acid Stain, and ND-DNA1 and Au-DNA2 solutions were allowed to react with Healthview Nucleic Acid Stain.....	86
Figure 4-3: Scheme of conjugation gold nanoparticle and nanodiamond by DNA.....	87
Figure 4-4(a): SEM images of the hybrid structures of NDs coupled with the 13 nm gold nanoparticles,.....	87
Figure 4-4(b): SEM images of the hybrid structures of NDs coupled with the 30 nm gold nanoparticles,.....	88
Figure 4-4(c): SEM images of the hybrid structures of NDs coupled with the 50 nm gold nanoparticles,.....	88
Figure 4-4(d): SEM images of the hybrid structures of NDs coupled with the 80 nm gold nanoparticles,.....	89
Figure 4-5: SEM image of NDs interacted with gold nanoparticles without DNA.....	89
Figure 4-6: HRTEM image of a 30 nm gold nanoparticle attached on a ND	

via a double string DNA	90
Figure 4-7(a): PL spectra of bare ND, gold nanoparticles, Au-DNA2 assembly, and ND-DNA1 assembly	90
Figure 4-7(b): Absorption spectra of 13nm, 30nm, 50nm, and 80nm Au nanoparticles	91
Figure 4-8(a): Plasmon enhanced PL spectra of Au-DNA-ND hybrid structures with gold nanoparticle sizes of 13 nm.....	91
Figure 4-8(b): Plasmon enhanced PL spectra of Au-DNA-ND hybrid structures with gold nanoparticle sizes of 30 nm.....	92
Figure 4-8(c): Plasmon enhanced PL spectra of Au-DNA-ND hybrid structures with gold nanoparticle sizes of 50 nm.....	92
Figure 4-8(d): Plasmon enhanced PL spectra of Au-DNA-ND hybrid structures with gold nanoparticle sizes of 80 nm.....	93
Figure 4-9: Scheme of interaction between hybrid structures and NdeI restriction enzyme.....	93
Figure 4-10: SEM image of hybrid structures interact with the NdeI restriction enzyme.....	94
Figure 4-11: PL spectra of bare ND, Au-DNA-ND hybrid structures before and after interacting with NdeI restriction enzyme.....	94
Figure 4-12: Time-resolved spectra of bare NDs, ND-DNA1 assembly, and Au-DNA-ND hybrid structures.....	95
Figure A-1: Conductivity data obtained in the temperature range 300–4.2 K for a series of films synthesized using different nitrogen concentrations.	120
Figure A-3: Silicon vacancies generated by ion implantation	120
Figure A-3: Neutral vacancy was formed after nitrogen ion implantation. Then annealing the neutral vacancy is converted into nitrogen vacancy.	121
Figure A-4: HRTEM image of the N-doped UNCD.....	122
Figure A-5: Raman spectra of UNCD and nitrogen doping UNCD	122
Figure A-6(a): EDS spectrum which the electron beam aims at the grain boundaries	123
Figure A-6(b): EDS spectrum which the electron beam aims at the grains	123
Figure A-7: TEM image of the nitrogen doping UNCD after treated by microwave plasma	124
Figure A-8: Raman spectra of (a) nitrogen doping UNCD and nitrogen doping UNCD treated by microwave plasma with (a) microwave	

power of 800W and total pressure of 10Torr (b) over high microwave power and total pressure	124
Figure A-9(a): EDS spectrum of sample A	125
Figure A-9(b): EDS spectrum of sample B	125
Figure A-10(a): SIMS spectrum of sample A	126
Figure A-10(b): SIMS spectrum of sample B	126
Figure A-11: Photoluminescence spectra of nitrogen doping UNCD, sample A. and sample B which both treated by microwave plasma	127
Figure A-12 (a): SEM image of the slope generated by Focus ion beam ..	127
Figure A-12 (b): Photoluminescence intensity of Si-V traced at 738nm...	128
Figure A-12 (c): Photoluminescence intensity of Si-V traced between 550nm and 650nm.....	128



Chapter 1 Introduction and Background

1-1 Diamond

The diamond crystal is formed by SP^3 -bonding structured carbon atoms. There are two face-centered cubic lattices in the diamond lattice shifted by a vector $(a/4, a/4, a/4)$. The lattice parameter a is 3.56683\AA . Diamond has the greatest number density, i.e. atoms per unit volume, of any known substance. This combined with the strength of the carbon-carbon bond, giving rise to an extraordinarily high bond energy density. Therefore, diamond exhibits extremely mechanical properties. Diamond is known as the hardest natural materials scoring 10 on old Mohs scale of mineral hardness [1.1]. The high bonding energy density also leads to good chemical stability for resisting most acid and alkalis. Unlike most electrical insulators, pure diamond shows good thermal conductivity which can reach up to 20W/cm-K at room temperature [1.2]. The thermal conductivity of pure diamond which is roughly four times more higher than copper is the highest of any known solid and excellent insulator with conductivity about $10^{15}\ \Omega\text{-cm}$ [1.3]. Diamond can also be treated as semiconductor with a wide band gap of 5.45eV . Due to the wide band gap, diamond has high optical transmissivity around $>95\%$ from deep UV to far IR. The wide band gap grants diamond a very low or negative electron affinity; hence, it is then able to emit

electrons from its surface with very little applied voltage.

1-2 Synthesize of diamond

1-2-1 HTHP (high temperature and high pressure) diamond

In 1954, Hall and his co-workers in General Electric (GE) achieved their first commercially successful synthesis of diamond under HPHT (high pressure and high temperature) where diamond is a more stable form than graphite [1.4, 1.5]. Their breakthrough was to use a belt press which was capable to produce the pressure over 10 GPa and temperature above 2000°C. Because of the large activation energy required for breaking carbon-carbon bonds, graphite is not necessarily transformed into diamond, even under high pressure and temperature [1.6, 1.7]. The molten iron, nickel or cobalt which acted as solvent-catalyst was dissolved in graphite and accelerated its conversion into diamond. In addition, the morphology of the grown crystals is determined by the pressure and temperature. Furthermore, the growth rate of diamond depends on the solubility of carbon on graphite-metal and metal-graphite interface. Therefore the concerns for the features of the stable HPHT conditions were kept to grow high-quality diamonds. The mass-production and high-quality diamond crystals make the HPHT process a more suitable choice for industrial applications.

1-2-2 CVD (chemical vapor deposition) diamond

In the 1950s, a domain of research performed in the Soviet Union and U.S. focused on pyrolysis of hydrocarbon gases at the relatively low temperature at 800°C. This low-pressure process is known as chemical vapor deposition (CVD). Since the early 1980s, this method has been the subject of intensive worldwide research. The advantages of CVD diamond growth include the ability to produce diamond over large areas and on various substrates, and its well control over chemical impurities. The CVD process does not require pressure as high as HPHT.

To activate the carbon-containing precursor molecules in the CVD process, the gas typically must reach a temperature exceeding 2000°C. To achieve this target, several techniques can be employed, including hot filament, plasma-assisted (DC or microwave), combustion flame, and so on activation. Because hot-filament CVD is a simple growth method, it has been widely accepted among diamond researchers in the early stages of research [1.8, 1.9].

The crucial fact for the growth rate and crystal quality is not only the gas temperature, but also the gas composition, which typically use the mixture of CH₄ and H₂. During the diamond growth which is under low pressure, the graphite phases are formed on the growth surface in a certain amount which is in accordance with the diamond phases. Consequently, the graphite must be removed effectively to continue

the diamond CVD. For keeping the diamond phase stable, the atomic hydrogen has gotten the function to etch the graphite phases selectively. The carbon source gas must therefore be highly diluted with hydrogen. The hydrogen atoms which are characteristic of diamond CVD under low pressure are believed to play crucial roles in the process.

Depending on the types of substrate, there are two principal synthesis varieties: the growth of diamond on diamond (homoepitaxy) and on non-diamond substrate (heteroepitaxy). Homoepitaxy growth results in monocrystalline layers with superior properties. However, the growth rate is slow due to the low surface chemical activity of diamond. Additionally, the diamond substrate is expensive and limited in size. In the growth of heteroepitaxy, films may consist of oriented or non-oriented grains. They contain numerous defects, like grain boundaries and amorphous carbon, but can be grown to large sizes.

1-2-3 Detonation of explosive

The explosive detonation is the other method of diamond synthesis. The technology was based on the detonation transformation of carbon-containing explosives with negative oxygen balance. The product is a mixture of different kinds of carbon, carbon black, etc; the major product among them is ultra-dispersed diamond (UDD) powder which consists of highly defective structure and an active surface with special

absorption ability and high reacting capacity [1.10]. Nevertheless, it is not able to control the production more precisely in diamond size.

1-2-4 Ultrasound cavitation

Micron-sized diamond crystals can be synthesized from a suspension of graphite, which is in the organic liquid at atmospheric pressure and room temperature, by using ultrasonic cavitation. The diamond yield is about 10% of the initial graphite weight. The estimated cost of diamond produced by this method is comparable to the HPHT method; the crystalline perfection of the product is significantly worse to the ultrasonic synthesis. This technique requires relatively simple equipments and procedures, however, it has only been reported by two research groups, and has no industrial use as of 2009 [1.11]. Numerous process parameters are not yet optimized, such as, the preparation of the initial graphite powder, the choice of ultrasonic power, synthesis time and the solvent. However, it does leave a route for potential improvement of the efficiency and reduction of the cost of the ultrasonic synthesis.

1-3 Impurities in diamond

Pure diamond crystal is colorless. Colored diamonds contain crystallographic defects, including intrinsic defects and impurity-related defects, which cause the

coloration. Intrinsic defects include vacancies, interstitials and extended structural defects. Small foreign elements, such as nitrogen and boron, can appear as single atoms at lattice sites, while large impurity atoms tend to form complexes with other impurities or vacancies. Nevertheless, more than 300 optical centers due to the element H, He, Li, B, N, NE, S, Si, P, Ti, and so on in diamond are documented [1.12].

1-3-1 Classification of diamond

Natural diamond can be typically classified into four types, i.e. Ia, Ib, IIa and IIb, according to the dominant type of defect present. More than 95% of natural diamonds belong to the type Ia. There was the highest concentration of nitrogen (up to 3000 ppm) in type Ia diamond. The aggregative nitrogen present in two major structures of which are the A-center and B-center. The A-center consists of a pair of substitutional nitrogen atoms in nearest neighborhood, while the B-center occurs as a complex of four substitutional nitrogen atoms surrounding a lattice vacancy. The concentration of nitrogen which is ranging between 150 to 600 ppm is still considerable in type Ib diamond. Nitrogen forms dominantly in single-substitutional structure. The single-substitutional nitrogen atoms act as donor centers in diamond. The optical absorption of type I diamonds give rise to slightly yellow color [1.13].

The concentration of nitrogen impurities lower than IR absorption sensitivity (~

1ppm) was defined as type II diamond. The type IIa diamond refers to the purest crystals. Boron is one of the most dominant impurities in type IIb diamond. The only boron related defect is single substitutional acceptor with an energy level 0.37eV above the valence band. Therefore, the type IIb diamond shows P-type conductivity at room temperature. Optical absorption which gives type IIb diamond the characteristic blue color was produced by ionization of the acceptors.

The CVD diamond can contain different impurities, depending on the substrate and mixing reaction gases. This classification is not used in CVD diamond, yet, is used for HPHT synthesis diamond. Nitrogen is the most common contamination in the HPHT synthesis diamond. Most diamond synthesized through the growing process by HPHT is the type Ib. If boron was added into the growth chamber to reduce the concentration of nitrogen, the type IIb diamond can be produced. The high temperature annealing which lead to aggregation of single-substitutional nitrogen converse type Ib into type Ia [1.14].

1-3-2 Analysis of defects in diamond

The Raman spectrum of diamond consists of a sharp peak at 1332cm^{-1} , while graphite gives a rise in the boarder peaks characterized by the D-band at 1350cm^{-1} and the G-band at 1580cm^{-1} . The width of 1332cm^{-1} peak line reveals that how much random stress exists in the diamond [1.15]. The figure 1-1(a) shows the Raman

spectra of three different CVD diamond films. The quality of diamond is clearly distinguishable. The excitation wavelength influenced the results of Raman spectra. The figure 1-1(b) shows the different spectra of various wavelength of laser excitation of diamond. While IR laser was used in Raman measurement, non-diamond components emerge in the spectra due to that the IR laser is more sensitive for SP^2 -bond carbon scattering. If the Raman spectra were measured by UV laser, the fairly good quality can be obtained [1.15].

The surface morphology and structure properties also influenced the results of the Raman spectra. In figure 1-2, Raman spectra of nanodiamonds of different size are presented. For the size of 5-50nm nanodiamond, characteristic D-band and G-band were dominated. For the size of 100-500nm, the intense diamond peak at 1332cm^{-1} exhibited with traceable graphitic or amorphous signature [1.16]. However, for the size larger than 50nm, the structure is usually explained as diamond polycrystal structure with graphitic structure on surface. While the nanodiamond with size 100nm and larger, the Raman spectra have similar characters of bulk diamond which has strong and sharp 1332cm^{-1} peak. For the smaller nanodiamond, the graphitic or amorphous structure dominated the spectra. We observed that nanodiamonds with sizes 100 nm and larger, the Raman spectra have similar characters with sharp and intense diamond peak; while the spectra for 5–50 nm nanodiamonds appear differently.

The same difference was observed in photoluminescence spectra.

Luminescence can be excited by either an electron beam or light. The methods are called cathodoluminescence and photoluminescence, respectively. The Raman scattering is often measured together with photoluminescence. Additionally, electron beam excites different optical centers at the same time, which leads to complications in interpretation of the spectra. By contrast, selective excitation is allowed in PL by choosing proper excitation wavelengths. Figure 1-3 (a) and (b) depicts the photoluminescence spectra of different sizes nanodiamonds obtained by using 488 and 532 nm excitation wavelength, respectively [1.16].

Electron spin resonance (ESR) spectroscopy is a technique for studying chemical species that have one or more unpaired electrons. Unpaired electrons in solids have a non-vanishing spin which is associated with a magnetic moment. Consequently, the spin states have different energies in a magnetic field. Natural and synthetic diamond has been extensively studied by ESR, now, this method is gaining new attention due to the possibility of using the spin states in the defect center to implement a solid state quantum bit at room-temperature [1.17].

1-3-3 Color center of diamond

If the excited and ground states of a defect are both located within the band gap and then an optical dipole transition is allowed between them, this defect is luminescent

under excitation. Those defects give the crystal a characteristic color, and are thus called color centers. A huge variety of optical color centers which maintain more than 100 different color centers can be found in diamond owing to the wide band gap of diamond [1.18].

A very important transition occurs between the levels $M=0$ and $n=0$, it is the zero-phonon line. In absorption, the phonon-assisted transition takes place at energies which is higher than ZPL; in emission, however, it is at lower energies, which leads to a mirror symmetry relative to the ZPL. In addition, the charge states are another important property of the color centers. Generally, different charged states give rise to the complete spectra. In the semiconductors with shallow donors and acceptors, the equilibrium charge state of defects is determined by the position of the Fermi-level.

Nitrogen is the most prominently known impurity, which forms the nitrogen vacancy defect in diamond and it consists of a substitution nitrogen atom with a next nearest neighbor vacancy. According to the impurities which are close to the surrounding area acting as electron donor or acceptor, the defects can form two types of states: neutral nitrogen vacancy center $[(N-V)^0]$ and negative-charged nitrogen vacancy center $[(N-V)^-]$ [1.19-1.22].

The $[(N-V)^-]$ defect in diamond which consists of a substitution nitrogen atom with a next nearest neighbor vacancy is the most dominant defect in irradiated and

annealed type-Ib diamond. The resulting N-V pair has the expected C_{3v} symmetry. It is established that the ground state is spin triplet and the ZPL absorption corresponds to $^3A \rightarrow ^3E$ transition. The excited orbital doublet state produces the characteristic zero-phonon line at 637nm (1.945 eV) with a radiative decay time of 13ns [1.23]. The center also produces a paramagnetic resonance signal, which are the properties confirming the C_{3v} symmetry.

The $[(N-V)^0]$ center has nominal C_{3v} symmetry and zero-phonon E-A optical transition at 575nm (2.158 eV). The remarkable point of the 575nm center is the absorption that is to be very weak to detect, especially in the case of highly nitrogen contained type-Ib diamond. Its lifetime is 6ns at room temperature [1.24].

It has been reported that several other color centers emitting at the wavelength of 768, 746, 749, 764, 756, and 772nm was ascribed to defects containing Ni, Si and Cr atoms [1.25-1.29]. These centers were found in diamond nanocrystals grown by CVD method or were made in bulk diamond by ion implantation of the corresponding species. Even the atomic structure of these centers has not been established yet. However, the 768nm center has been tentatively ascribed to a complex containing Ni and Si atoms: the 746, 749, 764, 756nm centers have been ascribed to Cr-related defects, while the 772nm center might be a defect incorporating Cr and Ni atoms. A great advantage of these centers is the short luminescence lifetime. For example, the

luminescence lifetime of the 749nm Cr-related center is about 1 ns, which makes it the most efficient single-photon emitter working in bulk diamond.

1-4 Application of diamond

The research efforts in diamond synthesis are rewarded by its unique properties, which are then useful for many applications. Diamond has various advantages for electronics in the semiconductor. Due to the band gap, it is inherently suitable to emit or detect UV light. The low electron affinity allows electron emission at low temperatures. Devices based on diamond work readily at harsh conditions, e.g. under radiation or chemical corrosion. UV-sensors[1.30], light emitting diodes[1.31], cold cathode,[1.32] metal-semiconductor FETs,[1.33] and electro-chemical electrodes[1.34] have all, meanwhile, been implemented using diamond.

1-4-1 Nanodiamond as bio-marks

Over the past few years, nanomaterials, a branch of nano-biotechnology with emphasis on the views of the biological, have attracted much attention [1.35]. The study of nanomaterials involves biological applications and fabrication of bio-functionalized devices. Quantum dots have specifically been applied in fluorescent probes in recent years, which were immediately turned into a brightness

owing to the quantum yield can be compared to fluorescent dyes and have less photobleaching [1.36]. They were widely employed for the vitro imaging of pre-labeled cells due to those advantages. The ability to image single-cell migration in real time is expected to be important to several research areas, such as embryogenesis, cancer metastasis, stem-cell therapeutics, and lymphocyte immunology. However, the bio-cytotoxicity of quantum dots was concerned on medical applications. The semiconductor quantum dots can be dissolved, in a process as known as photolysis, to release toxic ions into the culture medium. The quantum dots must be carefully examined before its bio-cytotoxicity can be approved for clinical use.

In comparison, nanodiamonds which consist of carbon atoms possess remarkable features of low bio-cytotoxicity [1.37, 1.38]. As a result, the nanodiamonds is a relative safe nanomaterials based on its non-bio-cytotoxicity and biocompatibility.

Nanodiamonds are promising nano-materials owing to good chemical stability, various nanosizes, biocompatibility, good surface modification and good optical property for bio-applications [1.39-1.42]. The surface of nanodiamonds can also be a unique platform for the conjugation of chemicals and biomolecules after functional modifications. The surface of nanodiamond can carry a variety of oxygen containing functional groups immediately after purification in strong oxidative acids or oxidation in air. The acid-treated oxidative nanodiamonds show high affinity for biomolecules.

Surface carboxylated group of nanodiamond are typical ligands used for covalent coupling of these biomolecules to nanodiamonds through amide linkage.

The Raman[1.15] and photoluminescence[1.19-1.12] properties of nanodiamonds have been intensively studied. Some intrinsic Raman signals can be used as detection markers or can be employed in biological objects. This diamond Raman peak is strong and isolated, so it can be used as an indicator for allocating nanodiamonds.

1-4-2 CVD diamond for bio-chip applications

CVD diamond can be mono- or polycrystalline. Whereas monocrystalline diamond requires a diamond substrate, polycrystalline diamond can be grown on different materials, such as silicon (Si) and quartz (SiO_2), and is dominated by columnar growth. For grain sizes below 500 nm, the CVD film is called nanocrystalline diamond (NCD); after a certain thickness, the grain size near the surface exceeds 500 nm and the film then becomes microcrystalline diamond ($\mu\text{-CD}$). In addition, a slightly different material is ultra-nanocrystalline diamond (UNCD) which the grain size and roughness are not dependent on the film thickness, because these films do not show columnar growth. For optimization of detection techniques and sensitivities, for realization of highly integrated sensor arrays and for bio-interfaces, materials like Si, SiO_2 , gold, glassy carbon, SnO_2 , and ZnO_2 , do not possess desired chemical stability.

CVD diamond is an outstanding material for bioelectronics with good electronic and chemical properties [1.43, 1.44]. Additionally, ultra-hard diamond (50–150 GPa) is promising with respect to mechanical stability of nanostructure.

1-4-3 Diamond for Single-photon source

The development of reliable devices for the generation of single photons is crucial for many applications such as, for example, quantum cryptography[1.45], optical quantum computation[1.46] as well as experiments on the foundations of quantum optics [1.47, 1.48]. Single-photon emission was first observed from single atoms and ions in traps and from molecules. More recently, semiconductor quantum dots and photoactive point defects, such as nitrogen-vacancy (N-V) and silicon-vacancy (Si-V) in diamond have been used in SPE experiments [1.49, 1.50]. Among the array of luminescent nanomaterials, color centers in diamond seem to be the most-promising single-photon source for quantum-physics applications, such as optics, information processing and cryptography. This is due to the remarkable photoemission properties of the defects, such as their extraordinary stability at room temperature and their high quantum efficiency (typically >0.1), which are combined with the unique chemical and mechanical properties of the diamond material itself. Moreover, the association of a spin structure in the ground level resulted in a long coherence time at room temperature with spin-dependent optical transitions allows it to be developed for

quantum-state preparation by optical pumping and single-spin quantum state readout [1.51].

1-5 Research motivation and object

Nanodiamond carry the following features, such as, good photostability, easy surface-modification, and low cytotoxicity to be considered as a good nanomaterial for bio-applications. In this thesis work, we have developed a new technique which is a combination of SAM and E-beam lithography to pattern nanodiamond on silicon base substrate. As a result of the good bio-molecules absorptivity of nanodiamond, the nanodiamond arrays can easily be bio-functionalized. The technique which we demonstrated here is suitable for applications of bio-sensing chips and single bio-molecule patterning and detection. In what follows, we will expect to develop it to be as bio-chip based on bio-functionalized nanodiamond arrays.

The optical property of nanomaterials plays an important role for bio-applications, such as bio-labeling or optical sensing. The surface plasma resonance effect from the metallic nanoparticles greatly enhances the optical property. The ability to increase the fluorescence emission can greatly improve the effectiveness of fluorescence-based applications, such as single molecular detection and sensing in biology. The surface plasma resonance which is between gold nanoparticles and nanodiamonds can be

applied as template for bio-sensing chips. This optical enhancement can be used as optical sensing bio-sensors.

1-6 Reference

- [1.1] P. G. Read, *Gemmology*. Butterworth-Heinemann., 49,
- [1.2] L. H. Wei, P. K. Kuo, and R. L. Thomas, "Thermal Conductivity of Isotopically Modified Single Crystal Diamond," *Phys. rev. lett.*, vol. 70, 3764, (1993)
- [1.3] A.T. Collins, "The Optical and Electronic Properties of Semiconducting Diamond," *Philos. T. R. Soc. A*, vol. 342, 233, (1993)
- [1.4] H. T. Hall, "Ultra-high pressure apparatus," *Rev. Sci. Instr.*, vol. 31, 125, (1960)
- [1.5] F. P. Bundy, H. T. Hall, H. M. Strong and R. H. Wentorf, "Man-made diamonds," *Nature*, vol. 176, 51, (1955)
- [1.6] H. P. Bovenkerk, F. P. Bundy, H. T. Hall, H. M. Strong and R. H. Wentorf, "Preparation of diamond," *Nature*, vol. 184, 1094, (1959)
- [1.7] R. M. Hazen, "The diamond makers," Cambridge University Press, *GE diamond*, 100, (1999)
- [1.8] S. Matsumoto, Y. Sato, M. Tsutsumi, and N. Setaka, "Growth of diamond particles from methane-hydrogen gas," *J. Mater. Sci.*, vol. 17, 3106, (1982)
- [1.9] M. Kamo, Y. Sato, S. Matsumoto, and N. Setaka, "Diamond synthesis from gas

phase in microwave plasma," J. Cryst. Growth., vol. 62, 642, (1983)

[1.10] P. Decarli, and J. Jamieson, "Formation of Diamond by Explosive Shock," Science, vol. 133, 1821, (1961)

[1.11] E. M. Galimov et al, "Experimental Corroboration of the Synthesis of Diamond in the Cavitation Process," Doklady Physics, vol. 49, 150, (2004)

[1.12] A. Zaitsev, "Vibronic spectra of impurity-related optical centers in diamond," Phys. Rev. B, vol. 61, 12909, (2000)

[1.13] K. Iakoubovskii, Optical Study of Defects in Diamond. PhD thesis, Catholic University of Leuven, Belgium, (2000)

[1.14] T. Evans and Z. Qi, "The kinetics of the aggregation of nitrogen atoms in diamond," Proc. R. Soc. A, vol. 381, 159, (1982)

[1.15] J. Wagner, C. Wild, and P. Koidl, "Resonance effects in raman scattering from polycrystalline diamond films," Appl. Phys. Lett., vol. 59, 779, (1991)

[1.16] P.H. Chung, E. Perevedentseva, C.-L. Cheng a, "The particle size-dependent photoluminescence of nanodiamonds," Sur. Sci., vol. 601, 3866, (2007)

[1.17] J. Wrachtrup and F. Jelezko, "Processing quantum information in diamond," J. Phys.: Condens. Matter, vol. 18, S807, (2006)

[1.18] G. Davies, "Properties and Growth of Diamond," INSPEC, The Institution of Electrical Engineers, London, EMIs Data Review Series, (1994)

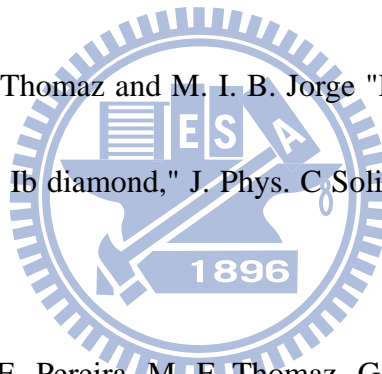
[1.19] G. Davies and M. F. Hamer, "Optical Studies of the 1.945 eV Vibronic Band in Diamond," Proc. R. Soc. Lon. Ser.-A, vol. 348, 285, (1976)

[1.20] G. Davies, S. C. Lawson, A. T. Collins, A. Mainwood, and S. J. Sharp, "Vacancy-related centers in diamond," Phys. Rev. B, vol. 46, 13157, (1992)

[1.21] Y. Mita, "Change of absorption spectra in type-Ib diamond with heavy neutron irradiation," Phys. Rev. B, vol. 53, 11360, (1996)

[1.22] G. Davies, "Charge states of the vacancy in diamond," Nature, vol. 269, 498, (1997).

[1.23] A. T. Collins, M. F. Thomaz and M. I. B. Jorge "Luminescence decay time of the 1.945 eV centre in type Ib diamond," J. Phys. C Solid State Phys., vol. 16, 2177, (1983)



[1.24] M. I. B. Jorge, M. E. Pereira, M. F. Thomaz, G. Davies, and A. T. Collins, "Decay times of luminescence from brown diamonds," Port. Phys., vol. 14, 195, (1983)

[1.25] I. Aharonvich, C. Zhou, A. Stacey, F. Treussart, J. F. Roch, and S. Praver, "Formation of color centers in nanodiamonds by plasma assisted diffusion of impurities from the growth substrate," Appl. Phys. Lett., vol. 93, 243112, (2009)

[1.26] I. Aharonvich, C. Zhou, A. Stacey, J. Orwa, S. Castelletto, D. Simpson, A. D. Greentree, F. Treussart, J. F. Roch, and S. Praver, "Enhanced single-photon emission

in the near infrared from a diamond color center," Phys. Rev. B, vol. 79, 235316, (2009)

[1.27] D. Steinmetz, E. Neu, J. Meijer, W. Borse, and C. Becher "Single photon emitters based on Ni/Si related defects in single crystalline diamond," arXiv:1007.0202

[1.28] I. Aharonovich, S. Castelletto, B. C. Johnson, J. C. McCallum, D. A. Simoson, A. D. Greentree and S. Praver. "Chromium single-photon emitters in diamond fabricated by ion implantation," Phys. Rev. B, vol. 81, 121201, (2010)

[1.29] P. Siyushev et al "Low-temperature optical characterization of a near-infrared single-photon emitter in nanodiamonds," New J. Phys., vol. 11, 113029, (2009)

[1.30] K. Hayashi, Y. Yokota, T. Tachibana, K. Kobashi, J. Achard, A. Gicquel, C. Olivero, M. Castex, and A. Treshchalov, "Temporal response of UV sensors made of highly oriented diamond films by 193 and 313 nm laser pulses," Diamond Relat. Mater., vol. 10, 1794, (1991)

[1.31] S. Koizumi, K. Watanabe, M. Hasegawa, and H. Kanda, "Ultraviolet emission from a diamond pn junction," Science, vol. 292, 1899, (2001)

[1.32] K. Okano, S. Koizumi, S. R. P. Silva, and G. A. J. Amaratunga, "Lowthreshold cold cathodes made of nitrogen-doped chemical-vapor deposited diamond," Nature, vol. 381, 140, (1996)

- [1.33] H. Umezawa, K. Tsugawa, S. Yamanaka, D. Takeuchi, H. Okushi, and H. Kawarada, "High-performance diamond metal-semiconductor field effect transistor with 1 μm gate length," *Jpn. J. Appl. Phys.*, vol. 38, 1222, (1999)
- [1.34] T. N. Rao and A. Fujishima, "Recent advances in electrochemistry of diamond," *Diamond Relat. Mater.*, vol. 9, 384, (2000)
- [1.35] C. M. Niemeyer, "Nanoparticles, Proteins, and Nucleic Acids: Biotechnology Meets Materials Science," *Angew. Chem., Int. Ed.*, vol. 40, 4128, (2001)
- [1.36] X. Michalet, F. F. Pinaud, L. A. Bentolila, M. Tsay, S. Doose, J. J. Li, G. Sundaresan, A. M. Wu, S. S. Gambhir, S. Weiss, "Quantum Dots for Live Cells and in vivo Imaging, Diagnostics and Beyond," *Science*, vol. 307, 538, (2005)
- [1.37] A. M. Schrand, H. Huang, C. Carlson, J. J. Schlager, E. Osawa, S. M. Hussain, and L. Dai, "Are Diamond Nanoparticles Cytotoxic?," *J. Phys. Chem. B*, vol. 111, 1, (2007)
- [1.38] S. J. Yu, M. W. Kang, H. C. Chang, K. M. Chen, and Y. C. Yu "Bright Fluorescent Nanodiamonds: No Photobleaching and Low Cytotoxicity" *J. Am. Chem. Soc.*, vol. 127, 17604, (2005)
- [1.39] H. Tamura, H. Zhou, K. Sugisako, Y. Yokoi, S. Takami, M. Kubo, K. Teraishi, A. Miyamoto, "Periodic density-functional study on oxidation of diamond (100) surfaces," *Phys. Rev. B*, vol. 61, 11025, (2000)

[1.40] E. Mironov, A. Koretz, E. Petrov, "Detonation synthesis ultradispersed diamond structural properties investigation by infrared absorption," *Diamond Relat. Mater.*, vol. 11, 872, (2002)

[1.41] Wenmackers, S.D. Pop, K. Roodenko, V. Vermeeren, O.A. Williams, M. Daenen, O. Douheret, J. D'Haen, A. Hardy, M.K. Van Bael, K. Hinrichs, C. Cobet, M. vande Ven, M. Ameloot, K. Haenen, L. Michiels, N. Esser, P. Wanger, "Structural and optical properties of DNA layers covalently attached to diamond surfaces," *Langmuir*, vol. 24, 7269, (2008)

[1.42] P. Christiaens, V. Vermeeren, S. Wenmackers, M. Daenen, K. Haenen, M. Nesladek, M. vande Ven, M. Ameloot, L. Michiels, P. Wanger, "EDC-mediated DNA attachment to nanocrystalline CVD diamond films," *Biosens. Bioelectron.*, vol. 22, 170, (2006)

[1.43] C.E. Nebel, J. Rinstein (eds) "Thin-Film Diamond I," *Semiconductors and Semimetals*, 76, Elsevier Academic Press.

[1.44] C.E. Nebel, J. Rinstein (eds) "Thin-Film Diamond II," *Semiconductors and Semimetals*, 76, Elsevier Academic Press.

[1.45] N. Gisin, G. Ribordy, W. Tittel, and H. Zbinden, "Quantum cryptography," *Rev. Mod. Phys.*, vol. 74, 145, (2002)

[1.46] E. Knill, R. Laflamme and G. J. Milburn, "A scheme for efficient quantum

computation with linear optics" Nature, vol. 409, 46, (2001)

[1.47] C. Braig, P. Zarda, C. Kurtsiefer, and H. Weinfurter, "Experimental demonstration of complementarity with single photons," Appl. Phys. B, vol. 76, 113, (2003)

[1.48] T. Aichele, U. Herzog, M. Scholz and O. Benson, "Single-photon generation and simultaneous observation of wave and particle properties," AIP Proc., vol. 750, 35, (2005)

[1.49] C. Kurtsiefer, S. Mayer, P. Zarda, and H. Weinfurter, "Stable solidstate source of single photons," Phys. Rev. Lett., vol. 85, 290, (2000)

[1.50] R. Brouri, A. Beveratos, J. P. Poizat, and P. Grangier, "Photon antibunching in the fluorescence of individual color centers in diamond," Opt. Lett., vol. 25, 1294, (2000)

[1.51] P. Neumann, R. Kolesov, B. Naydenov, J. Beck1, F. Rempp, M. Steiner, V. Jacques, G. Balasubramanian, M. L. Markham, D. J. Twitchen, S. Pezzagna, J. Meijer, J. Twamley, F. Jelezko and J. Wrachtrup "Quantum register based on coupled electron spins in a room-temperature solid," Nat. Phys., vol. 6, 249, (2010)

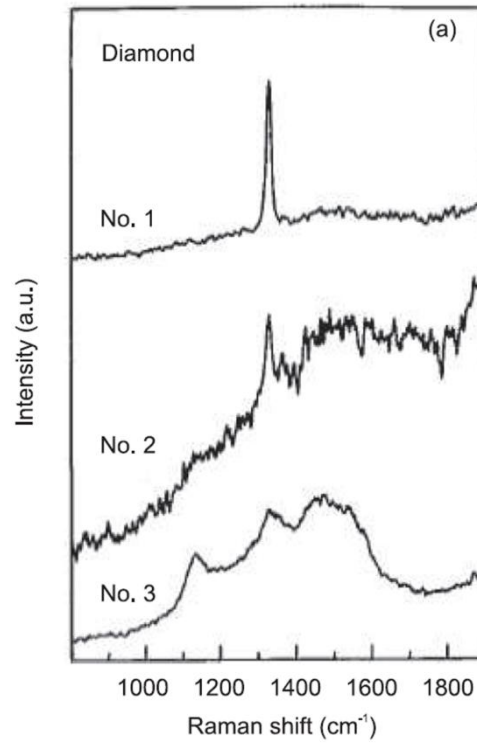


Figure 1-1(a): Raman spectra of three different CVD diamond films [1.15]

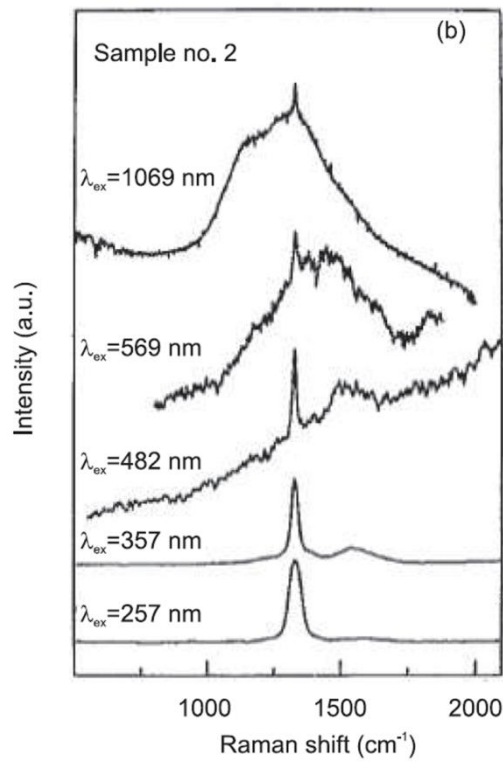


Figure 1-1(b): The different spectra of various wavelength of laser excitation of diamond [1.15]

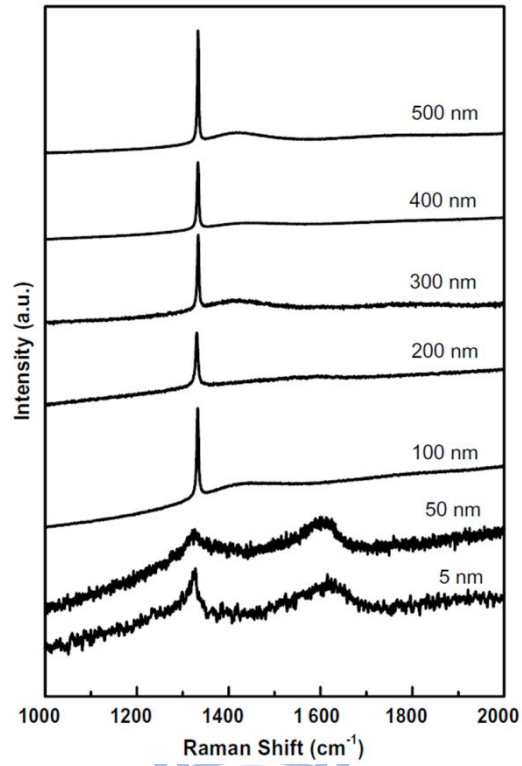


Figure 1-2: Raman spectra of nanodiamonds of different size [1.16]

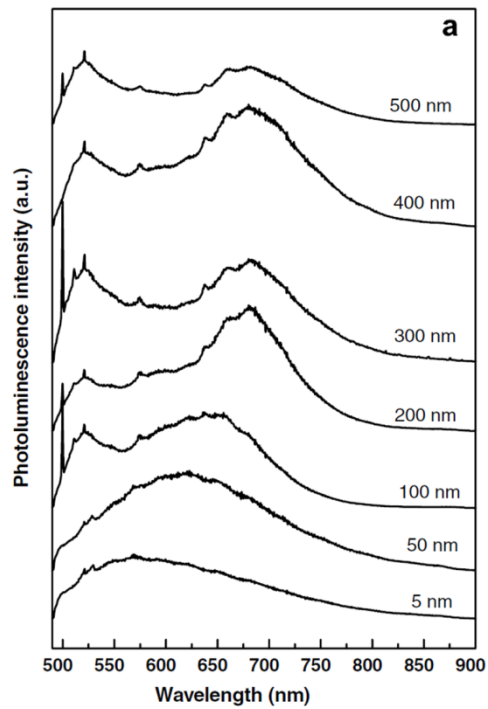


Figure 1-3: (a) Photoluminescence spectra of different sizes nanodiamonds obtained

by using 488nm laser excitation [1.16]

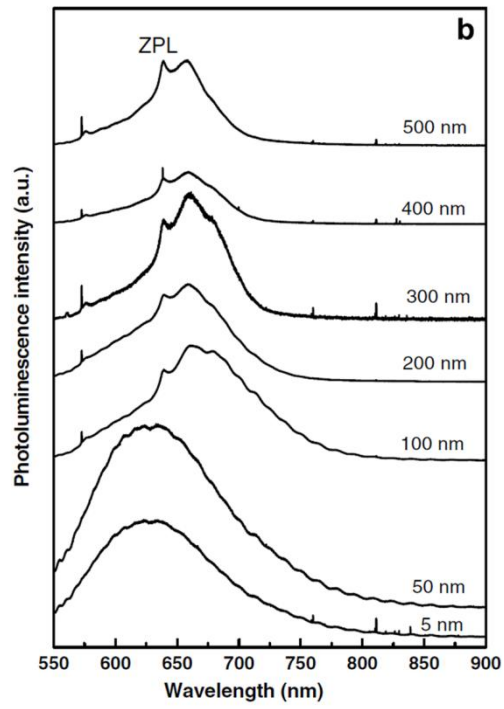
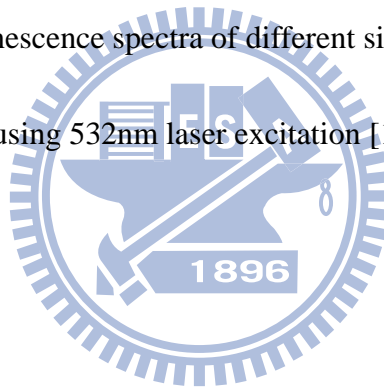


Figure 1-3: (b) Photoluminescence spectra of different sizes nanodiamonds obtained by using 532nm laser excitation [1.16]



Chapter 2 Skeleton of this thesis and instrumentation

2-1 Description of the remaining chapters

This thesis is composed of two separated but closed related research works on nanodiamonds. A short abstract of each experimental work and instrumentation sections are given below. More details and discussion are presented in chapter 3 and 4. Studies related to the nitrogen-doped ultrananocrystalline diamond films generated by microwave plasma are put in the appendix attached to this thesis.

2-1-1 Protein Functionalized Nanodiamond Arrays

Nanodiamonds possess remarkable features such as low bio-cytotoxicity, good optical property in fluorescent and Raman spectra, and good photostability for bio-applications. In chapter 3, we devise techniques to position functionalized nanodiamonds on self-assembled monolayer (SAMs) arrays adsorbed on silicon and ITO substrates surface using electron beam lithography techniques. The nanodiamond arrays were functionalized with lysozyme to target a certain bio-molecule or protein specifically. The optical properties of the nanodiamond-protein complex arrays were characterized by a high throughput confocal microscope. The synthesized nanodiamond-lysozyme complex arrays were found to still retain their functionality in

interacting with E. coli. This work is elaborated in chapter 3.

2-1-2 Plasmon-enhanced photoluminescence from bioconjugated gold

nanoparticle and nanodiamond assembly

In this part of the work, we coupled NDs with gold nanoparticles of different sizes using two complementary DNA sequences. After hybridizing the gold nanoparticles on the NDs, we observed the enhancement of the photoluminescence (PL) signals originating from the nitrogen-vacancy (N-V) center of the ND. The enhancement was attributed to the plasmon field created by the gold nanoparticles. The lineshape of the enhanced PL spectra was also affected by the sizes of the attached nanoparticles due to their different resonant plasma frequencies. The signal enhancement can be used as an indexing tool for bio-sensing applications. This work is elaborated in chapter 4.

2-2 Instrumentation

2-2-1 E-beam lithography

Generally speaking , electron beam lithograph system is constructed from four main parts ; including electron optical column · chamber · handling system · and control unit. The major part is electron optical column, which determines the shape of

electron. It controls the image resolution and exposing quality. Electron optical column is generally composed of electron gun、blanking、condense lens、stigmator、objective lens、deflector、and electron detector (figure 2-1). These accessories enable the electron beam ejecting from electron gun to be well-controlled and expose to the right place.

There are three common phenomena occur during the exposure of electron beam system ; including forward scattering、back scattering、and charging effect. Each of them can influence the quality of the e-beam exposed patterns, especially when the pattern size is down to sub-50nm. The effect of forward and back scattering will broaden the pitch size and produce some proximity effect. The charging effect is the results of the electron accumulation phenomenon. These effects will blur the exposed image and produce a poor exposure quality (figure 2-2).

2-2-2 Confocal microscopes

The principle of confocal imaging was patented in 1957 by Marvin Minsky and aims to overcome the limitation of traditional wide field fluorescence microscopes [2.1]. In wide field fluorescence microscope, the entire specimen is flooded in light from a light source. The whole specimen in the optical path was totally excited at the same time and the fluorescence of the specimen was detected by the microscope's detector including the unfocused background parts. The principle of cofocal

microscopes is to use both point-wise illumination and detection. As shown in figure 2-3, the point illumination and a pinhole were in an optically conjugate plane in front of the detector in order to eliminate out-of-focus signals. The name confocal stems from this configuration. As the only signals very close to the focal plane can be detected, the image, the image's optical resolution, particularly in the sample depth direction, is much better than that of wide-field microscopes. However, as much of the light from sample fluorescence is blocked at the pinhole, this increased resolution is at the cost of decreased signal intensity – so long exposures are often required.

As only one point in the sample is illuminated at a time, 2D or 3D imaging requires scanning over a regular raster (i.e. a rectangular pattern of parallel scanning lines) in the specimen. The achievable thickness of the focal plane is defined mostly by the wavelength of the used light divided by the numerical aperture of the objective lens, but also by the optical properties of the specimen. The thin optical sectioning possible makes these types of microscopes particularly good at 3D imaging and surface profiling of samples.

2-2-3 Raman spectrum

Although the inelastic scattering of light was predicted by Adolf Smekal in 1923, it is not until 1928 that it was observed in practice. The Raman effect was named after one of its discoverers, the Indian scientist Sir C. V. Raman who observed the effect by

means of sunlight (1928, together with K. S. Krishnan and independently by Grigory Landsberg and Leonid Mandelstam). Raman won the Nobel Prize in Physics in 1930 for this discovery accomplished using sunlight, a narrow band photographic filter to create monochromatic light and a "crossed" filter to block this monochromatic light. He found that light of changed frequency passed through the "crossed" filter. Systematic pioneering theory of the Raman effect was developed by Czechoslovak physicist George Placzek between 1930 and 1934. The mercury arc became the principal light source, first with photographic detection and then with spectrophotometric detection. At the present time, lasers are used as light sources.

The Raman effect is a light scattering phenomenon. While light of frequency V_0 (usually from a laser) irradiates a sample, it can be scattered. The frequency of the scattered light can either be at the original frequency which referred to as Rayleigh scattering or at some shifted frequency $V_S = V_0 \pm V_{\text{internal}}$ (referred at as Raman scattering). The frequency V_{internal} is an internal frequency corresponding to rotational, vibrational, or electronic transitions. In discussing the Raman effect, some commonly used terms need to be defined. As shown in figure 2-4, radiation scattering to the lower frequency side (to the red) of the exciting line is call Stockes scattering. The scattering radiation at the same frequency as the incident radiation is called Rayleigh scattering. While the light scattered at higher frequency than exciting line (to the blue)

is referred to as the anti-Stokes scattering. Finally, the magnitude of this shift between the Stokes or the anti-Stokes line and the exciting line is called the Raman shift,

$\Delta V = |V_0 - V_{\text{internal}}|$. The energy diagram for Stokes and anti-Stokes scattering was shown in figure 2-4.

2-2-4 Luminescence

Luminescence is the emission of light from any substance and occurs from electronically excited states. Luminescence can be of two types: fluorescence and phosphorescence. Phosphorescence is emission of light from triplet-excited states, in which the electron in the excited orbital has the same spin orientation as the ground-state electron. Transitions to the ground state are forbidden and the emission rates are slow (10^3 - 100 s^{-1}), so phosphorescence lifetimes are typically milliseconds to seconds. Phosphorescence is usually not seen in fluid solutions at room temperature, but there are many deactivation processes that compete with emission, such as nonradiative decay and quenching processes. Fluorescence is emission light from singlet-excited states, in which the electron in the excited orbital is paired (of opposite sign) to the second electron in the ground-state orbital. Return to the ground state is spin-allowed and occurs rapidly by emission of a photon. Those emission rates of fluorescence typically are 10^8 s^{-1} , so that a typical fluorescence lifetime is near 10 ns. Fluorescence spectral data are generally presented as emission spectra. Emission

spectra vary widely and are dependent upon the chemical structure of the fluorophore and the solvent in which it is dissolved.

A fluorophore is usually excited to some higher vibrational level of either S_1 or S_2 . With a few rare exceptions, molecules in condensed phases rapidly relax to the lowest vibrational level of S_1 . This process, called internal conversion, is nonradiative and takes place in 10^{-12} seconds or less. Return to the ground state occurs to a higher excited vibrational ground-state level, which then quickly reaches thermal equilibrium.

An interesting consequence of emission to a higher vibrational ground state is that the emission spectrum is typically a mirror image of the absorption spectrum of the $S_0 \rightarrow S_1$ transition.

Molecules in the S_1 state can also undergo a spin conversion to the first triplet state, T_1 . Emission from T_1 is termed phosphorescence and is generally shifted to longer wavelengths (lower energy) relative to fluorescence. Transition from the T_1 to the singlet ground state is forbidden, and as a result, the rate constants for triplet emission are several orders of magnitude smaller than those for fluorescence. As shown in figure 2-5, processes which occur between the absorption and emission of light are usually illustrated by a Jablonski diagram.

2-3 Reference

[2.1] Paul Daviddovits and M. David Egger, "Scanning Laser Microscope," nature, vol. 223, 831 (1969)

[2.2] ELS-7500EX Electron Beam Lithography System Instrument Manual, ELIONIX Inc.



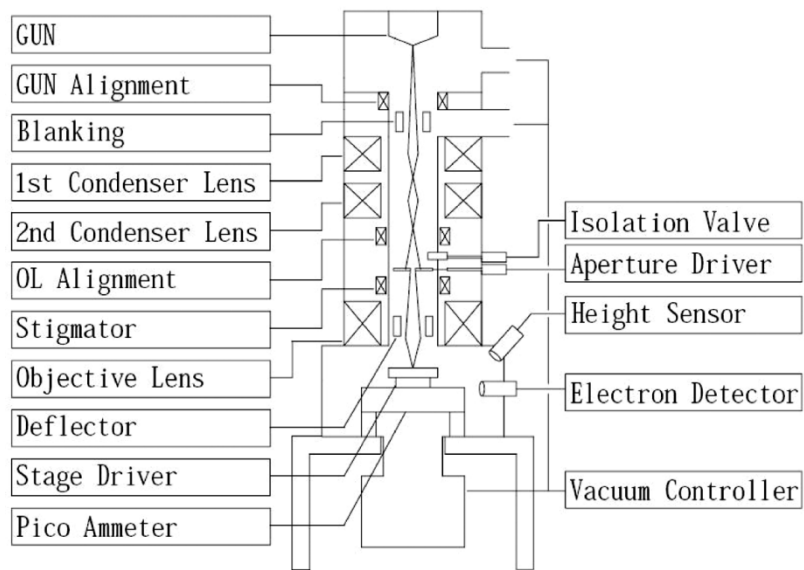
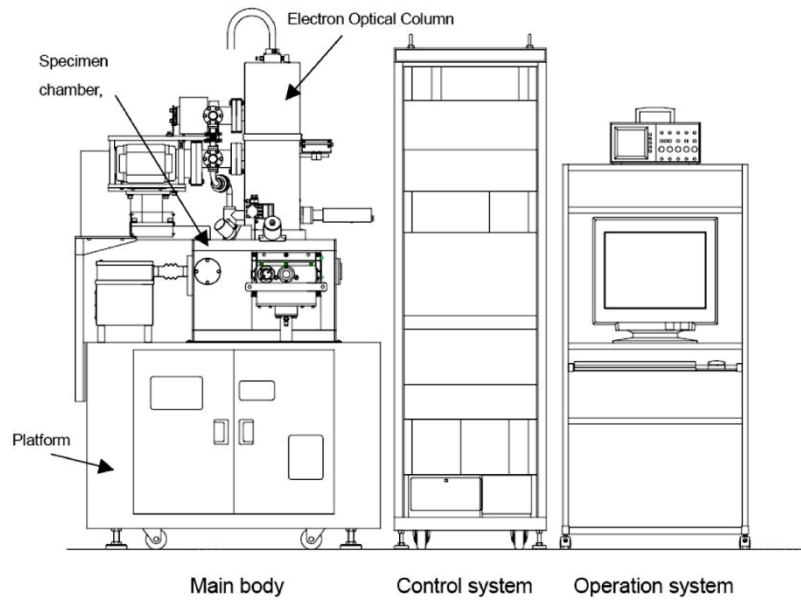


Figure 2-1: Overlay of electron beam system and the electron optical column of electron beam system [2.2]

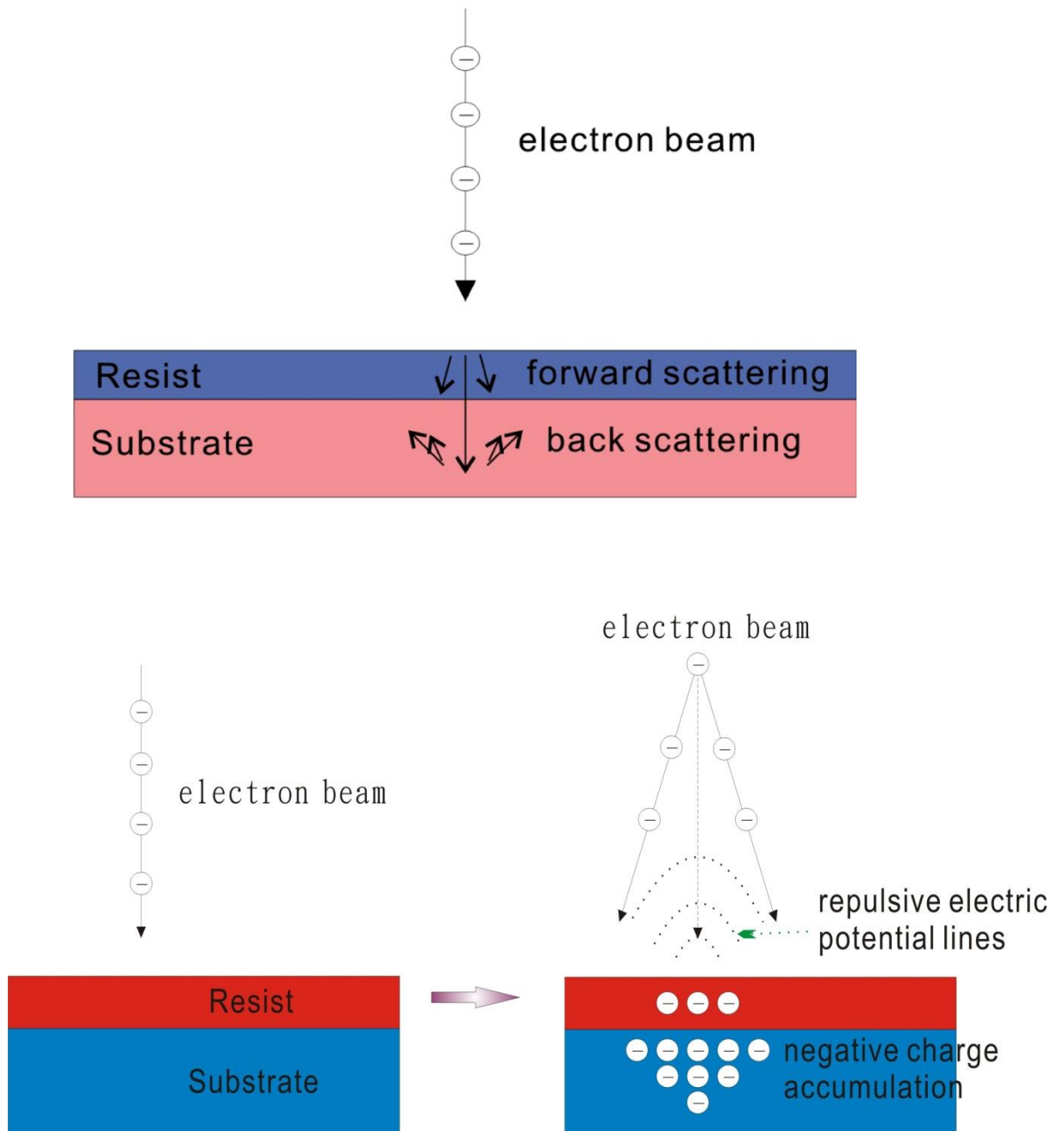


Figure 2-2: Illustration and simulation result of forward and back scattering effect

and the charge effect during the electron beam process

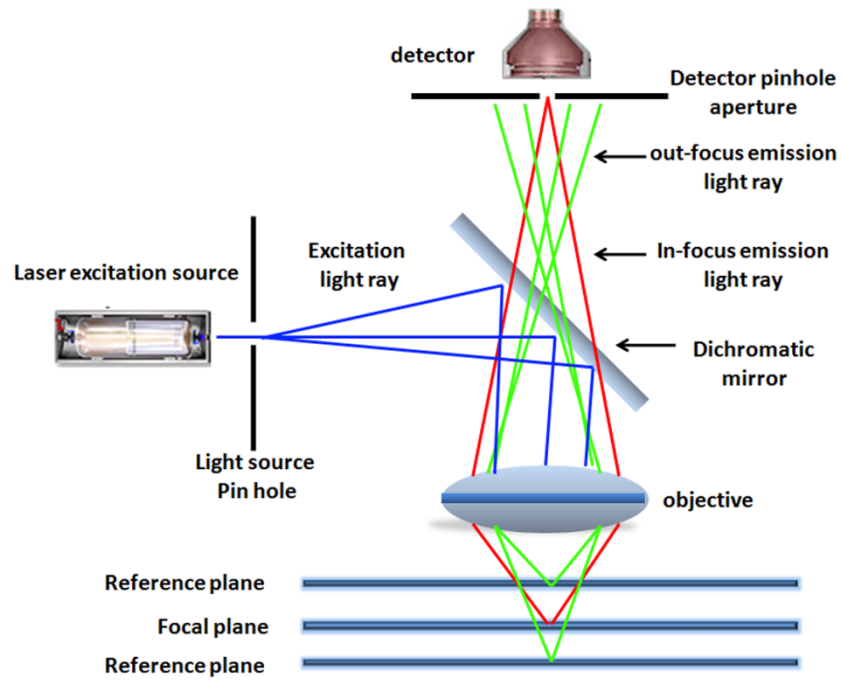


Figure 2-3: Illumination of confocal microscope



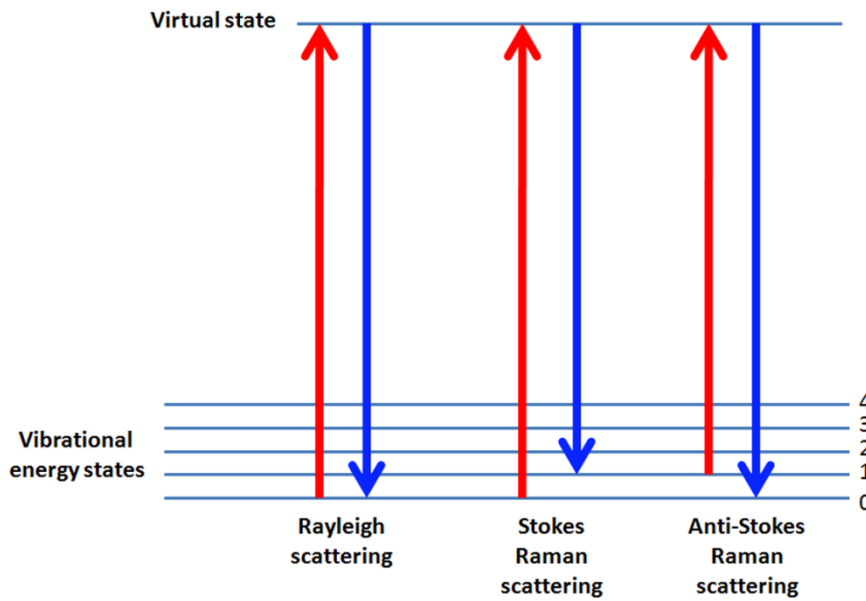
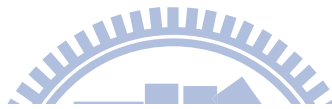
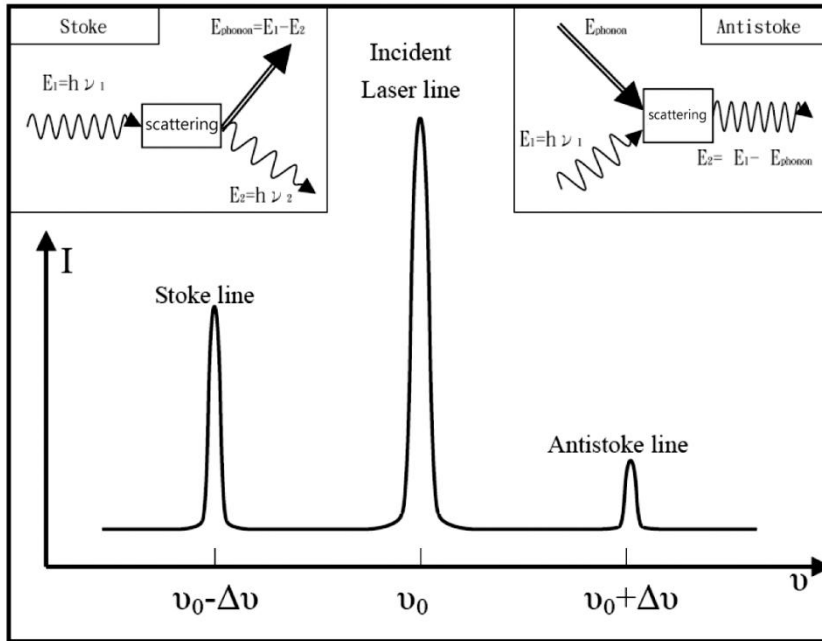


Figure 2-4: Energy diagram for Rayleigh, Stokes, and anti-Stokes scattering

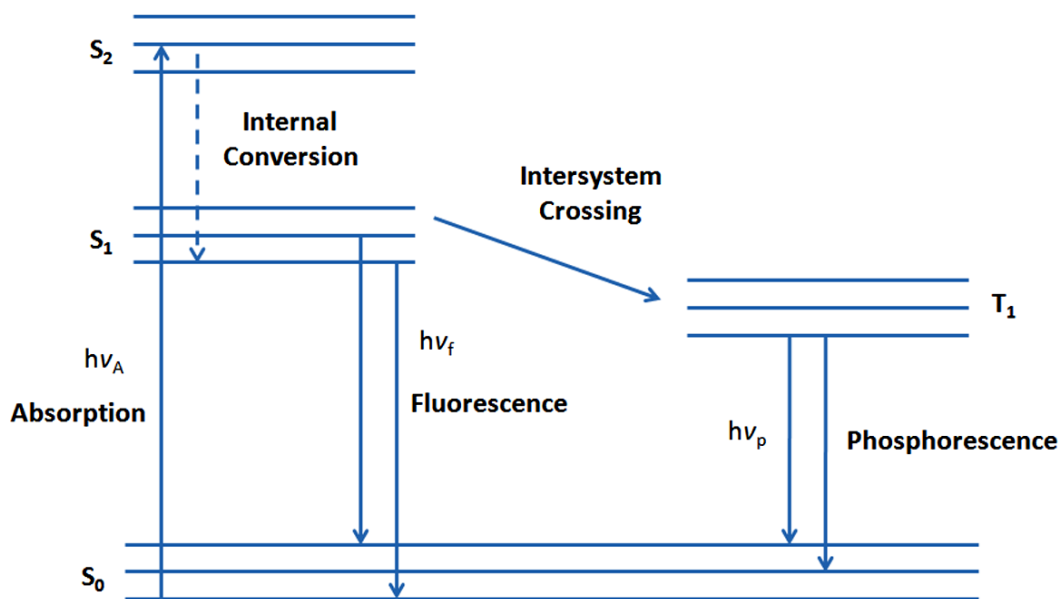
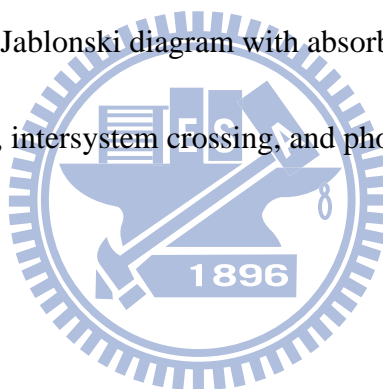


Figure 2-5: Simplified Jablonski diagram with absorbance, internal conversion, fluorescence, intersystem crossing, and phosphorescence



Chapter 3 Application of bio-functionalized nanodiamond arrays

3-1 Literature review

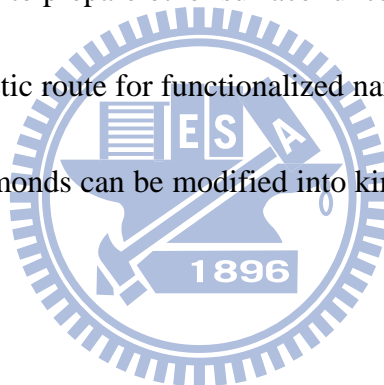
3-1-1 Nanodiamond

The cytotoxicity of nano-materials has been mostly concerned while the development of biomedical applications. Among of numerous nano-materials, nanodiamonds possess remarkable features of low-cytotoxicity. In the previous reports [3.1], it has been shown that nanodiamonds induce no significant cytotoxicity in variety of cell types. Jui-I. Chao, Chia-Liang Cheng, and their coworkers has shown that nanodiamonds are no or very low cytotoxicity for lung cells. The cytotoxicity test of nanodiamonds in human lung cells was demonstrated (figure 3-1). It indicates that nanodiamonds did not significantly induce the cell death. The nanodiamonds examined in many other cells including neuronal, renal, and cervical cells also show no cytotoxicity in those cells. As a result, nanodiamonds are relatively safe nano-materials for further evaluation of clinical applications.

Other the low cytotoxicity, the detectable fluorescence of nanodiamonds with no photobleaching was demonstrated in previous researches [3.2]. The figure 3-2 shows photostability tests of nanodiamond (red) and fluorescent polystyrene nanospheres

(blue) excited under the same conditions. Accord to the results of photostability test, no sign of photobleaching was found for nanodiamond even 8 hours of continuous excitation. By contrast, the fluorescence of polystyrene nanospheres was photobleached within 0.5 hour under the same condition.

The nanodiamonds are chemically inert, but can be surface-functionalized easily. For the oxidative acid-treated, nanodiamonds can carry a variety of oxygen-containing such as carboxylated group. Carboxylated nanodiamond can be used to as a starting material to prepare other surface functionalized nanodiamond. The figure 3-3 shows the synthetic route for functionalized nanodiamonds. It demonstrates that the surface of nanodiamonds can be modified into kinds of functional groups [3.3, 3.4].



3-1-2 Bio-chip

The development of biochip is a major thrust of biotechnology, which encompasses a very diverse range of research. At the same time, the semiconductor fabrication technology has been steadily perfecting the science of micro and nano- miniaturization. In recently, the combination of those two technologies has enabled biotechnology to begin packing traditionally bulky sensing tools into smaller and smaller area named as bio-chip. Thousands of biochemical reactions were performed at those miniaturized chips. The biochip can be able to large numbers of biological analytes quickly for

various purposes such as disease diagnosis or detection of bio- agents.

The biochip can be typically classified into two types. One is the processing chip and the other one is microarray chip. The processing chip, also named as Lab-on-chip (LOC), is a device which integrates several laboratory functions on a single chip by combination of micro-fluidics and Microelectromechanical systems (MEMs) [3.5]. For the microarray chip, the bio-molecules such as DNA, protein, or cells were deposited on the flat substrates like glasses, silicon wafer, or polymers with the high density and small areas. Surface chemistry is used to covalently bind the sensor molecules to the substrate medium.

The development of biochip is multi division of research systems including bio-molecules, chip surface modification, and signal detection. The bio-molecules modification on surface is very important for bio-chip researches. Physical adsorption and chemical adsorption are widely used in bio-chip. In the physical adsorption, bio-molecules attach to substrate via Van der waals force such as hydrophobic interaction and electrostatic attraction force. In the chemical adsorption, bio-molecules form the covalent linking with substrate. For example, amino group of horseradish peroxidase (HRP) reacts with carboxylated group of 16-mercaptohexadecanoic (16-MHA) forming amide bonding.

The signals such as variations of electric or optical properties were used to take as

reference for detecting reaction of biomolecules. In the previous report, Yi Cui and his coworkers demonstrated that the electric property of silicon nanowire was altered by charge change of surface modified molecules. The figure 3-4 shows electric properties of surface modified nanowire were affected by the variation of pH value [3.6].

3-2 Fabrication of bio-functionalized nanodiamond arrays by self assemble monolayer

3-2-1 Preparation of carboxylated nanodiamond solution

The average diameter of the nanodiamond (ND) powder used in our experiments is about 100nm (General Electric company, USA). The particle size is confirmed by SEM.

The 0.15g nanodiamond powder was treated with the 160ml 5:1 mixture of concentrated H_2SO_4 and HNO_3 solutions at 75 °C for 1 hour in ultrasonic bath for dispersion and stir for 11 hours for carboxylated reaction, and extensively rinsed several times with DI water and dry [3.7]. The sediment was then collected and dried.

The functional COOH group was formed on the ND surface followed by the standard chemical treatment mentioned above. The surface functional carboxylated group of nanodiamonds was checked by Fourier transform infrared and Raman spectroscopy.

The acoustic cavitation [3.8, 3.9] generated by ultrasonic bath heats up the water to

make the dissociation of water into H^+ and OH^- ions. While the OH^- ions adsorb on the surface of nanodiamonds, the increasing of electric charges on nanodiamond surface induce a coulomb repulsion force between nanoparticles. Therefore, the clustering of nanodiamonds can be avoided. The NDs solution was prepared by adding 0.1 g of carboxylated functionalized NDs into 100 ml of deionized water followed by an ultrasonic bath for 60 min.

3-2-2 Fabrication of nanodiamond nanoarray by self assemble monolayer

A silicon wafer was first diced into 15 mm x 15 mm chips. A silicon oxide layer was grown on the silicon chips with a thickness of about 400 nm by using Plasma enhanced chemical vapor deposition (PECVD). The substrate was first cleaned with ultrasonic bath in acetone, isopropyl alcohol, and deionized water solution for 5 min. Then the ZEP520 photoresist was spin-coated on the silicon oxide substrates at a rate of 500 rpm for 10 sec and 5000 rpm for 50 sec, and baked at 180 °C for 2 min. The thickness of the photoresist on the silicon chip was about 300 nm.

Self-assembled monolayer (SAM) is an organized layer of amphiphilic molecules in which one end of the molecules, the head group shows a specific, reversible affinity for substrates. SAMs are created by the chemical sorption of hydrophilic head groups onto a substrate from the vapor or liquid phase followed by a slow two dimensional organization of hydrophobic tail groups. Initially, adsorbate molecules

form either a disordered mass of molecules or form a lying down phase, and over a period of minutes to hours, begin to form crystalline or semicrystalline structures on the substrate surface. The hydrophilic head groups assemble together on the substrate, while the hydrophobic tail groups assemble far from the substrate. Areas of close-packed molecules nucleate and grow until the surface of the substrate is covered in a single monolayer. To form an amino-terminated layer on the surface of substrate, the substrates were immersed in 5 vol% solution of 3-aminopropyl triethoxysilane (APTES) in 95% ethanol for 4 hours and later rinsed with ethanol and thermally treated at 120 °C for 60 min [3.10].

The patterned substrate was dipped into 3 ml of the NDs solution and 3 ml of 0.1 M MES buffer (2-(N-morpholino) ethane sulfonic acid). After which, 6 ml of 0.025 M EDC solution 1-ethyl-3-[3-(dimethylamino)propyl]carbodiimide hydrochloride, 0.025 M NHS solution (N-hydroxysuccinimide) (here after “EDC/NHS solution”) and 8 ml deionized water were added into the reaction and allowed to stabilize for 8 hours. After the reaction was completed, the substrate was washed with acetone. The entire template was then immersed into ZDMAC (dimethylacetamide) solution for 4 hours to remove the photoresist. The substrate was again washed with acetone and deionized water, then dried with N₂. The figure 3-5 (a) and (b) show how the carboxylated NDs were anchored on the patterned silicon templates and processes for

the preparation of the substrates.

3-2-3 Fabrication of PLL and FITC functionalized nanodiamond nanoarray

The PLL (poly-L-lysine hydrobromide) solution was prepared by dissolving 8ml PLL into 20ml borate buffer and the FITC (fluorescence isothiocyanate) solution was prepared by dissolving 10mg FITC into 3ml borate buffer. The nanodiamond array chip was dipped into the 3ml borate buffer and reacted with the added 1ml PLL solution for 60 minutes. After reaction, the nanodiamond array chip was washed by borate buffer and deionized water. The PLL functionalized nanodiamond arrays were demonstrated. The adsorption of PLL on the nanodiamond arrays was further verified using the FITC as a probe. Then, the chip was dipped into the mixture of 3ml borate buffer and 0.02ml FITC solution and reacted for 30 minutes in dark room. The superfluous FITC was washed by DMSO, borate buffer and deionized water. All of the processes were carried under 4 °C. The figure 3-6 shows the processes of the nanodiamond array chip which was functionalized by PLL and attached with FITC.

[3.11]

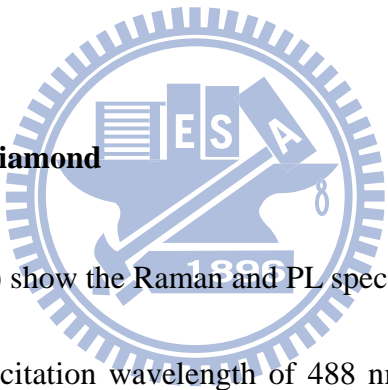
3-2-4 Fabrication of Lysozyme functionalized nanodiamond arrays

The lysozyme solution was prepared by dissolving 0.1g lysozyme into 20ml PBS (Phosphate-buffered saline) buffer. To ensure equilibration absorption, the

nanodiamond patterned chip was dipped into the lysozyme solution mentioned above and mixed together with stirring for 2hr before it was washed by PBS buffer and deionized water. After which, 10 μ l of E.coli suspension in 90 μ l PBS medium was mixed with the nanodiamonds chip in PBS buffer. The nanodiamond chip was washed with PBS buffer and deionized water. The lysozyme functionalized nanodiamond array was preserved under 4°C before examination.

3-3 Results and discussion

3-3-1 Carboxylated nanodiamond



The figure 3-7 (a) and (b) show the Raman and PL spectra of NDs with and without the acid treatment at an excitation wavelength of 488 nm. The treatment with acid particularly removed the carbon-like structure from the ND surface. In the Raman spectrum, the peaks at 1350 cm^{-1} and 1580 cm^{-1} (D-band and G-band signals caused by the carbon-like SP^2 structure from the ND surface) were clearly attenuated after the acid treatment [3.12]. The figure 3-7(b) shows that the narrower emission band was obtained because the acid treatment reduced the surface disorder and the number of surface defects [3.13]. The figure 3-8 shows the Fourier transform infrared (FTIR) spectroscopy of NDs before and after acid treatment. In the FTIR spectrum, the

surface carboxylated groups induce the peaks between 3100 and 3300 cm^{-1} broadening [3.7].

3-3-2 Nanodiamond nanoarray

Two kinds of patterns were designed to be placed on the Si templates. One is the crossmarks and the other one is nanohole arrays. The crossmarks have a length of 600 μm and a width of 20 μm . The nanohole arrays have an average diameter of 300 nm and a pitch size of 5 μm . The figure 3-9 (a) shows the scanning electron microscope (SEM) image of one of the corners inside the crossmark. The SEM image of 2 dimensional nano arrays with a diameter of 300 nm and the pitch of the array in 5 μm is shown in Figure 3-9(b). From the SEM images one can observe that the nanodiamonds bonded with the patterned SAM inside the nano holes. The inset in Figure 3-9(b) shows a single functionalized ND was isolated inside a nano hole. The SEM image proves that we were able to arrange NDs with various well-defined patterns on the silicon substrates.

The cross-section SEM image of the patterned single nanodiamond was shown in Figure 3-10(a). The images were taken by cutting a trench in front of a patterned single nanodiamond with a focused ion beam (FIB). The figure 3-10(b) shows the atomic force microscopy (AFM) image of the nanodiamond array. According the cross-section SEM image and the AFM image, the well patterned single nanodiamond

array can be proved.

The optical properties of the patterned nanodiamonds are demonstrated as follows. The micro-Raman spectra were also excited inside the reference crossmarks, nano holes, and outside the nano hole array with a laser beam of about 1 μm in diameter. The Raman signals, as shown in Figure 3-11(a), were only found inside the crossmarks and nano holes array where the NDs were anchored. However, with the laser beam placed outside the nano hole array (pattern-out area), no diamond-related signals were collected. This indicates that NDs were only allocated on the SAM inside the crossmarks and the nano hole arrays. The locations of the anchored NDs were further examined with the photoluminescence spectra excited at a wavelength of 532 nm. The PL spectra are shown in Figure 3-11(b). The PL spectrum of the ND clusters is also shown in Figure 3-11(b) for comparison. Again, no PL signals can be found outside the pattern area.

A one dimensional (1D) Raman intensity image mapping was carried out along a selected nano hole array, as shown in figure 3-12(a). The laser beam with a diameter of 1 μm was scanned along a distance of 20 μm with a 500 nm step. The intensity of the 1332 cm^{-1} Raman signal as a function of the scanning distance was plotted in figure 3-12(b). We also performed a two-dimensional (2D) Raman spectra mapping in a selected square area (the area is shown by the red square in figure 3-13(a). The 2D

image of integrated Raman intensity mapping of the 1332cm^{-1} Raman peak is shown in figure 3-13(b). Keep in mind that the nanodiamond arrays were designed with a pitch of $5\mu\text{m}$. When compared with the results from the 2D Raman intensity mapping, we found that the intensity distribution was perfectly correlated with the spatial distribution of the nano hole arrays. The results indicate that the NDs were only anchored inside the nano holes and were perfectly distributed on the template according to the pattern defined by the e-beam lithography technique.

3-3-3 PLL and FITC functionalized nanodiamond arrays.

In the figure 3-14(a) shows the optical microscope image of the PLL and FITC functionalize nanodiamond arrays. The FITC dye was excited by 488nm laser and emission at 518nm. The 1D PL mapping was demonstrated along the selected red line in the figure 3-12(a). The results of PL mapping shown in figure 3-14(b) indicates that the intensity distribution of FITC was perfectly correlated with the spatial distribution of the PLL and FITC functionalized nanodiamond arrays. It was proved by detecting the PL signals from FITC that the nanodiamond arrays can be successfully functionalized by PLL. It was proved that the nanodiamond arrays can be functionalized by bio-molecules under above examination.

3-3-4 Lysozyme functionalized nanodiamond arrays

The lysozyme solution was prepared by dissolving 0.1g lysozyme into 20ml PBS (Phosphate-buffered saline) buffer. To ensure equilibration absorption, the nanodiamond patterned chip was dipped into the lysozyme solution mentioned above and mixed together with stirring for 2hr before it was washed by PBS buffer and deionized water. After which, 10 μ l of E.coli suspension in 90 μ l PBS medium was mixed with the nanodiamonds chip in PBS buffer. The nanodiamond chip was washed with PBS buffer and deionized water. The lysozyme functionalized nanodiamond array was preserved under 4°C before examination.

In the figure 3-15, the FTIR (Fourier transform infrared) spectra were shown for three different samples of carboxylated nanodiamond, lysozyme protein, and lysozyme functionalized nanodiamond arrays [3.7]. The carboxylated nanodiamonds show the peaks of C=O group at 1750 cm^{-1} and of carboxylated group at 3000 cm^{-1} -3500 cm^{-1} . The ratio of carboxylated groups on nanodiamond surface is about 7% [3.14, 3.15]. It makes the weaker signal of the surface carboxylated groups but the carboxylated group of nanodiamonds surface can be confirmed in FTIR spectrum. The FTIR spectrum of lysozyme is shown in Figure 3-15(b). The appearance of amide peaks is at 1490 cm^{-1} - 1590 cm^{-1} (amide 1), 1600 cm^{-1} - 1700 cm^{-1} (amide 2), and 3100 cm^{-1} - 3300 cm^{-1} from the lysozyme [3.7]. The spectra of lysozyme

functionalized nanodiamond arrays are shown Figure 3-15(c). Due to the large background from the SiO₂ layer for the energy larger than 3000 cm⁻¹, detecting any peaks higher than 3000 cm⁻¹ is difficult. However, weak peaks of amide at 1490 cm⁻¹ - 1590 cm⁻¹ and 1600 cm⁻¹ - 1700 cm⁻¹ that from lysozyme can still be identified, as shown in Figure 3-15(c).

The investigation of Raman spectra for the three different samples of lysozyme, lysozyme functionalized nanodiamond solution, and lysozyme functionalized nanodiamond arrays are shown in Figure 3-16. The figure 3-16(a) shows the Raman spectrum of the protein lysozyme. In the region between 1400 cm⁻¹ and 1700 cm⁻¹, some weak peaks were found due to amide in protein, amino acid, CH, and CH₂ groups. Figures 3-16(b) and 3-16(c) show the Raman spectra of lysozyme functionalized nanodiamond solution and lysozyme functionalized nanodiamond arrays, respectively. As shown in the spectra, the functionalized nanodiamond solution exhibits both peaks of nanodiamond located at 1332 cm⁻¹ and lysozyme located at the region between 1400 cm⁻¹ and 1700 cm⁻¹. Within our expectation, the Raman spectrum of the NDs-lysozyme arrays on the silicon template is identical to the NDs-lysozyme complex in the solution. After placement of lysozyme functionalized nanodiamond arrays in room temperate for 24 hours, the Raman spectrum of lysozyme functionalized nanodiamond arrays (don't show here) is unidentifiable for

lysozyme Raman feature. It may interpret the activity of lysozyme functionalized nanodiamond arrays vanish under such condition.

The interaction of the stable and bioactive lysozyme functionalized nanodiamond arrays with bacteria can be verified and observed using SEM. For the observation of interaction between lysozyme functionalized nanodiamond arrays and E.coli, the nanodiamond arrays were designed into 1 μ m in length and 5 μ m in pitch. Figures 3-17 (a) and (b) show the SEM images that E.coli interaction with the lysozyme functionalized nanodiamond crossmarks and nanoarrays, respectively. From the SEM images, we clearly observed that the E.coli were morphologically damaged while absorbed on lysozyme functionalized nanodiamond arrays [3.16, 3.17]. Lysozyme is an enzyme, which hydrolyze the cell wall of the bacteria. The lysozyme proteins absorbed on the nanodiamond arrays still retained their antibacterial activity and interacted with the E.coli bacterial cells. As shown in the figure 3-17 (b), the E.coli only interacts with the lysozyme functionalized nanodiamond arrays. It can't be observed that E.coli interact with the silicon substrate without lysozyme functionalized nanodiamond arrays.

3-4 Summary

In this study, we have demonstrated new methods and techniques to anchor

bio-functionalized nanodiamond arrays on silicon template by using e-beam lithography and SAM techniques. The nanodiamond arrays can be functionalized by kinds of bio-molecules such as PLL and lysozyme proteins. The lysozyme proteins can functionalize the nanodiamonds and still retained their antibacterial activity and interacted with E. coli bacterial cells. The device demonstrated here is suitable for applications in bio-sensing chips and single bio-molecule patterning and detection. It facilitates the development of new applications of different bio-functionalized nanodiamond arrays that can interact with special targets, as well as the individual observation of their optical property.



3-5 Reference

- [3.1] Jui-I. Chao, Elena Perevedentseva, Pei-Hua Chung, Kuang-Kai Liu, Chih-Yuan Cheng, Chia-Ching Chang, and Chia-Liang Cheng, "Nanometer-Sized Diamond Particle as a Probe for Biolabeling," *Biophys. J.*, vol. 93, 2199, (2007)
- [3.2] Shu-Jung Yu, Ming-Wei Kang, Huan-Cheng Chang, Kuan-Ming Chen, and Yueh-Chung Yu "Bright Fluorescent Nanodiamonds: No Photobleaching and Low Cytotoxicity," *J. Am. Chem. Soc.*, vol. 127, 17604, (2005)
- [3.3] A.-Y. Jee, and M. Lee, "Surface functionalization and physicochemical characterization of diamond nanoparticles," *Curr. Appl Phys.*, vol. 9, e144, (2009)

- [3.4] V. Vaijyanthimala, and H.-C. Chang, "Functionalized fluorescent nanodiamonds for biomedical applications," *Nanomedicine*, vol. 4, 47, (2009)
- [3.5] J. Cooper McDonald, David C. Duffy, Janelle R. Anderson, Daniel T. Chiu, Hongkai Wu, Olivier J. A. Schueller, George and M. Whitesides¹, "Fabrication of microfluidic systems in poly(dimethylsiloxane)," *Electrophoresis*, vol. 21, 27, (2000)
- [3.6] Yi Cui, Qingqiao Wei, Hongkun Park, Charles M. Lieber, "Nanowire Nanosensors for Highly Sensitive and Selective Detection of Biological and Chemical Species," *Science*, vol. 293, 1289, (2001)
- [3.7] C.Y. Cheng, P.H. Chung, J.S. Tu, Y.H. Hsieh, and C.L. Cheng, "The interaction of the protein lysozyme with bacteria *E. coli* observed using nanodiamond labelling," *Nanotechnology*, vol. 18, 315102, (2007)
- [3.8] Kenneth S. Suslick, "Sonochemistry," *Science*, vol. 247, 1439, (1990)
- [3.9] Takeyoshi Uchida, Toshio Sato, Shinichi Takeuchi, Naimu Kuramochi and Norimichi Kawashima, "Basic Study on Dispersion and Surface Modification of Diamond Powders by Sonochemical Reaction," *Jpn. J. Appl. Phys.*, vol. 42, 2967, (2003)
- [3.10] A. Shavel, N. Gaponik, and A. Eychmuller, "Covalent Linking of CdTe Nanocrystals to Amino-Functionalized Surfaces," *Chem. Phys. Chem.*, vol. 6, 449, (2005)

- [3.11] L.C. Lora Huang and H.C. Chang "Absorption and immobilization of Cytochrome c on Nanodiamond," *Langmuir*, vol. 20, 5879, (2004)
- [3.12] T. Ando, S. Inoue, M. Ishii, M. Kamo, Y. Sato, O. Yamada, and T. Nakano, "Fourier-transform infrared photoacoustic studies of hydrogenated diamond surfaces," *J. Chem. Soc., Faraday Trans.*, vol. 89, 749, (1993)
- [3.13] P.-H. Chung, E. Perevedentseva, C.-L. Cheng, "The particle size-dependent photoluminescence of nanodiamonds," *Sur. Sci.*, vol. 601, 3866, (2007)
- [3.14] V. Vaijyanthimala, and H.-C. Chang, "Functionalized fluorescent nanodiamonds for biomedical applications," *Nanomedicine*, vol. 4, 47, (2009)
- [3.15] T. T. B. Nguyen, H. C. Chang, and V. W. K. Wu, "Adsorption and hydrolytic activity of lysozyme on diamond nanocrystallites," *Diamond Relat. Mater.*, vol. 16, 872, (2007)
- [3.16] C.N. Pace, F. Vajdos, L. Fee, G. Grimsley, and T. Gray, "Crystallization and preliminary X-ray analysis of fructose 6-phosphate, 2-kinase:fructose 2,6-bisphosphatase," *Protein Sci.*, vol. 4, 2411, (1995)
- [3.17] H.R. Ibrahim, M. Yamada, K. Matsushita, K. Kobayashi, and A. Kato, "Enhanced bactericidal action of lysozyme to Escherichia coli by inserting a hydrophobic pentapeptide into its C terminus." *J. Biol. Chem.*, vol. 269, 5059, (1994)

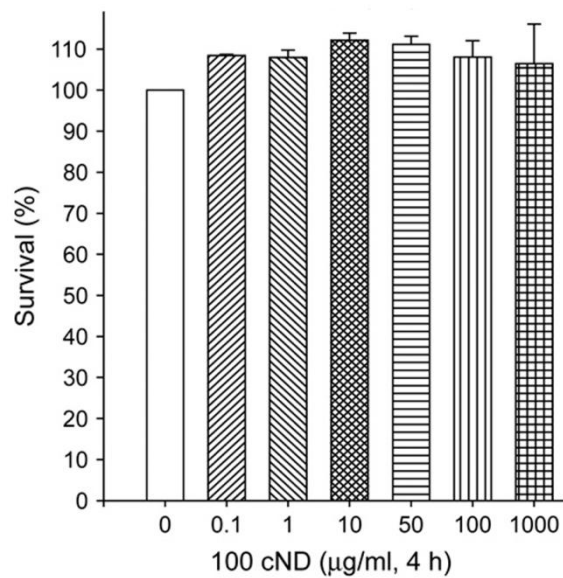


Figure 3-1: Cytotoxicity test of nanodiamonds [3.1]

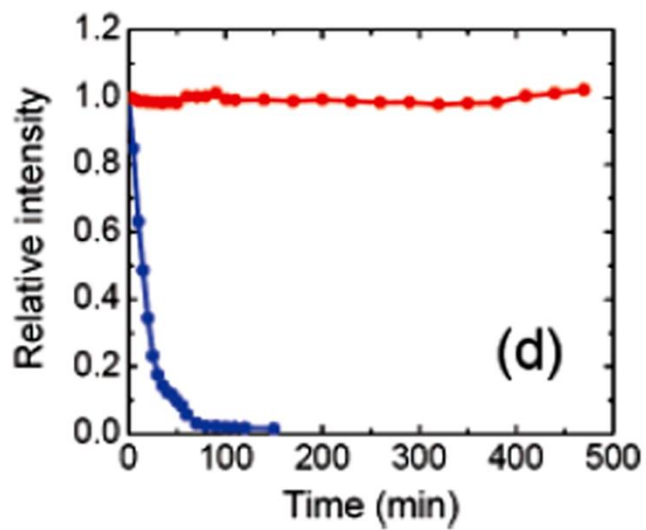


Figure 3-2: Photostability test of nanodiamond [3.2]

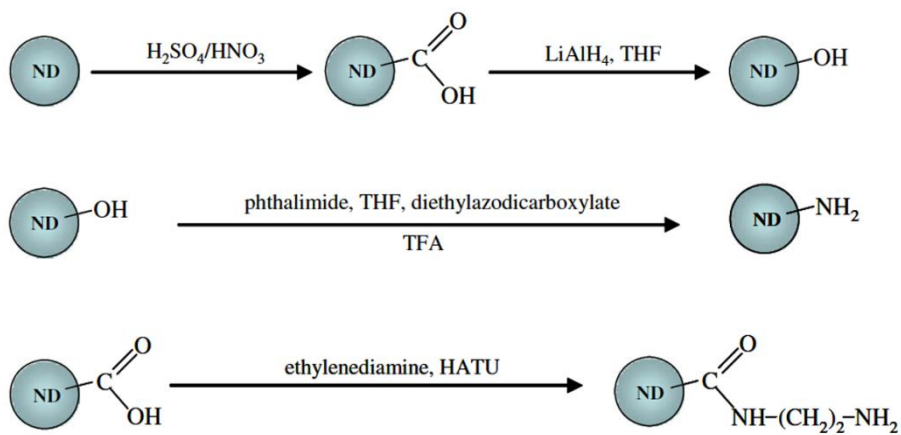


Figure 3-3: Synthetic route for functionalized nanodiamonds [3.3]

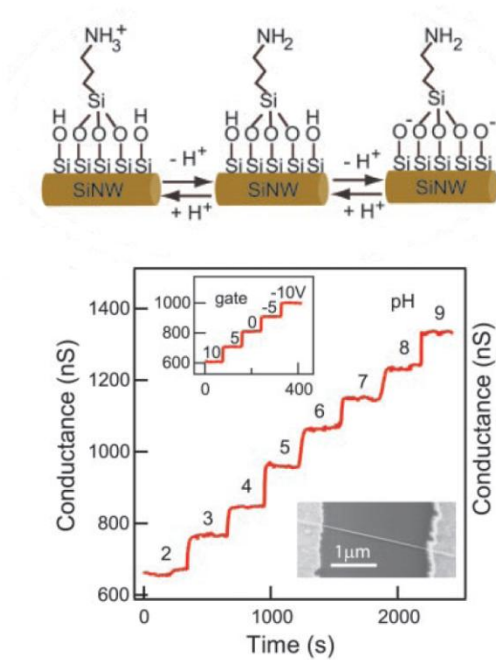


Figure 3-4: Electric properties of surface modified silicon nanowire were changed

under the variation of pH value [3.6]

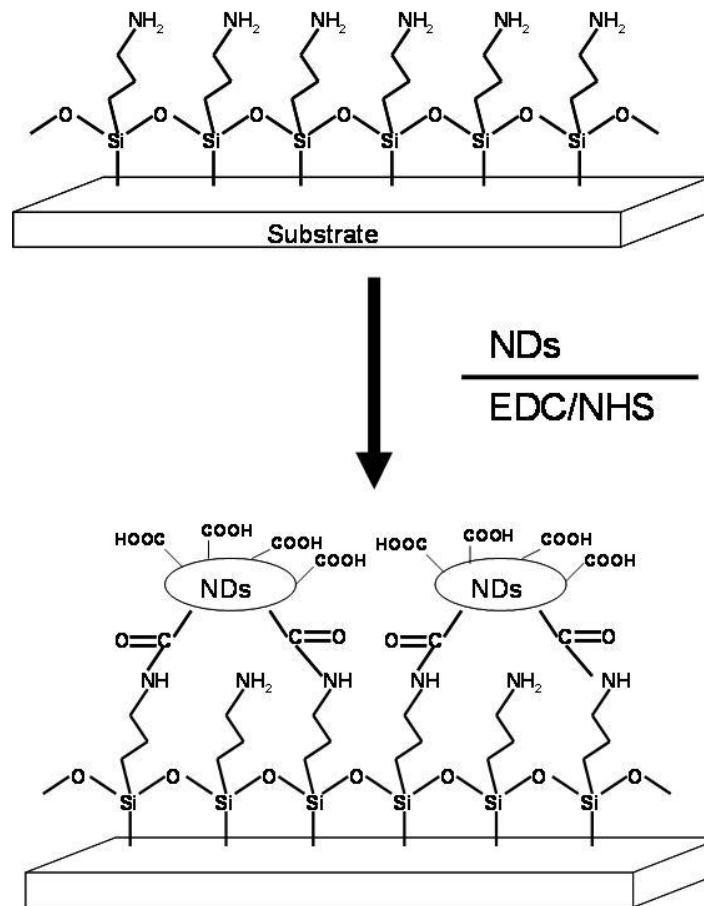


Figure 3-5 (a): Schematics of the functionalized NDs bonded to the SAM substrates

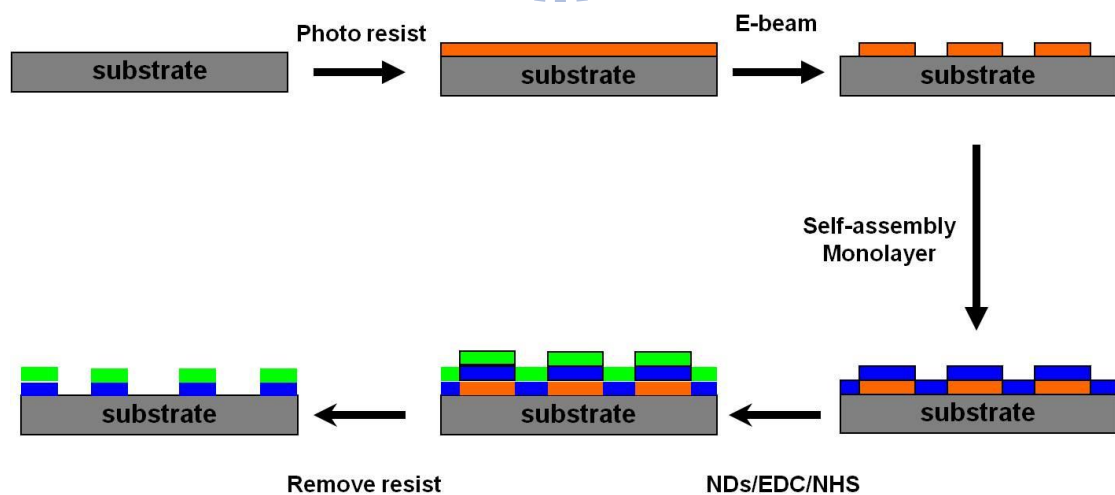


Figure 3-5 (b): Schematics of flow chart of the template fabrication processes

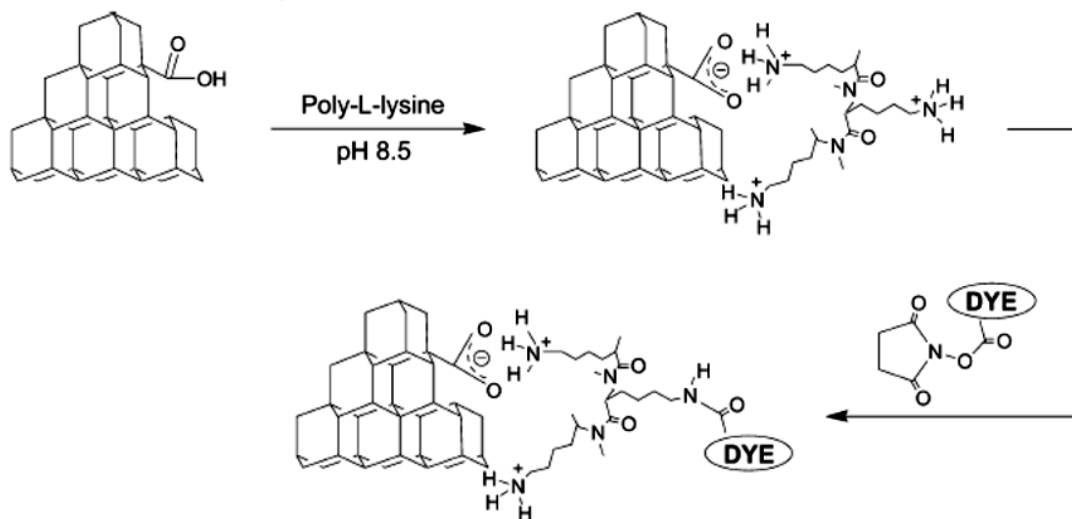
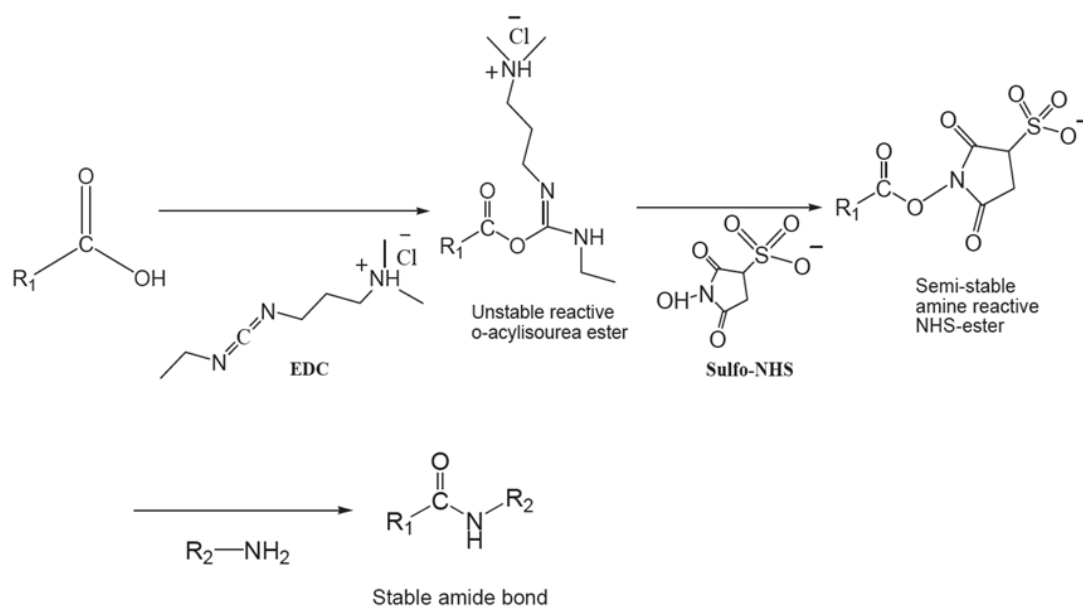


Figure 3-6: Schematic proceeding of the FITC functionalized NDs [3.11]

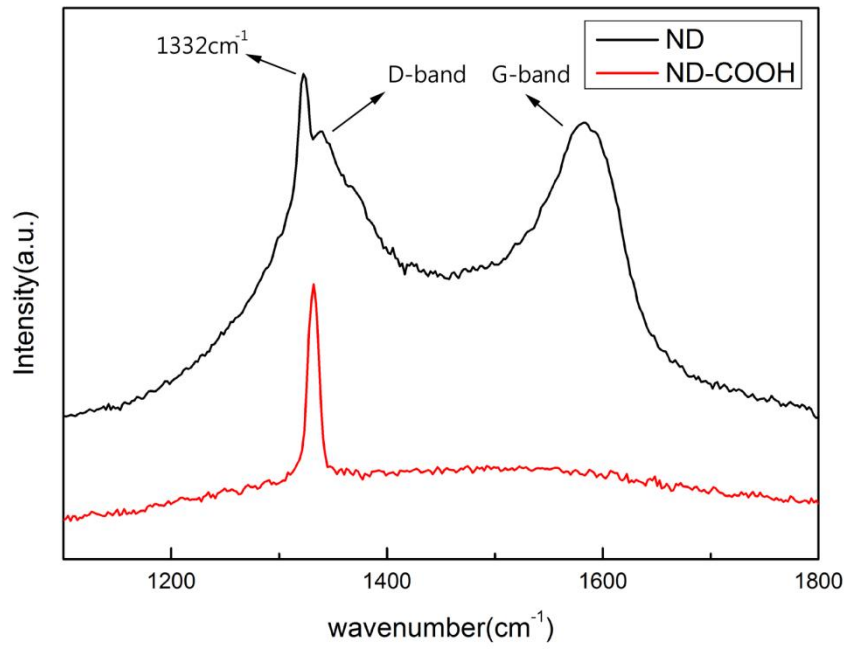


Figure 3-7 (a): Raman spectra of NDs with and without the acid treatment

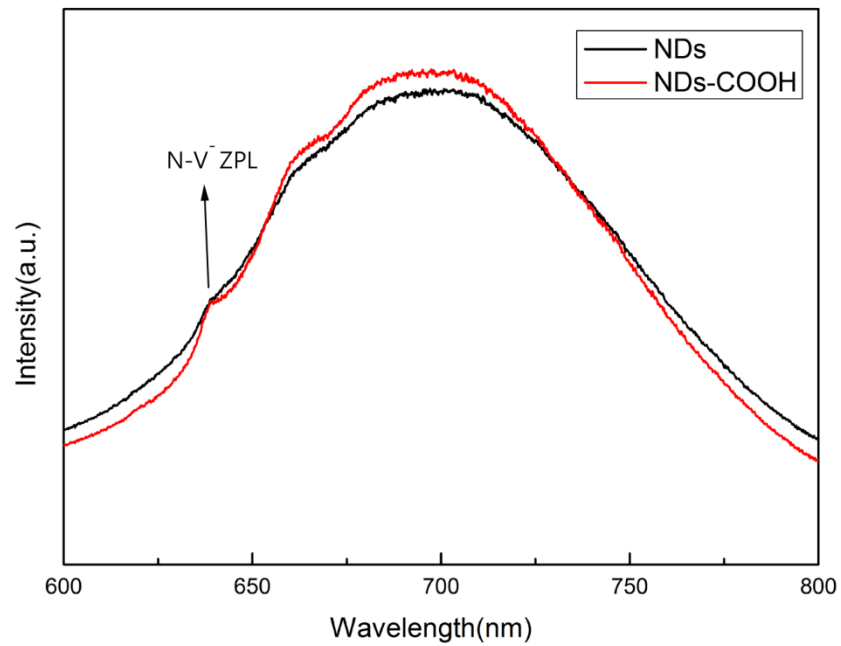


Figure 3-7 (b): Raman spectra of NDs with and without the acid treatment

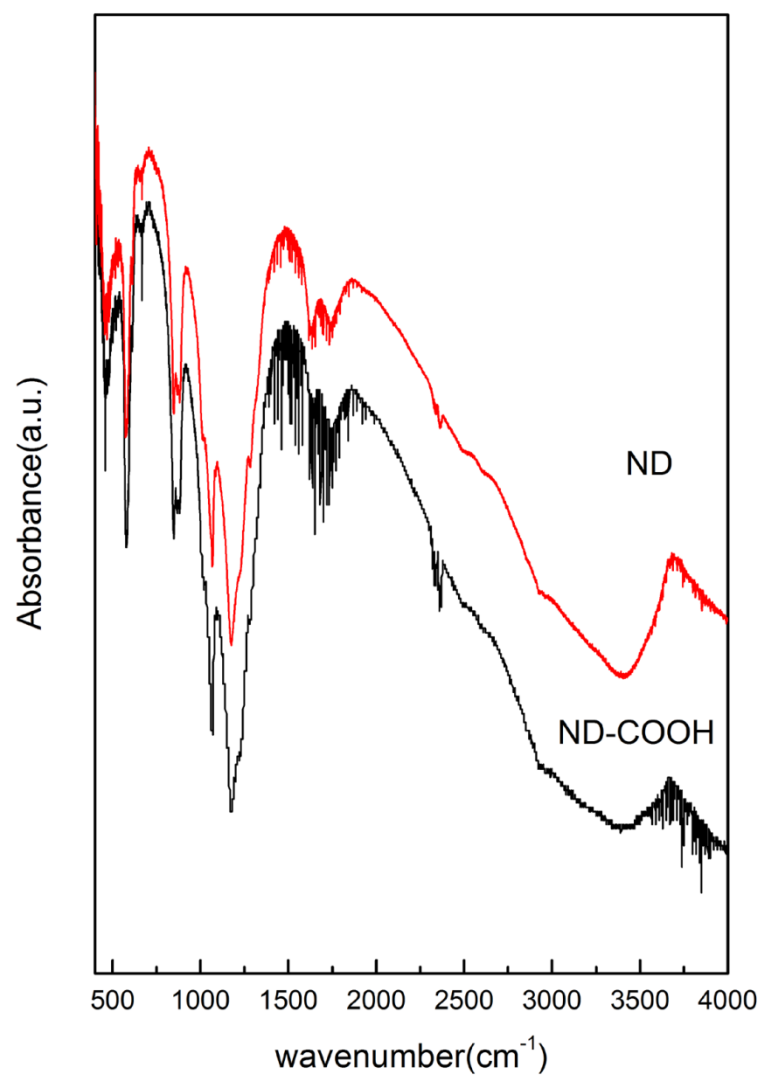


Figure 3-8: FTIR spectra of NDs with and without the acid treatment

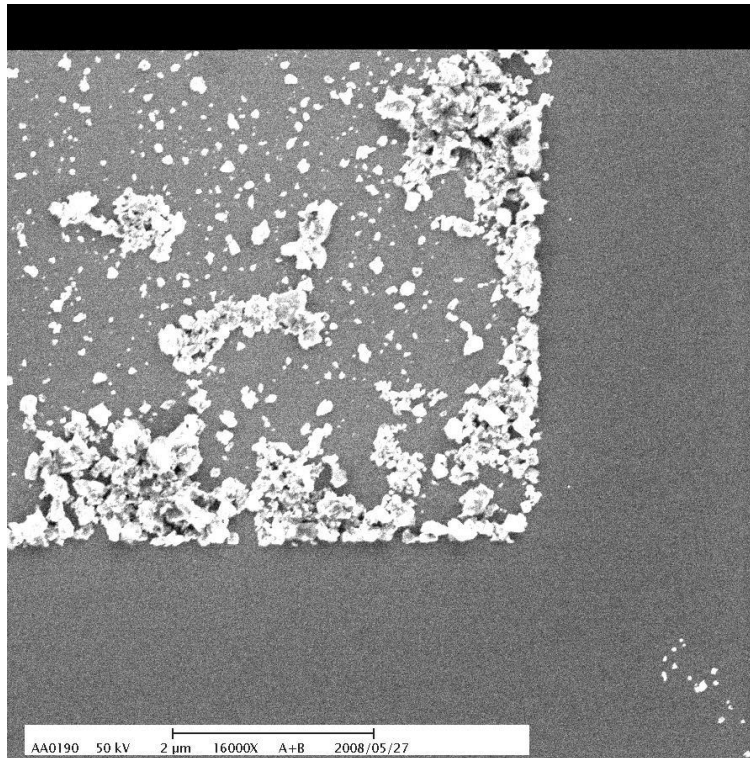


Figure 3-9 (a): SEM images of one of the corners of the cross marks

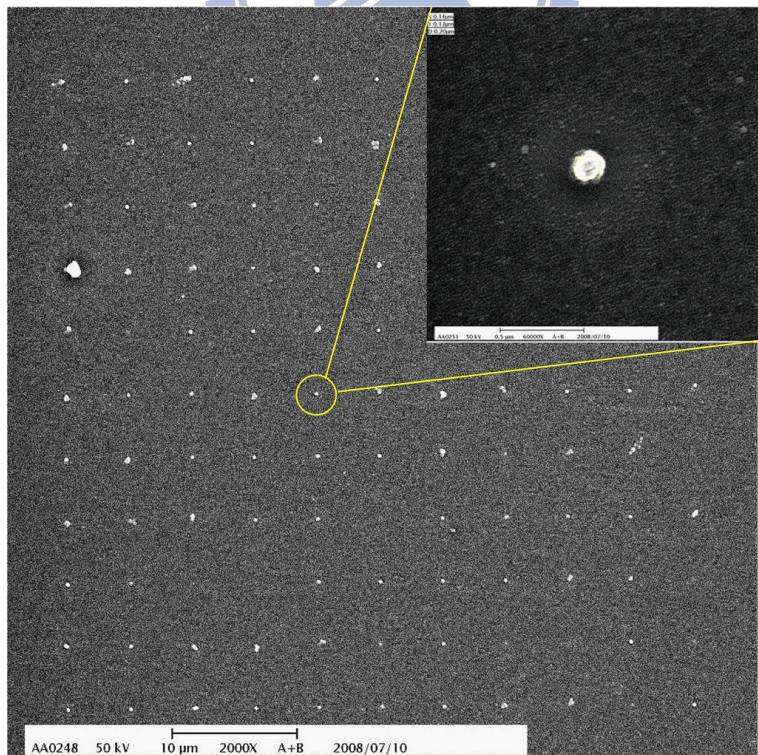


Figure 3-9(b): SEM images of the nano holes array

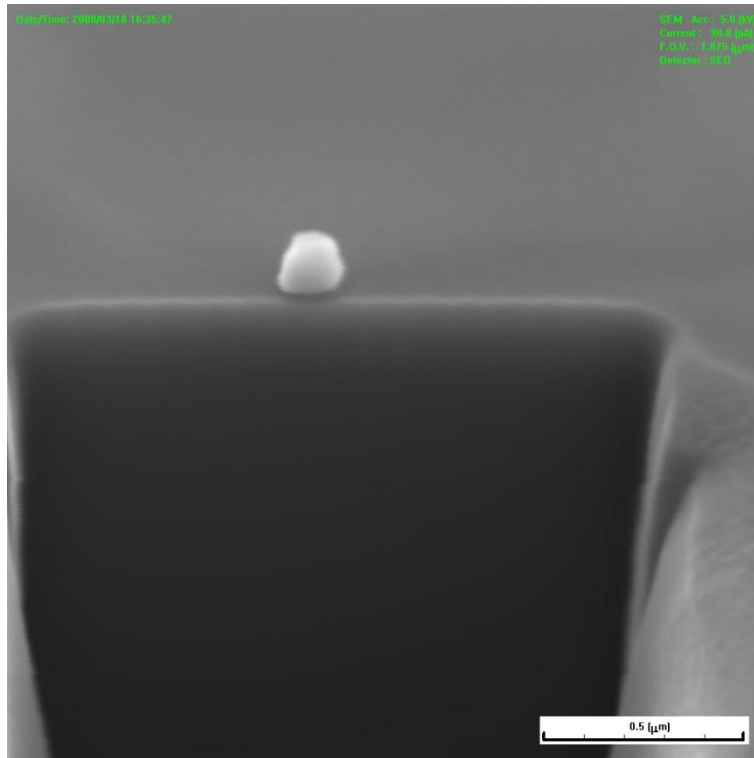


Figure 3-10(a): SEM images of the cross-section of a patterned single nanodiamond

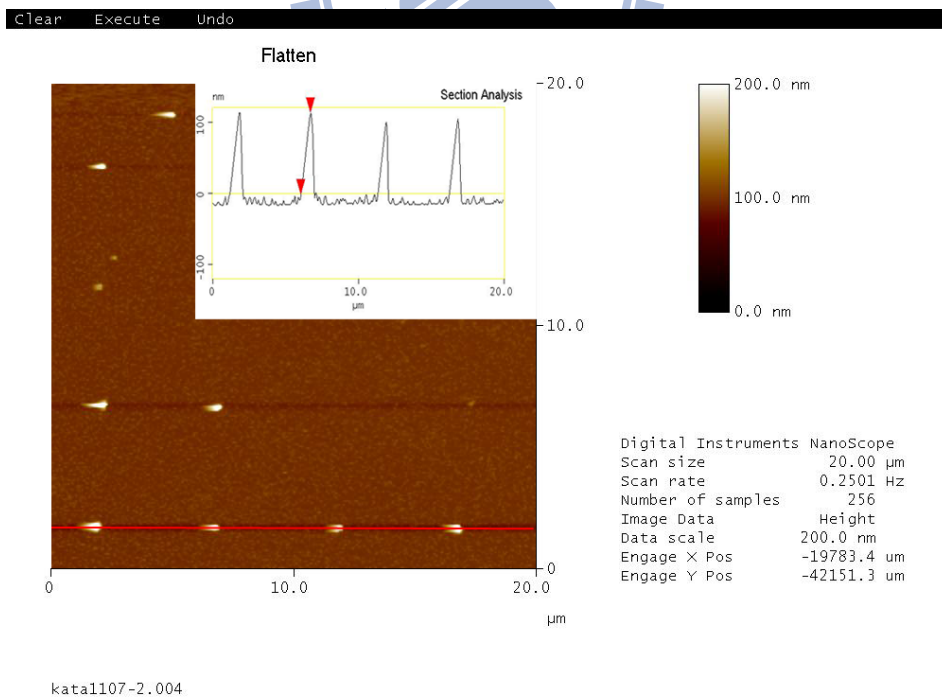


Figure 3-10(b): AFM images of patterned single nanodiamond arrays

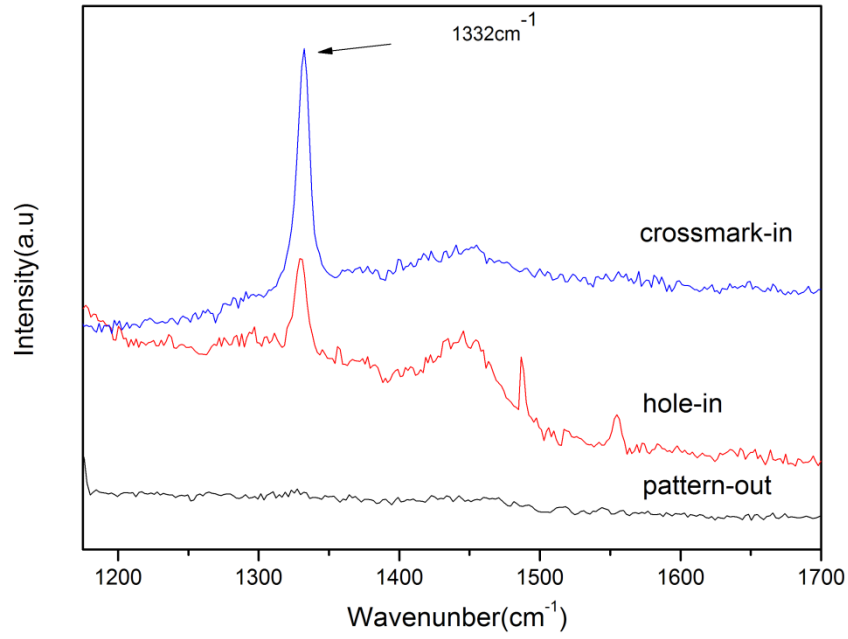


Figure 3-11(a): Raman spectra of pattern-in and pattern-out area

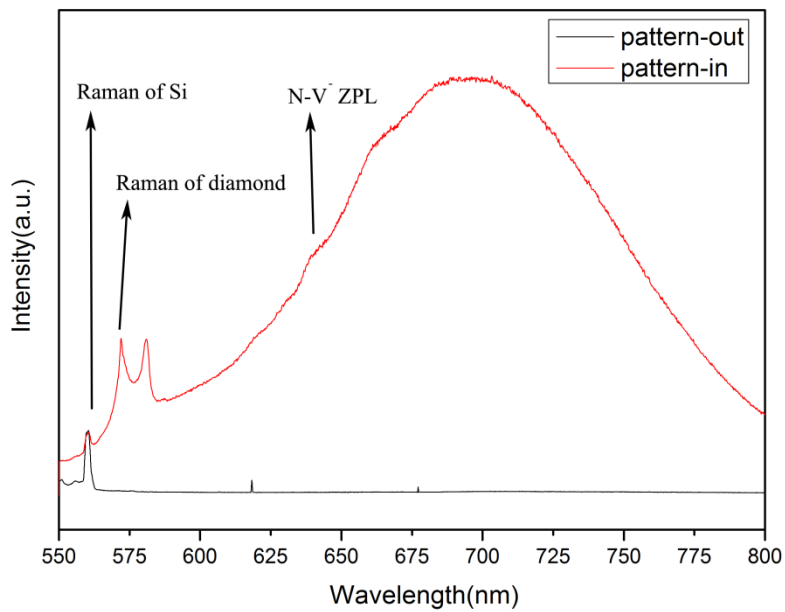
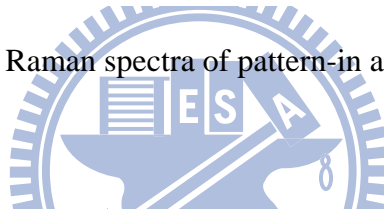


Figure 3-11(b): PL spectra of pattern-in and pattern-out area

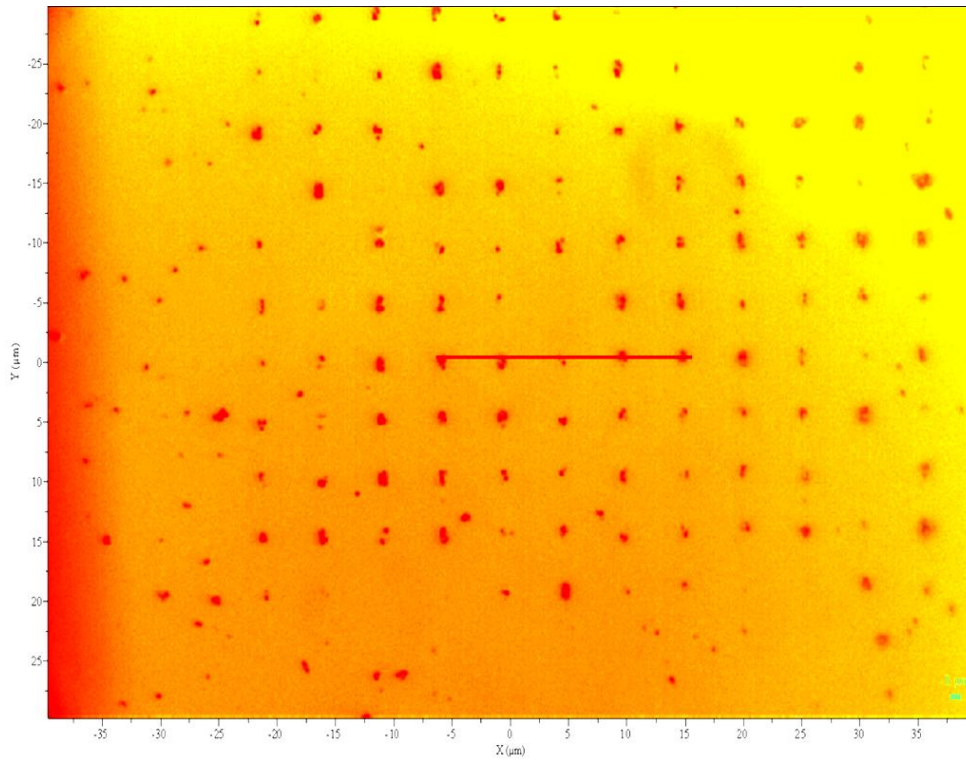


Figure 3-12(a): Optical image of the nanodiamond arrays of 1D mapping area, indicated by the straight line

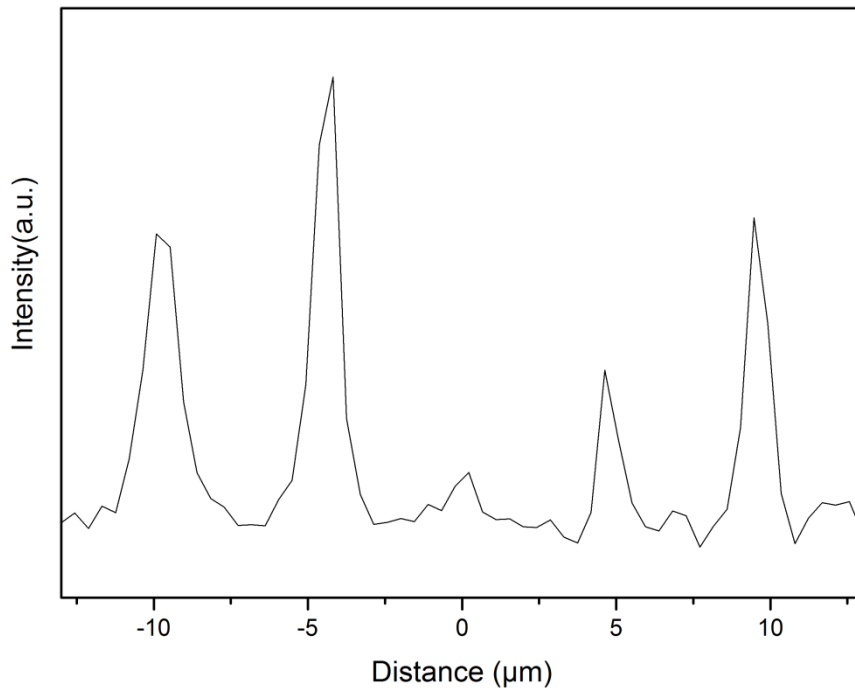


Figure 3-12(b): Image of the 1D Raman intensity mapping

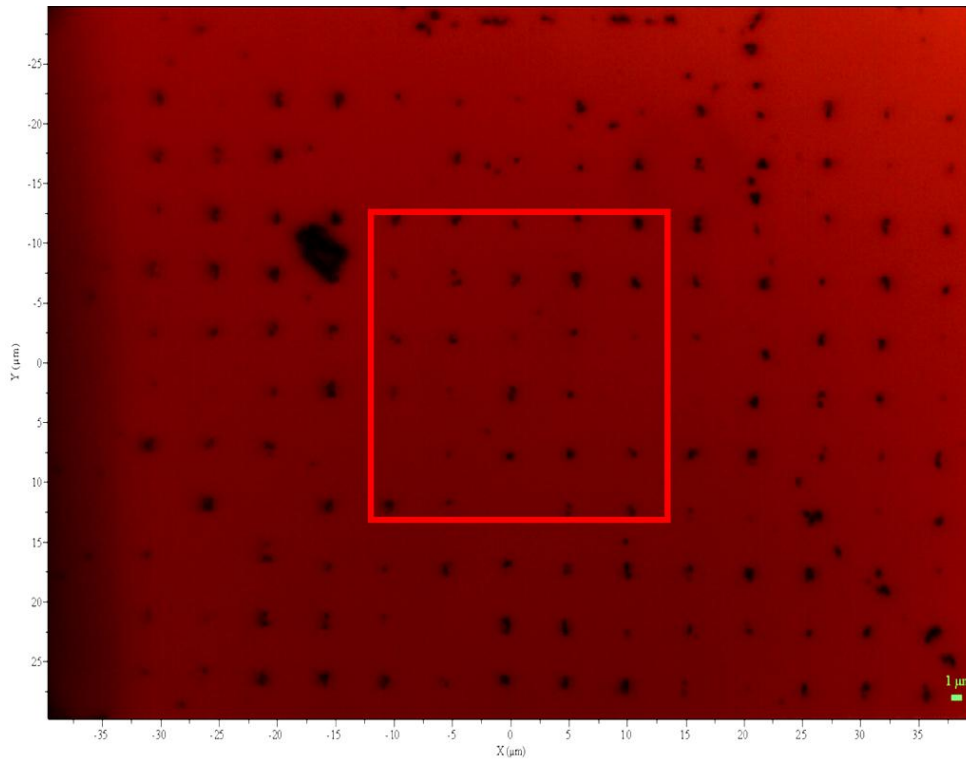


Figure 3-13(a): Optical image of nanodiamond arrays of the 2D mapping area, indicated by the square

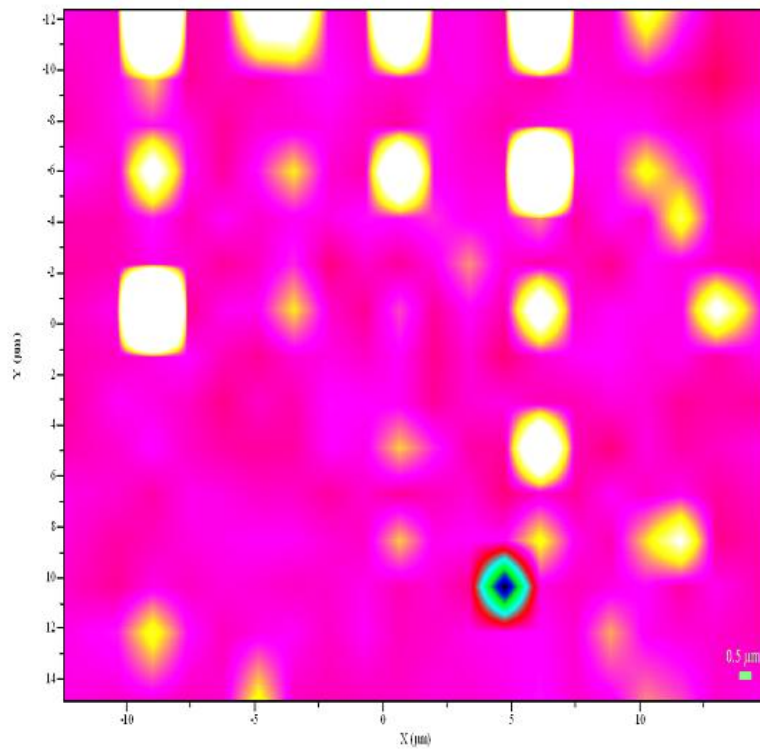


Figure 3-13(b): Image of the 2D Raman intensity mapping

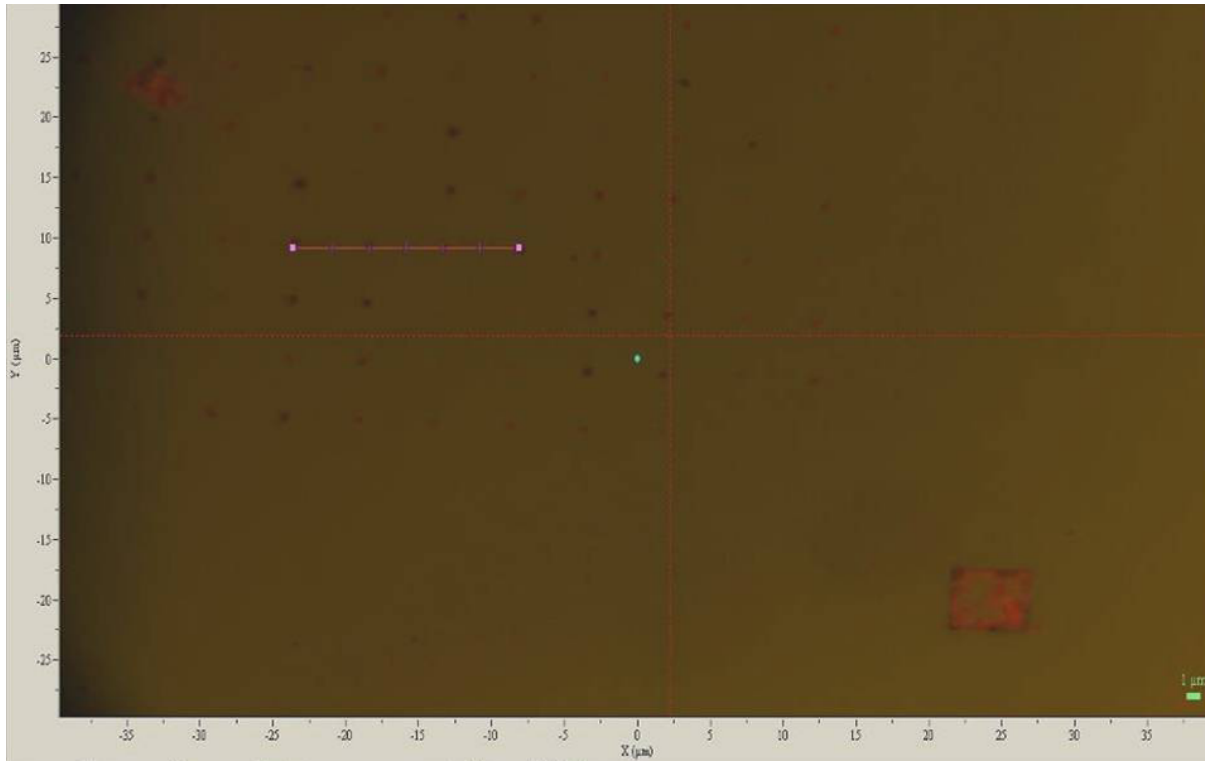


Figure 3-14(a): Optical image of the 1D mapping area, indicated by the straight line

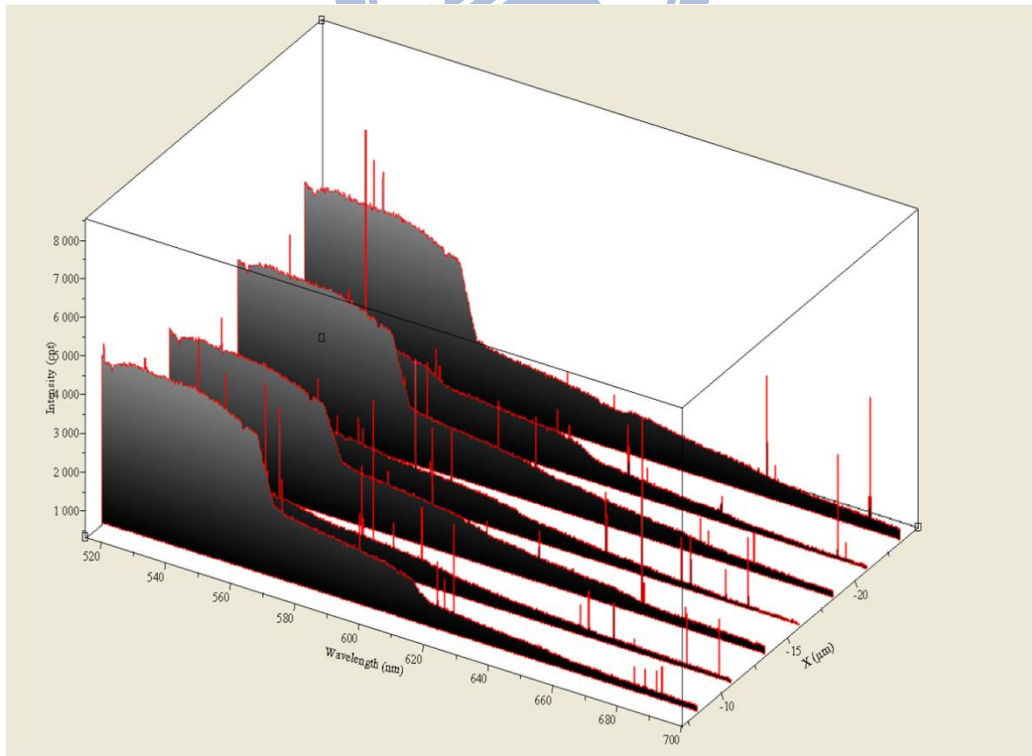


Figure 3-14(b): Image of the 2D PL intensity mapping.

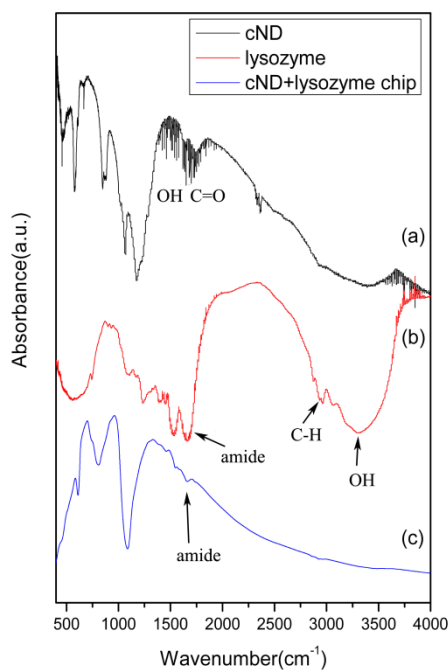


Figure 3-15: IR spectra of three different samples (a) cND (b) lysozyme and (c)

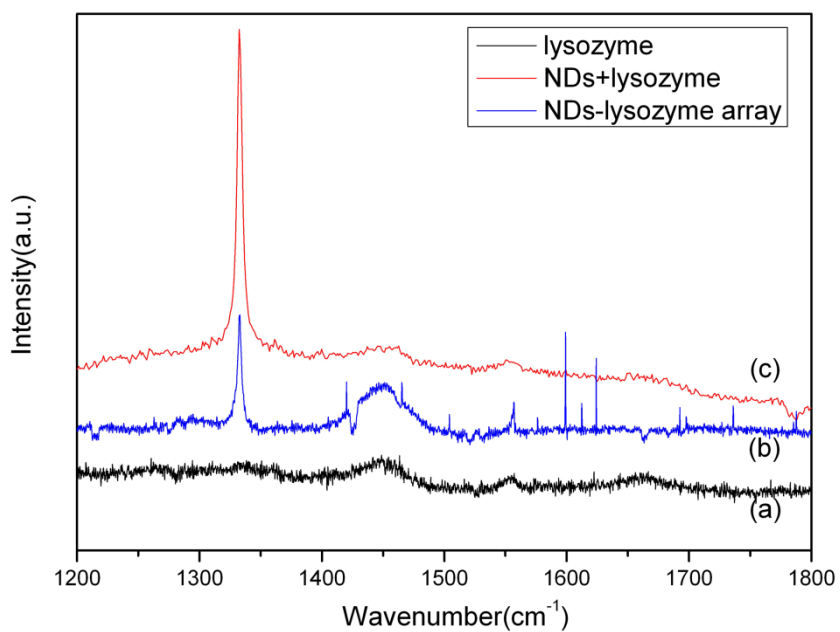


Figure 3-16: Raman spectra of three different samples (a) lysozyme (b)

lysozyme-cND complex in the solution (c) cND-lysozyme chip

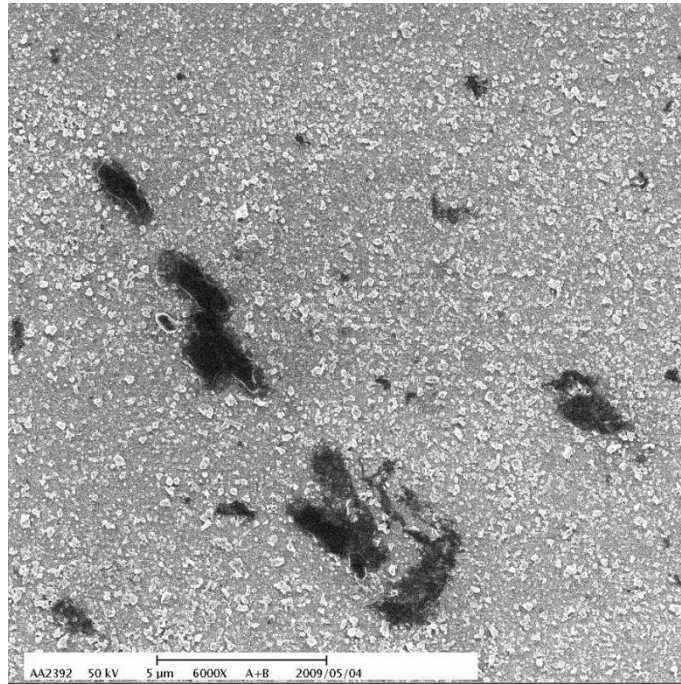


Figure 3-17(a): SEM images of E.coli interaction with ND-lysozyme film on

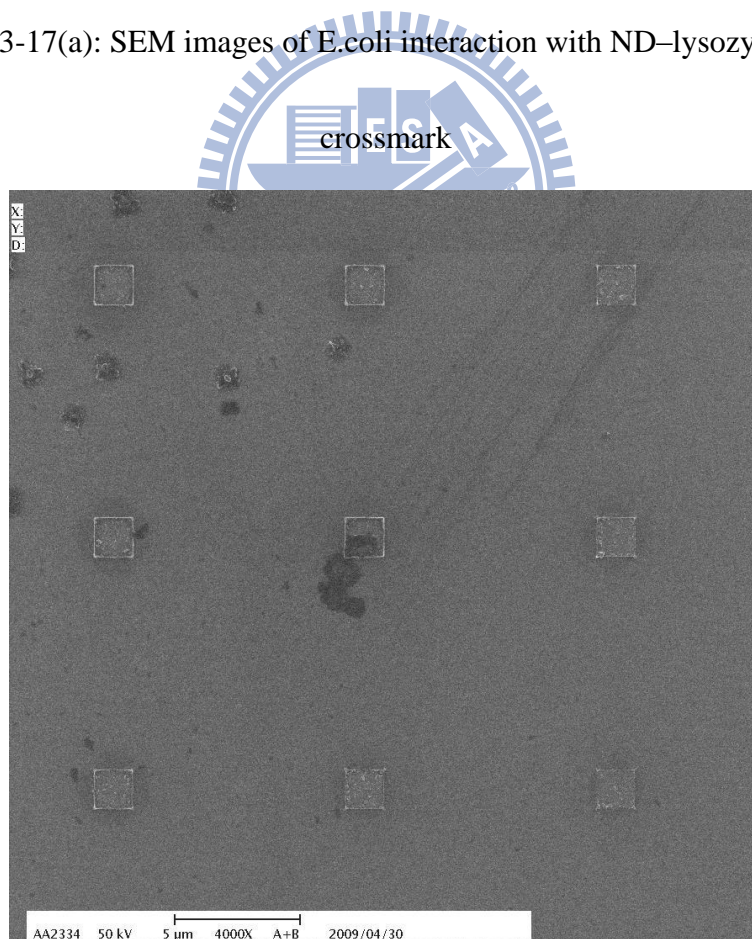


Figure 3-17(b): SEM images of E.coli interaction with ND-lysozyme film on

nanoarrays

Chapter 4 Photoluminescence enhancement of bioconjugated gold

nanoparticle and nanodiamond assembly

4-1 Literature review

Noble metal nanocrystals are known to enhance photoluminescence and Raman signals due to surface plasma resonance efficiency. Surface plasmons are coherent electron oscillations that exist at the interface between any two materials where the real part of the dielectric function changes sign across the interface (e.g. a metal-dielectric interface). Since the wave is on the boundary of the metal and the external medium, these oscillations are very sensitive to any change of this boundary, such as the adsorption of molecules to the metal surface. Localized surface plasmon polaritons (LSPRs) are collective electron charge oscillations in metallic nanoparticles that are excited by light. They exhibit enhanced near-field amplitude at the resonance wavelength. This field is highly localized at the nanoparticle and decays rapidly away from the nanoparticle / dielectric interface into the dielectric background, though far-field scattering by the particle is also enhanced by the resonance.

The interactions between plasmonic metal nanocrystals and materials give rise to very interesting phenomenon, including fluorescence enhancement, fluorescence

quenching, and molecular-plasma resonance. For example, a gold nanoparticle supports plasma resonances associated with the excitation of a collective oscillation of electrons. The scattering properties and the plasma spectra of small gold nanoparticles make them behave as an elementary resonant dipole antenna. This near field enhancement has been exploited and employed to amplify Raman scattering (SERS), fluorescence, photocurrent, and light absorption. This technique has become popular in recent years due to the importance of the fluorescence-based measurements in various fields, such as chemistry, bio-molecular materials science, and medicine. The ability to increase the fluorescence emission can greatly improve the effectiveness of fluorescence-based applications, such as single molecular detection and sensing in biology. Figure 4-1 demonstrated that the fluorescence of indocyanine green (ICG) dye molecules could be enhanced by metallic nanoparticles [4.1].

4-2 Fabrication of bioconjugated gold nanoparticle and nanodiamond assembly

4-2-1 Preparation of nano assembly

The average diameter of the nanodiamond (ND) powder used in our experiments is about 100nm (General Electric company, USA). The particle size is confirmed by SEM. The 0.15g nanodiamond powder was treated with the 160ml 5:1 mixture of

concentrated H_2SO_4 and HNO_3 solutions at $75\text{ }^\circ\text{C}$ for 1 hour in ultrasonic bath for dispersion and stir for 11 hours for carboxylated reaction, and extensively rinsed several times with DI water and dry. The sediment was then collected and dried. The functional COOH group was formed on the ND surface followed by the standard chemical treatment mentioned above. The surface functional carboxylated group of nanodiamonds was checked by Fourier transform infrared and Raman spectroscopy.

The acoustic cavitation generated by ultrasonic bath heats up the water to make the dissociation of water into H^+ and OH^- ions. While the OH^- ions adsorb on the surface of nanodiamonds, the increasing of electric charges on nanodiamond surface induce a coulomb repulsion force between nanoparticles. Therefore, the clustering of nanodiamonds can be avoided. The NDs solution was prepared by adding 0.1 g of carboxylated functionalized NDs into 100 ml of deionized water followed by an ultrasonic bath for 60 min.

The DNA sequences were made by primer (Oligo) synthesis (Bio Basic Inc). One DNA sequence was modified SH group and the other one was modified NH_2 group at 5' end and purification by HPLC. The two DNA sequences were designated as 5'-H₂N-GGAATTCCATATGGAATTCC (labeled as DNA1) and 5'-HS-GGAATTCCATATGGAATTCC (labeled as DNA2). The concentration of the DNA solution was $10\text{ }\mu\text{M}$.

The gold nanoparticles (Ted Pella, Inc.) were dissolved in a sodium citrate solution, and the concentration of gold nanoparticles was 0.01% by weight. The sizes of the gold nanoparticles used in this experiment were 13, 30, 50, and 80 nm, respectively.

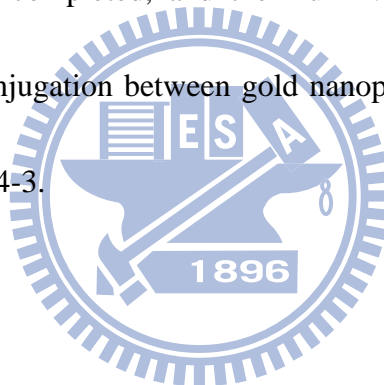
4-2-2 Conjugation of gold nanoparticle with nanodiamond

The solution consisting of 80 μl of gold nanoparticles was mixed with 20 μl of DNA2 solution to react for 12 hours. Then, 40 μl of 10 mM PSB buffer was added to react for 4 hours, after which 60 μl of 0.05 M NaCl was added for another 4-hours reaction to complete the Au-DNA2 solution.

We took 5 μl of NDs solution and mixed it with 5 μl of MES (2-(N-morpholino)ethane sulfonic acid), 10 μl of EDC (1-ethyl-3-[3-(dimethylamino)propyl]carbodiimide hydrochloride), 10 μl of NHS (N-hydroxysuccinimide), and 10 μl of DNA1 to react for 4 hours. The solution was then centrifuged, and the precipitations were collected and dissolved in 100 μl of DI water; we shall refer to this as the ND-DNA1 solution for the rest of this chapter. The adsorption of DNA1 on the ND surface was further verified using the Healthview Nucleic Acid Stain (Genomics) as a probe. When the Healthview Nucleic Acid Stain binds to DNA, it can emit fluorescence; our ND-DNA1 and Au-DNA2 solutions were allowed to react with this stain for 30min. The solution was then centrifuged and washed for several times. Figure 4-2 indicates the spectra of ND-DNA1 and

Au-DNA2 solutions were allowed to react with Healthview Nucleic Acid Stain. With laser excitation, the fluorescence emitted from the Healthview Nucleic Acid Stain was detected, confirming that the DNA1 and DNA2 were indeed linked with the NDs and AuNPs.

Next, 100 μ l of ND-DNA1 solution was mixed with 100 μ l of Au-DNA2 solution. Once the ND-DNA1 and Au-DNA2 solution was hybridized for 24 hours, it was centrifuged to wash out uncoupled gold nanoparticles. Finally, the ND and gold nanoparticle coupling was completed, and the Au-DNA-ND hybrid structure was formed. The scheme of conjugation between gold nanoparticle and nanodiamond by DNA was shown in Figure 4-3.



4-3 Results and discussion

4-3-1 Gold nanoparticle and nanodiamond assembly

Figure 4-4(a), (b), (c), and (d) shows the SEM images of the hybrid structures of NDs coupled with the 13 nm, 30nm, 50nm, and 80nm gold nanoparticles, respectively. Under the SEM images, nearly all of the gold nanoparticles were properly anchored on the NDs for all kinds of size gold we used after the extra unbounded gold nanoparticles were washed away with centrifugation for several times, indicating that

the NDs were well bonded with the gold nanoparticles with the DNA linker. The bonding force was also strong enough to hold the hybrid structures during the centrifugation processes. Without DNA linker (figure 4-5), there is no strong bonding between gold nanoparticle and ND. The gold nanoparticles were washed away with centrifugation.

Figure 4-6 shows the HRTEM image of the 30 nm gold nanoparticle binding with an ND. Under this TEM image, the gold nanoparticle was completely placed on the top of the ND surface and there was no gap in between them, even though the DNA sequence had a length of 6 nm. After performing the test with a longer DNA sequence with a length of 20 nm (the results are not shown here), the TEM images also showed the close contact of the gold nanoparticle with the ND surface. There are several reasons that can explain our TEM results. The density of the carboxylated group on the ND surface was about 7% [4.2, 4.3], leading to the limited number of DNA linkers established on the ND surface. Due to the hydrophobic adsorption, DNA molecules that grafted onto the nanoparticle surface may be expected to stay flat [4.4-4.6]. Another explanation could be that the stiffness of DNA was about 10 pN/um [4.7-4.9]. Due to the limited number of DNA sequences, they were not stiff enough to hold against the static attraction force in between the ND and gold nanoparticles. Therefore, the DNA sequences bended and allowed the gold nanoparticles to come in contact

with the ND.

4-3-2 Optical properties

A confocal microscope was used to allocate an isolated hybrid structure. The PL signals were collected through the microscope objective and are analyzed using a spectrometer equipped with a liquid nitrogen (LN)-cooled CCD detector at the excitation wavelength of 488 nm. The excitation power density from the diode-pumped solid state (DPSS) laser was controlled under 10 KW/cm^2 . The optical signal was further optimized by adjusting the focal plane position along the z-axis via the piezo-driven objective lens.

The luminescence properties of all tested nanoparticles were investigated individually before the coupling procedure was started. Figure 4-7(a) shows the luminescence properties of the NDs and 13 nm gold nanoparticles with and without coupling to a single string of DNA sequence at an excitation wavelength of 488 nm. In our experiments, optical excitation of gold nanoparticles showed a lack of or very weak luminescence. In an earlier report, the smooth gold films have a photoluminescence efficiency of only $\sim 10^{-10}$ following the excitation of electron from 5d to 6sp levels [4.10]. The poor luminescence efficiency can be attributed to the non-radiative energy relaxation processes of the photoexcited carriers, which is able to quench the photoluminescence. This could explain why the luminescence intensity

of ~ 520 nm was undetectable for our gold nanoparticles; the peak that appeared at 590 nm was the Raman signal from the buffer solution. The luminescence spectrum of the NDs and the PL peak assignment are given in Figure 4-7(a). The broad emission band consisted of two zero phonon emissions and several phonon band replicas from $[(N-V)^0]$ and $[(N-V)^-]$ [4.11-4.13]. The PL peaks at 575 and 638 nm originated from the $[(N-V)^0]$ and $[(N-V)^-]$ states [4.14-4.16], respectively. Peaks that appeared at 596[4.17], 660, and 680[4.18] nm were divacancy-related phonon replica bands of the $[(N-V)^0]$ and $[(N-V)^-]$ states. There was almost no change in luminescence intensity and lineshape when the ND and gold nanoparticles were respectively coupled with DNA1 and DNA2 sequences, as shown in Figure 4-7 (a). The plasmon resonance frequencies of our gold nanoparticles with sizes of 13, 30, 50, and 80 nm were determined to be at 520, 525, 535, and 550 nm, respectively, according to the absorption spectra shown in Figure 4-7(b).

4-3-3 Photoluminescence enhancement of Au-DNA-ND assembly

In the next step, we begin our optical investigations on Au-DNA-ND hybrid structures. The hybrid structures coupled with different Au particle sizes were excited with a laser operated at 488 nm through a confocal microscope. The luminescence was collected through the objective and analyzed with a 0.8 m spectrometer equipped with an LN-cooled CCD detector. The spectra of all four samples are plotted in

Figures 4-8(a)-(d). The PL spectra of pure NDs are also presented in parallel for comparison. We observed strong modification on the luminescence intensity profiles of the hybrid structures between 525-650 nm compared with the pure ND. In the case of 13 nm gold nanoparticles, the emission from the $[(N-V)^0]$ state was significantly enhanced than that from the $[(N-V)^-]$ state. This was due to the plasma resonance (\sim at 520 nm) of 13 nm Au nanoparticles, which was closer to the emission energy of the $[(N-V)^0]$ state. Therefore, stronger enhancement on the PL intensity from the $[(N-V)^0]$ state emission was observed in smaller gold nanoparticles. As we increased the nanoparticles' sizes with their plasma resonances moving closer to the $[(N-V)^-]$ state emission, enhancement on the longer wavelength part of the PL was observed [Figures 4-8(b)-(d)]. Therefore, the profile of the enhanced PL could be altered depending on the sizes of the gold nanoparticles attached.

Our hybrid structures can be disassembled using a particular enzyme called restriction enzyme. A restriction enzyme cuts double-stranded or single-stranded DNA at specific recognition nucleotide sequences. If we let our hybrid structures interact with the NdeI restriction enzyme, the link between the ND and gold nanoparticles can be disconnected. Therefore, the enhancement of PL should be deactivated because of the breaking of the DNA linkers. Scheme of how the hybrid structures can be cut by the NdeI restriction enzyme is shown in Figure 4-9. The SEM

image (as shown in Figure 4-10) of the hybrid structures after interacting with the NdeI restriction enzyme indicates that most of gold nanoparticles are removed from the NDs. PL spectra of the hybrid structures with the attached 13 nm gold nanoparticles removed by interacting with the NdeI restriction enzyme is given in Figure 4-11. Although our hybrid structures had a pH environment of 6.5, which did not match the restricting enzyme's ideal pH environment (the enzyme had a cutting rate of nearly 95% at pH = 8.5 and at a temperature of 35 °C), the PL enhancement was strongly suppressed when the gold nanoparticles were detached from the NDs (as shown in Figure 4-11). This again proves that the enhanced PL is solely due to the plasmon resonance from the gold nanoparticles.

For the time-resolved measurements, a pulsed diode laser was used as the excitation source at a wavelength of 405 nm; the pulse duration was 100 picosecond with a repetition rate of 10 MHz and an excitation density in the range of 1-100 W/cm². The time-resolved PL signal was analyzed with a 0.55 m spectrometer and detected by a micro-channel photomultiplier with a time-correlated single-photon counting setup. The overall spectral resolution and system response were 0.1 meV and 300 picosecond, respectively.

From time-resolved measurements, we obtained an excited state decay rate of the emission at 575 and 638 nm, corresponding to the emission maximum of the [(N-V)⁰]

and $[(N-V)^-]$ states, respectively. The time-resolved spectra for the bare ND, ND bound with DNA1, and the hybrid structures bound with 13 nm Au nanoparticles are shown in Figure 4-12. In contrast to the earlier reports, we extracted a much faster decay time of ~ 0.38 ns for the bare ND at room temperature. The time-resolved spectrum of the ND-DNA1 was almost overlapped with that of the bare ND spectrum. However, for the hybrid structures, we obtained a slight increase of the excited state decay rate by a factor of 1.5, which was probably limited by the system response. The decay rate of the hybrid structures also showed no dependence on the size of the Au nanoparticle attached. The faster decay times observed in the luminescence were probably due to the shorter excitation wavelength used in our measurements. The PL of nanodiamonds was found to be size and laser excitation wavelength dependent due to two competitive origins: the surface states [4.19-4.21] and vacancy centers in bulk diamond phase. When nanodiamonds are excited with short wavelengths, the radiation recombination will be affected by the continuously distributed energy levels in the bandgap arising from the surface states (or structural inhomogeneities). The ultrafast optical emission with a decaytime of 60 ps in ultrafine nanodiamonds was reported under pulsed laser excitation of 300 nm. It was attributed to the surface states and large surface-to-volume ratio of nanoparticles. We speculate that, with an excitation of 405 nm, carriers are excited in or above the surface defect states and

have an effect on the radiative transitions and PL lifetimes from the vacancy centers.

A thorough investigation on the excitation wavelength dependence of the PL decaytimes is required to clarify this issue.

4-4 Summary

In summary, we demonstrated the coupling of ND with gold nanoparticles using DNA sequences as a linker. PL due to the presence of the N-V centers [the $(N-V)^0$ and $(N-V)^-$ states] in the NDs was enhanced when the gold nanoparticles with various sizes were attached. The PL profile was modified in different ways when the gold nanoparticles with different plasmon resonances (or different sizes) were bound to the NDs via the DNA linkers. We also demonstrated that enhancement mechanism can be deactivated by detaching the gold nanoparticles from the ND via interaction with the NdeI restriction enzyme. The approach can also be extended to other color center and metal nanoparticles, thereby providing a method for bio chip and bio-molecular detection.

4-5 Reference

[4.1] Felicia Tam, Glenn P. Goodrich, Bruce R. Johnson, and Naomi J. Halas,

"Plasmonic Enhancement of Molecular Fluorescence," *Nano Lett.*, Vol. 7, 496, (2007)

[4.2] V. Vaijayanthimala, and H.-C. Chang, "Functionalized fluorescent nanodiamonds for biomedical applications," *Nanomedicine*, vol. 4, 47, (2009)

[4.3] T. T. B. Nguyen, H. C. Chang, and V. W. K. Wu, "Adsorption and hydrolytic activity of lysozyme on diamond nanocrystallites," *Diamond Relat. Mater.*, vol. 16, 872, (2007)

[4.4] Z. Gagnon, S. Senapati, J. Gordon, and H. C. Chang, "You have full text access to this content Dielectrophoretic detection and quantification of hybridized DNA molecules on nano-genetic particles," *Electrophoresis*, vol. 29, 4808, (2008)

[4.5] Z. Gagnon, S. Senapati, and H. C. Chang, "You have full text access to this content Optimized DNA hybridization detection on nanocolloidal particles by dielectrophoresis," *Electrophoresis*, vol. 31, 666, (2010)

[4.6] S. Basuray, S. Senapati, A. Aijian, A. R. Mahon, and H. C. Chang, "Shear and AC Field Enhanced Carbon Nanotube Impedance Assay for Rapid, Sensitive, and Mismatch-Discriminating DNA Hybridization," *ACS Nano*, vol. 3, 1823, (2009)

[4.7] C. Bustamante, J. F. Marko, E. D. Siggia, and S. Smith, "Entropic elasticity of lambda-phage DNA," *Science*, vol. 265, 1599, (1994)

[4.8] S. B. Smith, L. Finzi, and C. Bustamante, "Direct mechanical measurements of the elasticity of single DNA molecules by using magnetic beads," *Science*, vol. 258,

1122, (1992)

[4.9] T. R. Strick, J. F. Allemand, D. Bensimon, A. Bensimon, and V. Croquette, "The Elasticity of a Single Supercoiled DNA Molecule," *Science*, vol. 271, 1835, (1996)

[4.10] A. Mooradian, "Photoluminescence of Metals," *Phys. Rev. Lett.*, vol. 22, 185, (1969)

[4.11] G. Davies, "Properties and Growth of Diamond," INSPEC, The Institution of Electrical Engineers, London, EMIs Data Review Series, (1994)

[4.12] G. Davies and M. F. Hamer, "Optical Studies of the 1.945 eV Vibronic Band in Diamond," *Proc. R. Soc. Lon. Ser.-A*, vol. 348, 285, (1976)

[4.13] G. Davies, S. C. Lawson, A. T. Collins, A. Mainwood, and S. J. Sharp, "Vacancy-related centers in diamond," *Phys. Rev. B*, vol. 46, 13157, (1992)

[4.14] J. E. Ralph, "Radiation Induced Changes in the Cathodoluminescence Spectra of Natural Diamonds," *Proc. Phys. Soc.*, vol. 76, 688, (1966)

[4.15] G. Davies, "Dynamic Jahn-Teller distortions at trigonal optical centres in diamond," *J. Phys. C*, vol. 12, 2551, (1979)

[4.16] G. Davies and N. B. Manson, *Ind. Diam. Rev.* Feb: 50 (1980).

[4.17] R. A. Dugdale, "The colouring of diamonds by neutron and electron bombardment," *Br. J. Appl. Phys.*, vol. 4, 334, (1953)

[4.18] G. Davies, "The Jahn-Teller effect and vibronic coupling at deep levels in

diamond," Rep. Prog. Phys., vol. 44, 787, (1981)

[4.19] F.L. Zhao, Z. Gong, S.D. Liang, N.S. Xu, S.Z. Deng, J. Chen, and H.Z. Wang,

"Ultrafast optical emission of nanodiamond induced by laser excitation," Appl. Phys.

Lett., vol. 85, 914, (2004)

[4.20] A.E. Aleksenski, V.Yu. Osipov, A.Ya. Vul', B.Ya. Ber, A.B. Smirnov, V.G.

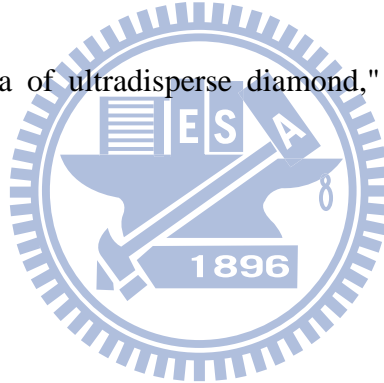
Melekhin, G.J. Adriaenssens, and K. Iakoubovskii, "Optical properties of

nanodiamond layers," Phys. Solid State, vol. 43, 145, (2001)

[4.21] .E. Kompan, E.I. Terukov, S.K. Gordeev, and Fiz. Tverd. Tela

"Photoluminescence spectra of ultradisperse diamond," Phys. Solid State, vol. 39,

1928, (1997).



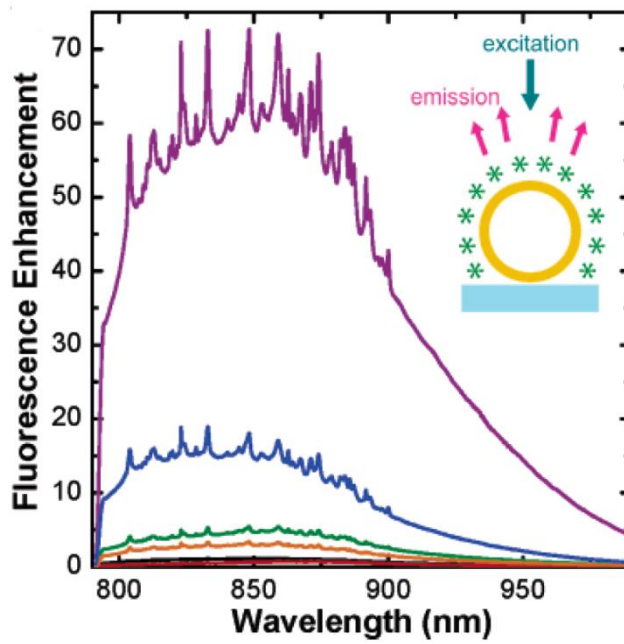


Figure 4-1: ICG dye molecules were enhanced by metallic nanoparticles [4.1]

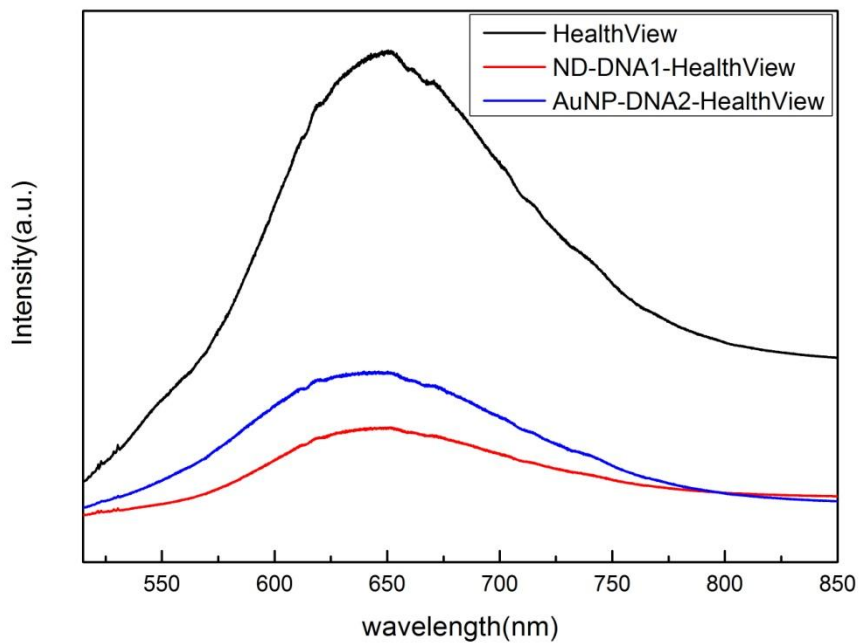


Figure 4-2: Spectra of Healthview Nucleic Acid Stain, and ND-DNA1 and Au-DNA2 solutions were allowed to react with Healthview Nucleic Acid Stain

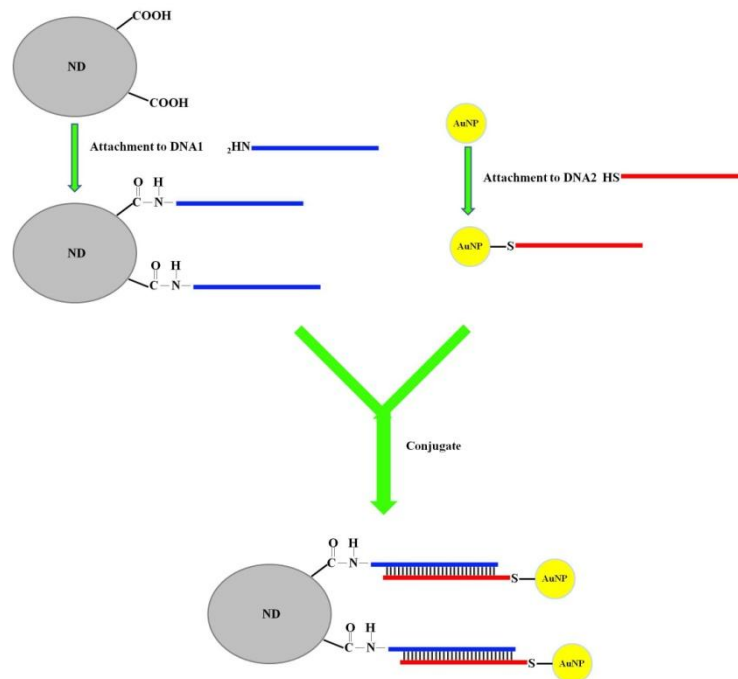


Figure 4-3: Scheme of conjugation gold nanoparticle and nanodiamond by DNA.

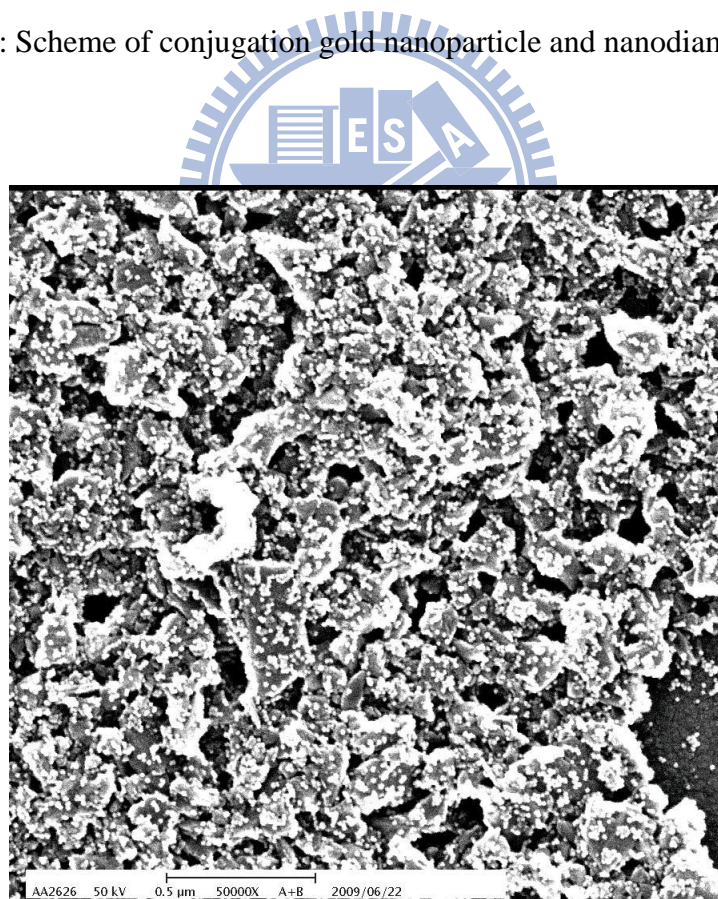


Figure 4-4(a): SEM images of the hybrid structures of NDs coupled with the 13 nm gold nanoparticles,

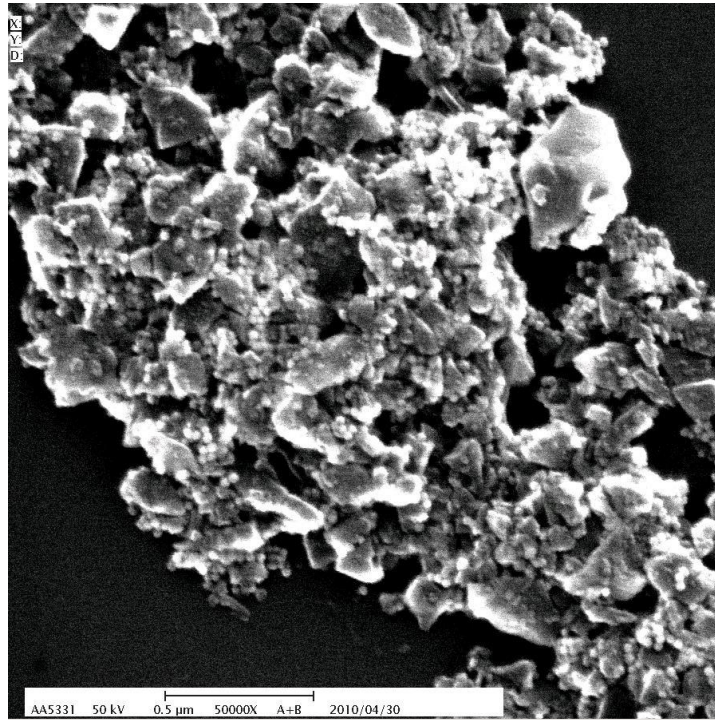


Figure 4-4(b): SEM images of the hybrid structures of NDs coupled with the 30 nm gold nanoparticles,

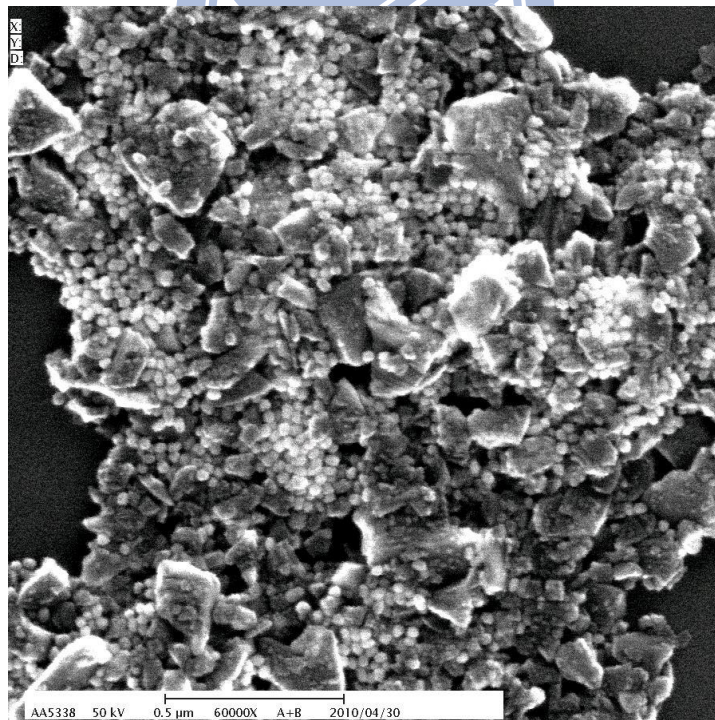


Figure 4-4(c): SEM images of the hybrid structures of NDs coupled with the 50 nm gold nanoparticles,

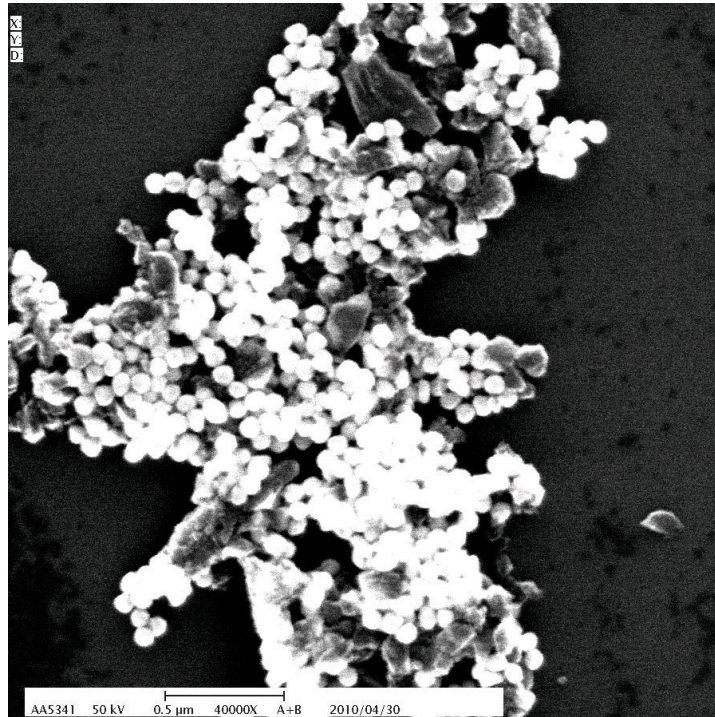


Figure 4-4(d): SEM images of the hybrid structures of NDs coupled with the 80 nm gold nanoparticles,

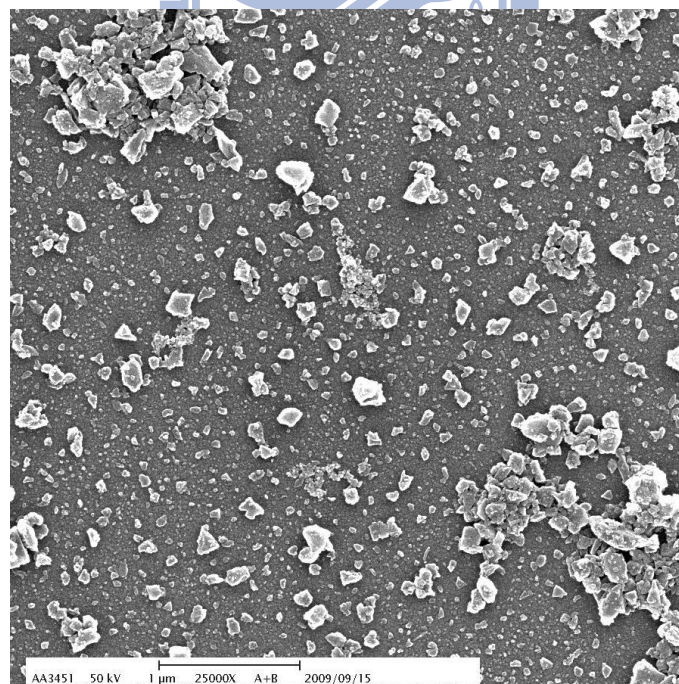


Figure 4-5: SEM image of NDs interacted with gold nanoparticles without DNA

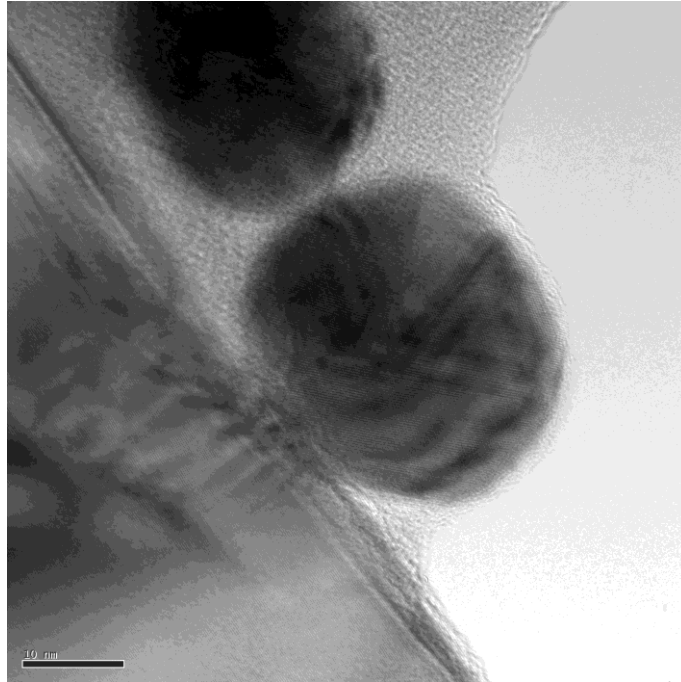


Figure 4-6: HRTEM image of a 30 nm gold nanoparticle attached on a ND via a double string DNA

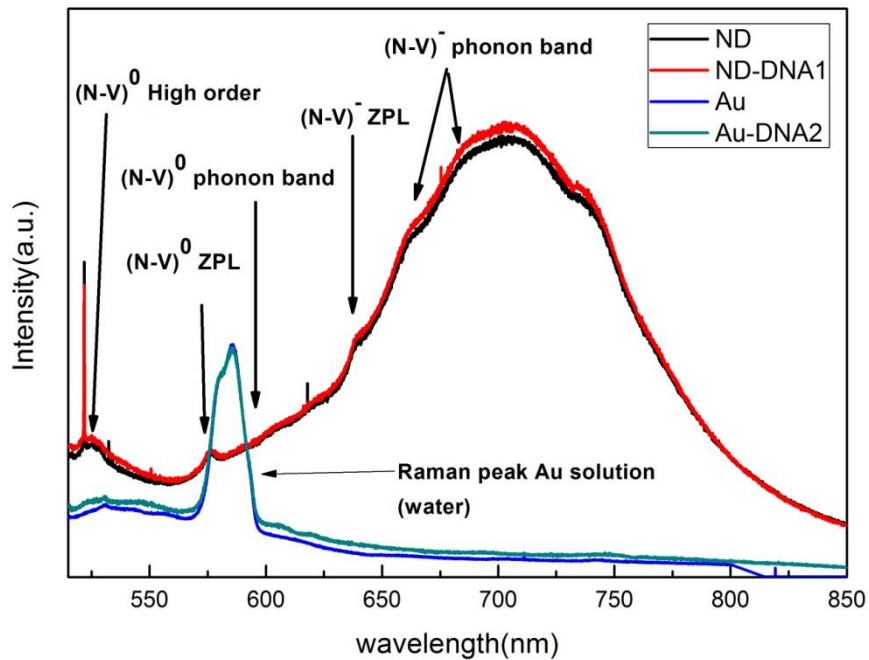


Figure 4-7(a): PL spectra of bare ND, gold nanoparticles, Au-DNA2 assembly, and ND-DNA1 assembly

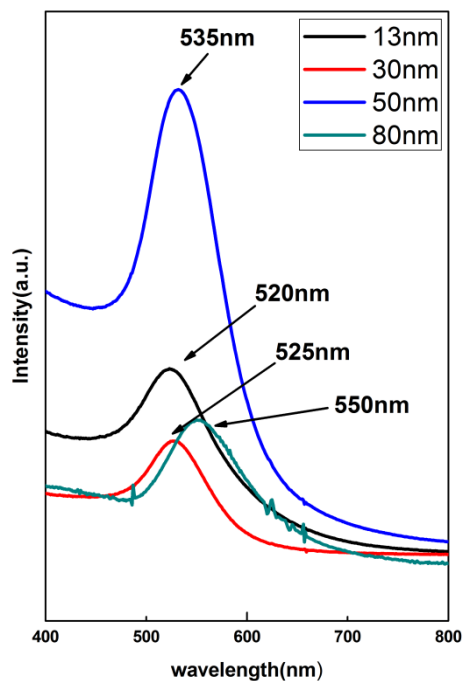


Figure 4-7(b): Absorption spectra of 13nm, 30nm, 50nm, and 80nm Au

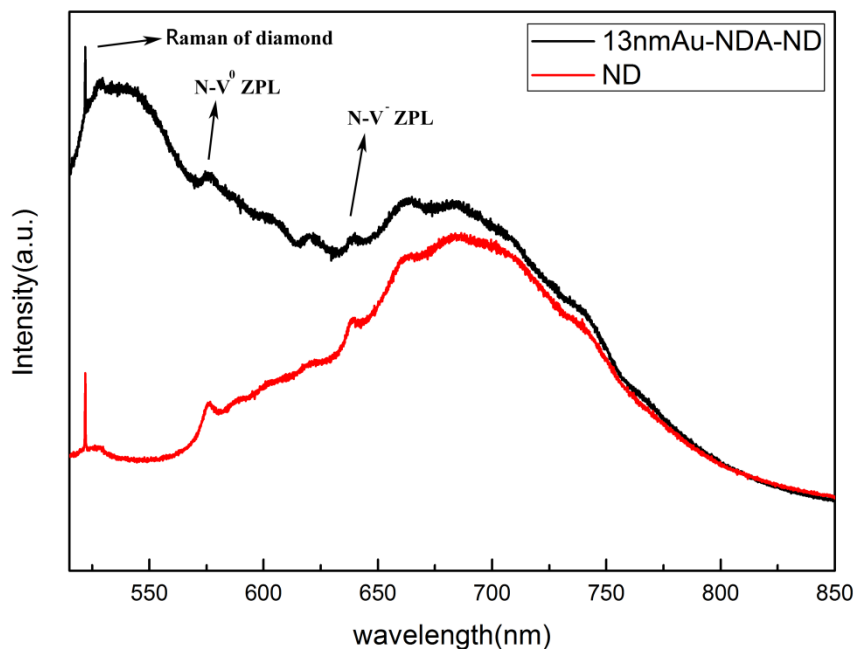
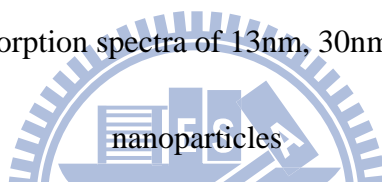


Figure 4-8(a): Plasmon enhanced PL spectra of Au-DNA-ND hybrid structures with gold nanoparticle sizes of 13 nm

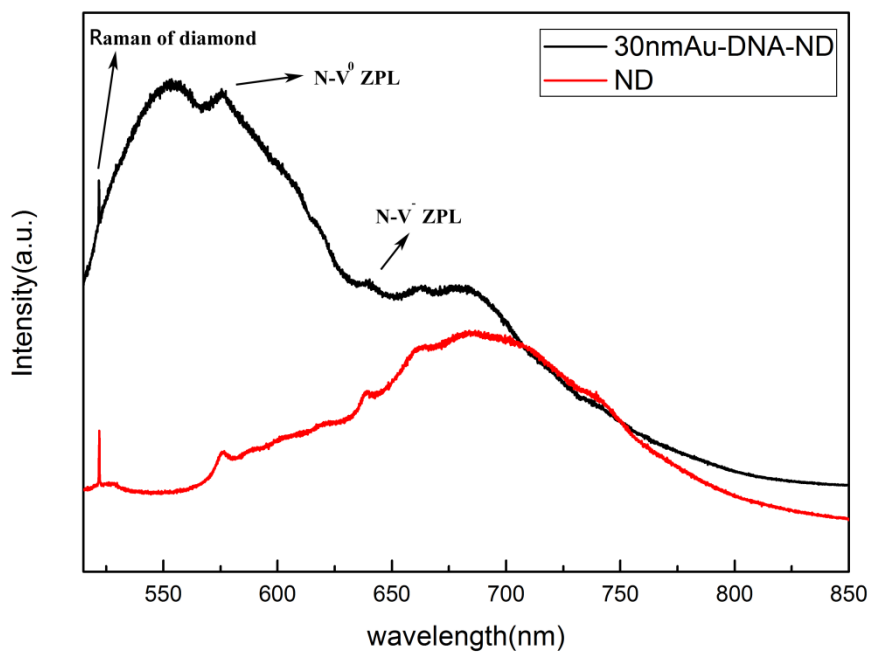


Figure 4-8(b): Plasmon enhanced PL spectra of Au-DNA-ND hybrid structures with gold nanoparticle sizes of 30 nm

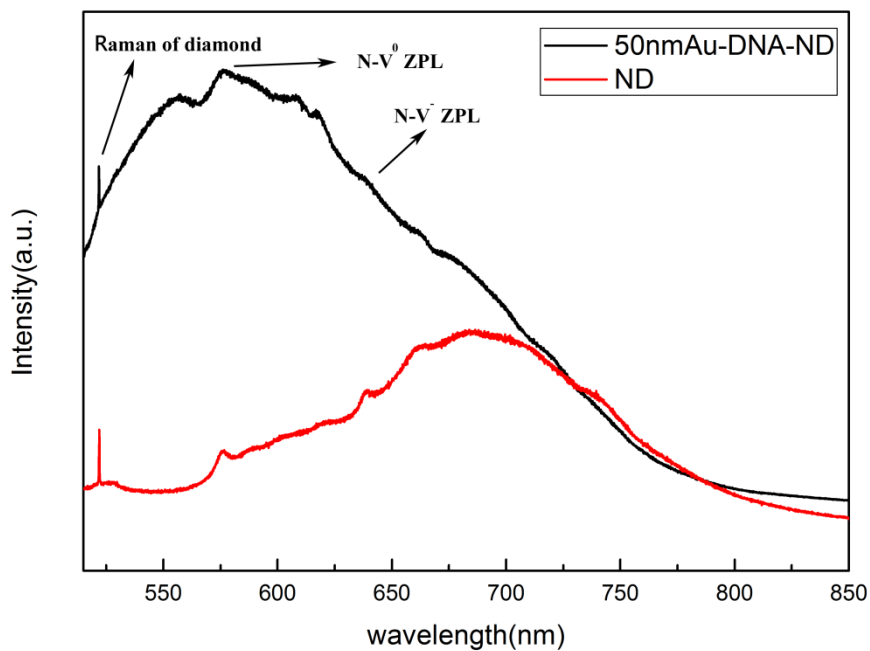


Figure 4-8(c): Plasmon enhanced PL spectra of Au-DNA-ND hybrid structures with gold nanoparticle sizes of 50 nm

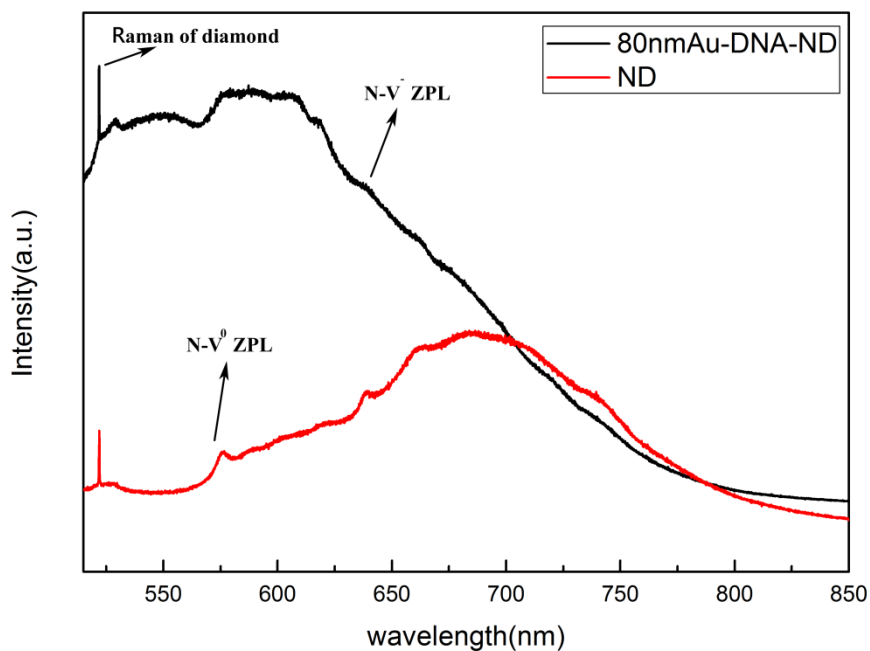


Figure 4-8(d): Plasmon enhanced PL spectra of Au-DNA-ND hybrid structures

with gold nanoparticle sizes of 80 nm

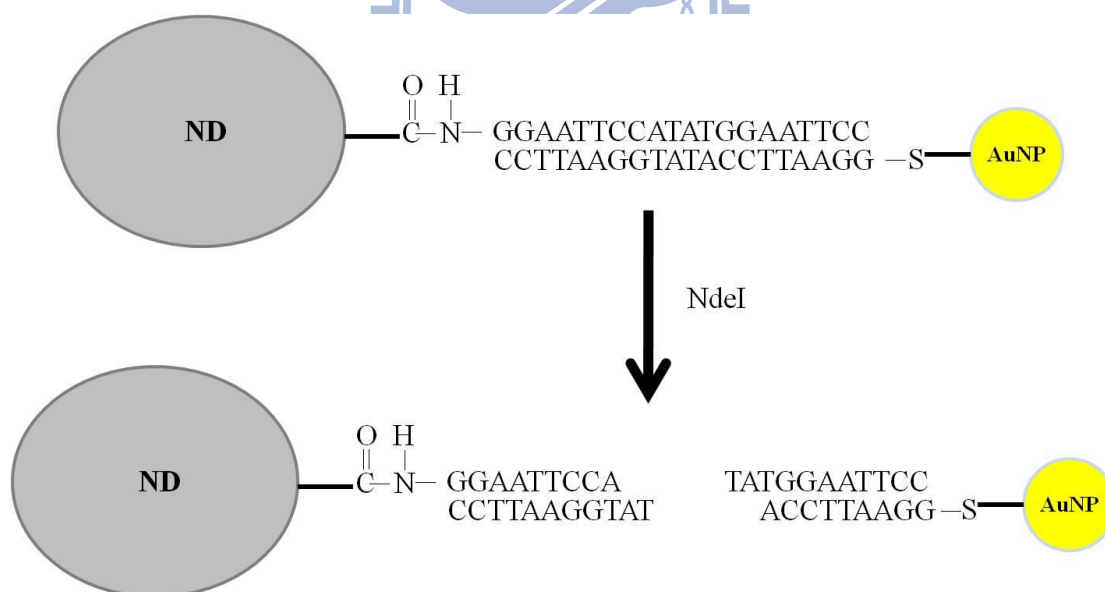


Figure 4-9: Scheme of interaction between hybrid structures and NdeI restriction

enzyme

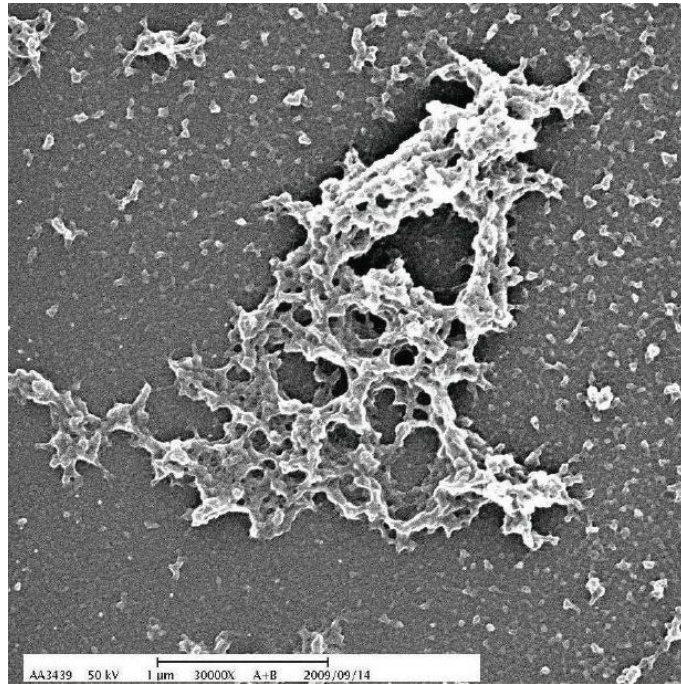


Figure 4-10: SEM image of hybrid structures interact with the NdeI restriction

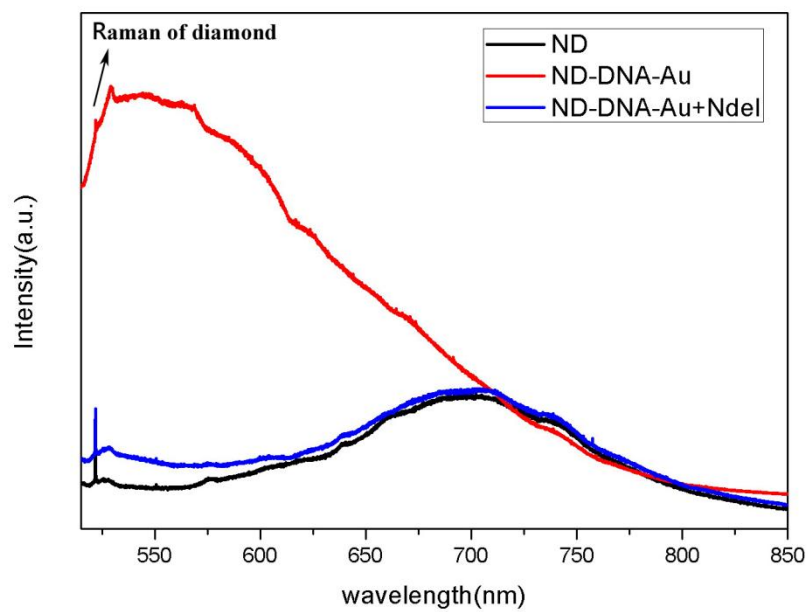
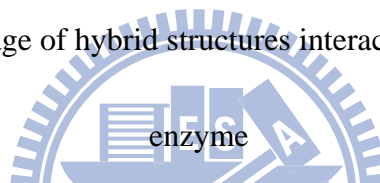


Figure 4-11: PL spectra of bare ND, Au-DNA-ND hybrid structures before and after interacting with NdeI restriction enzyme

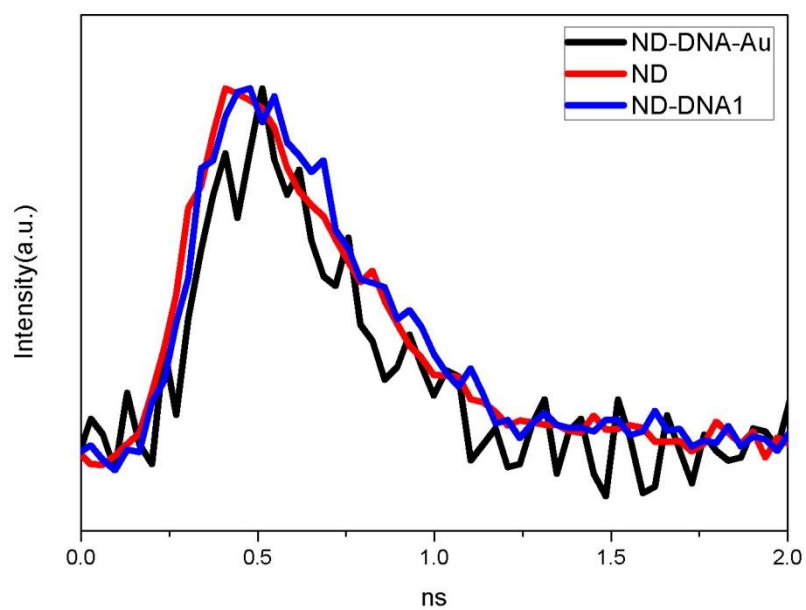
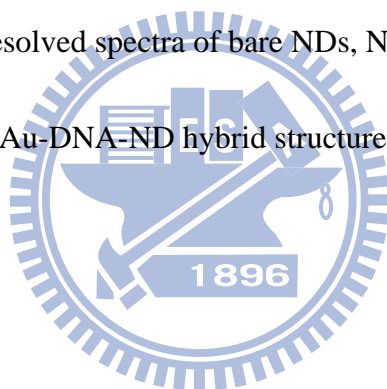


Figure 4-12: Time-resolved spectra of bare NDs, ND-DNA1 assembly, and

Au-DNA-ND hybrid structures



Chapter 5 Conclusion

In the first part of the thesis, we demonstrated novel methods and techniques to pattern and anchor bio-functionalized nanodiamond arrays. The nanodiamond arrays can be functionalized by different kinds of bio-molecules, such as PLL and lysozyme proteins. The device demonstrated here is suitable for applications in bio-sensing chips and single bio-molecule patterning and detection. It facilitates the development of new applications of different bio-functionalized nanodiamond arrays that can interact with special targets, as well as the individual observation of their optical property.

In the second part, we use the DNA as the linker to combine the nanodiamond with various sizes of gold nanoparticles. The PL profile was modified in different ways when the gold nanoparticles with different Plasmon resonances (or various sizes) were bound to the NDs via the DNA linkers. The NdeI restriction enzyme can detach the gold nanoparticles from the nanodiamond to deactivate the enhancement from the gold nanoparticles. This approach can also be extended to other color center and metal nanoparticles, thereby providing a method for bio chip and bio-molecular detection.

Publications

Protein Functionalize Nanodiamond Arrays

Y. L. Liu and K. W. Sun

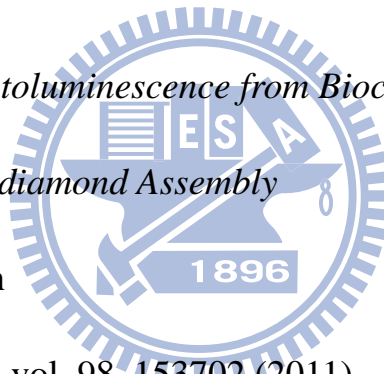
Nanoscale Res Lett vol. 5, 1045 (2010)

Plasmon-enhanced Photoluminescence from Bioconjugated Gold

Nanoparticle and Nanodiamond Assembly

Y. L. Liu and K. W. Sun

Applied Physics Letters vol. 98, 153702 (2011)



Appendix-Fluorescent defect centers in nitrogen-doped

ultrananocrystalline diamond films generated by microwave plasma

A-1 Literature review

A-1-1 Ultrananocrystalline diamond films

Diamonds have enormous potential applications due to their marvelous physical and chemical properties. Diamond films grown by chemical vapor deposition (CVD) method from CH_4/H_2 mixtures typically have micrometer-size crystallites [A.1]. In contrast, diamond films grown from hydrogen-poor Ar/CH_4 microwave plasmas are characterized by microstructures consisting of crystallites with an average size 3-10 nm [A.2]. The latter films are called ultrananocrystalline diamond (UNCD). Use of hydrogen-poor growth conditions systematically produces uniform films with controlled grain size in the range of a few nanometers and with thicknesses up to several tens of micrometers. These UNCD films have a large percentage of atoms at the grain boundaries [A.2] which are expected to be different from those in microcrystalline diamond. The UNCD films have attracted much attention as a promising material due to unique and advantageous properties such as high hardness, chemical inertness, high electron field emitting [A.3, A.4], and possibility of p- and

n-type conductivities by doping [A.5]. Moreover, many physical properties, such as electrical conductivity [A.6], field emission threshold voltage [A.4], mechanical [A.7], and optical properties [A.8], differ from other conventional diamond films. Many properties of UNCD show dependence on the crystalline size, fraction of carbon atoms, and the concentration of impurities, which open scientific and technological applications such as optics, microelectronics systems, and tribology [A.9, A.10].

A-1-2 Semiconductor diamond

The CVD diamond film is possible to be fabricated with a p-type or n-type conducting nature. However, there is a typical problem in doping of wide band gap semiconductors, i.e., p-type doping is easier than n-type doping in diamond [A.11]. Diamond can be efficiently doped into p-type with boron [A.12]. Boron occurs in the rare type IIb natural diamond, and can be readily incorporated in synthetic diamond, both via CVD and HPHT methods. Acceptor concentrations over a wide range can be achieved, with the characteristics of the films varying from relatively resistive p-type samples to highly conductive material, which exhibits metallic conduction [A.13, A.14]. In contrast, an effective n-type doping in diamond has not yet been established. From early 1980s, n-type doping has been investigated mainly using phosphorus as an impurity. In 1996, the phosphorus-doped n-type diamond thin films on diamond substrates are grown and the nature of the conductivity is clearly characterized by

temperature dependent Hall measurements [A.15]. From an analogy to phosphorus, nitrogen seems to be impurities doped in n-type diamond films intuitively. Bhattacharyya and his coworkers have shown nitrogen-doped UNCD samples synthesized by a microwave plasma-enhanced chemical-vapor-deposition method using a CH_4 (1%) / Ar gas mixture with 1%–20% nitrogen gas added during the growth [A.6]. The electrical conductivity of the nitrogen-doped UNCD films was found to increase with increasing nitrogen content. Figure A-1 shows the results of the conductivity measurements obtained in the temperature range of 300 K to 4.2 K for films contained different nitrogen concentrations.

A-1-3 Ion implantation

Implantation of impurities for controlled doping of semiconductors is a routine technique nowadays. It is a material engineering process which is described as a operation of utilizing the ions of any materials to be accelerated in an electrical field and then impacted into another solid. It can also be used to introduce the impurities into any kind of materials and modifies its properties, regardless of the considerations of the phase diagram and thermodynamic equilibrium. However, the ion implantation is always accompanied severe damage to the target while the energy of ion implantation exceeds in bind energy of the solid.

One common technique to create defect centers in diamond is through ion

implantation and high temperature annealing. Ion implantation is used to create damage in diamond lattice and generate vacancies in diamond, which can also be used to introduce impurities. It is the only technique to effectively modify diamond after its growth and is widely used to realize p-type and n-type doping of diamond [A.16].

A lot of damages are induced by ion implantation, which can lead to changes in the bonding configuration resulting in drastic changes in physical and chemical properties. The damage threshold was found to be 10^{22} vacancies/cm³ for room temperature implantations [A.17]. The two elementary damage products - vacancies and interstitials - have different diffusivities [A.18]. Carbon interstitials seem to become mobile in diamond at about 50 K, while vacancies probably start to diffuse only at about 700 K. This leads to an imbalance between interstitials and vacancies in the vacancy-rich region. In order to achieve the optimal annealing of the crystal, extra carbon atoms may be supplied to the vacancy-rich region.

Generally, annealing of diamond is carried out in vacuum or under protective gas to avoid the reaction with oxygen. Annealing is performed at temperature which vacancies become mobile and combine with impurities to form defect centers [A.19, A.20]. Ion implantation has also been shown as a unique method of controllable creation of single optical centers.

Collins and his coworkers confirm that the 737nm center involves silicon by

implanting conventional diamond with Si ions [A.21]. Figure A-2 demonstrated that silicon vacancies (1.681eV) were generated by ion implantation. Meijer and his coworkers have shown that nitrogen-vacancy (N-V) defect centers were also produced in very pure diamond (type IIa) by nitrogen implantation as reported in [A.20]. The N-V defect centers also have been produced in nitrogen-rich diamond (type Ib) by high-energy radiation damage such as focus ion beam (FIB) or electron beam, followed by an annealing process [A.22]. The annealing is carried out at a temperature so that vacancies become mobile and can combine with the impurities to form defect centers. Another common technique to create defect centers in diamond is through ion implantation. Figure A-3 demonstrated that the neutral vacancy was formed after nitrogen ion implantation. After annealing, the neutral vacancy was converted into N-V centers.

A-1-4 Silicon vacancies

It is a fact that the strong narrow-line luminescence at emission energy of 738nm (1.681 eV) and 757nm (1.638 eV) is assigned as silicon vacancy center (Si-V) [A.21]. The most striking property of Si-V center is that which exhibits a very weak vibronic structure, both in luminescence and absorption, with no mirror symmetry relative to the ZPL. The majority of the emission is concentrated on the ZPL with a FWHM of about 6 nm, even though it is at room temperature. The short luminescence lifetime is,

moreover, another extraordinary property of the Si-V center. It was measured to be 2.7ns at room temperature and 4ns at 4K [A.23]. The charge state of Si-V center is predominantly considered to be neutral, since Si-V center shows a similar property in the measurement as the neutral N-V center. The UV illumination which can increase the intensity of the ZPL of Si-V up to ten times indicates that the existence of a more positively charged state. However, the luminescence of Si-V is usually undetectable in natural semiconducting diamond with negligible nitrogen atoms content [A.21]. The isolated nitrogen atoms act as electron donors in diamond, and then pin the Fermi-level to a position of nearing the conduction band. The Si-V is a more positively charged state that is also optically inactive. Its center becomes smaller with the higher position of Fermi-level, and the emission of the Si-V center, consequently, increases.

A-2 Growth of nitrogen-doped UNCD films

Nitrogen doped ultrananocrystalline diamond (N-doped UNCD) films were grown on SiO₂/Si substrates in microwave plasma enhanced chemical vapor deposition (MPECVD) system (IPLAS Cyrranus) with microwave power of 1400W at a pressure of 110 Torr and a substrate temperature of 800°C for 45 minutes. The Ar-rich mixture gases (73% Ar / 25% N₂ / 2% CH₄) were used as reaction gases during the growth.

Before the deposition, the substrate surface was seeded in an ultrasonic bath with nanodiamond particles from detonation synthesis (with an average size of 4-6 nm)

A-3 Properties of nitrogen-doped UNCD films

Figure A-4 shows the high resolution transmission electron microscopy (HRTEM) image of the nitrogen-doped UNCD film. The crystalline diamond grain of nitrogen-doped UNCD shows pin-like structures and is wrapped by a SP^2 graphite structure. For low-nitrogen partial pressure the morphology of the films remains largely unchanged, with the grain size and grain boundary (GB) widths increasing only slightly. However, in films made with higher N_2 partial pressure, both the grain size and GB widths increase significantly [A.24-A.26]. It is the main mechanism for the increase in grain size and grain boundary width in nitrogen doped UNCD. The clustering of larger grains leads to the elongation of the nanocrystalline structures and results to the formation of pin-like structures in nitrogen-doped UNCD films.

The room temperature conductivity was about $140 \Omega^{-1}cm^{-1}$ for 25% N-doped UNCD film. In previous reports [A.6, A.25, A26], the tight binding molecular dynamics simulations indicate that the nitrogen is favored to be incorporated into the grain boundaries than into the grains. When nitrogen is introduced into the GBs, the associated carbon dangling-bond state is above the Fermi level and donates electron-to-carbon defect states near the Fermi level, causing it to shift upward, i.e.,

toward the conduction band. Thus, it is reasonable to believe that nearest-neighbor hopping or other thermally activated conduction mechanisms would occur in the GBs and result in greatly enhanced electron transport [A.6, A.27, A.28].

The Raman spectra for the undoped UNCD films and the nitrogen-doped UNCD films are shown in Figure A-5. The spectrum of the undoped UNCD film consists of five peaks, which indicates the following three carbon phases: 1. diamond (peak at 1332cm^{-1}); 2. amorphous SP^2 carbon (D-band at 1350cm^{-1} and G-band at 1580cm^{-1}); and 3. polyacetylene (1150cm^{-1} is C-H in-plane bending and 1480cm^{-1} is C=C stretch vibrational modes of trans-polyacetylene) [A.29]. The increase of the SP^2 structure (D-band and G-band) in grain boundaries is also confirmed in the Raman spectrum from nitrogen-doped UNCD films. The peak at 1150cm^{-1} , which is a typical feature in the undoped UNCD film, disappears for the nitrogen-doped UNCD film due to the increase of grain size and grain boundaries.

Although the theoretical calculations and experiments in previous studies indicate that nitrogen is favored to be incorporated into the grain boundaries. However, it is still possible for some of the nitrogen dopants to enter the grains, and even form the N-V complexes [A.26, A.30, A.31]. Figure A-6 shows the energy dispersive spectrum (EDS) data with the electron beam aimed at the grain boundaries (as shown in Figure A-6(a)) and grains (as shown in Figure A-6(b)). The EDS spectra indicate that the

nitrogen appears both in the grain boundaries and inside the grains. Therefore, it proves that the nitrogen can be incorporated both in the grain boundaries and the grains.

A-4 Properties of nitrogen-doped UNCD films treated with microwave plasma

After the growth, the nitrogen-doped UNCD film was treated with microwave plasma at room temperature for 30 minutes with various power ranged from 300 W to 800 W and total pressure varied from 0.1 Torr to 10 Torr. The simulated air (80% N₂ / 20% O₂) was used as reaction gas in microwave plasma treatment.

Figure A-7 show the HRTEM images of nitrogen-doped UNCD films after microwave plasma treatment at room temperature with 800W power and total pressure of 10 Torr for 30 minutes. Images in Figure A-7 demonstrate that the crystallinity of the nitrogen-doped UNCD film is not affected by the microwave plasma treatment and retains its grain boundaries and grains morphology. There is no indication of re-growth in the nitrogen-doped UNCD film after microwave plasma treatment.

The Raman spectra were recorded for nitrogen-doped UNCD film before (as shown in Figure A-8(a)) and after the microwave plasma treatment (as shown in Figure A-8(b) and (c)). Figure A-8 (b) and (c) show the Raman spectra of nitrogen-doped

UNCD film treated with different microwave plasma power and at a total pressure of 10 Torr. After the microwave plasma treatment, we find that the Raman peaks of SP² carbon phases (D-band and G-band) are decreased and the Raman peak of 1332cm⁻¹ (corresponding SP³ structure diamond) is revealed. This is attributed to the oxygen in the microwave plasma reaction gases which induces the oxidation of the SP² carbon cluster and leads to the reduction in the SP² carbon clusters. When this reaction takes place, the peak of SP³ can be clearly revealed. Most SP² carbon exists in the grain boundaries. Because the reduction of SP² carbon clusters also leads to the reducing of the grain boundaries. Therefore, both the Raman signals of amorphous carbon and diamond disappear under very high microwave power and total pressure, as shown in Figure A-8(c). Under high power and total pressure, it not only leads to over etching of the amorphous carbon but also the etching of the diamond.

Two different samples (sample A and sample B) were grown in this work. The EDS spectra of sample A and sample B (shown in figure A-9(a) and (b)) indicate that the sample B contains silicon impurities but sample A does not (or too low to be detectable). The same results are also established by SIMS (secondary ion mass spectrometry) spectra. The figure A-10(a) and (b) are SIMS spectra of sample A and sample B, respectively. The intensity of silicon in sample A is much weaker than other elements. However, the intensity of silicon in sample B is 100 times higher than

sample A. This is because that the sample B was intentionally placed closer to the atomic gas of plasma than the sample A during the growth. Therefore, etching of the silicon substrate may occur which introduced the silicon impurities into the UNCD films during the growth proceeding [A.32].

The PL spectra measured in the wavelength range of 515-850 nm for sample A and sample B are shown in Figure A-11. For the untreated nitrogen-doped UNCD films, the measured PL intensity of both samples is rather weak. The two peaks in 522nm and 528nm are the Raman peaks of D-band and G-band. After microwave plasma treatment, both sample A and sample B show strong PL enhancement between 550nm and 650nm. The PL spectrum of sample A shows two major peaks around 575nm and 630nm. By using band assignment from previous PL spectra reports, the signals between 550nm and 750nm were contributed form nitrogen vacancies $[(N-V)^0]$ and $[(N-V)^-]$ [A.33-A.35].

In sample A the PL intensity of nitrogen vacancies $[(N-V)^0]$ is stronger than that of $[(N-V)^-]$. The remarkable point of the $[(N-V)^0]$ center is the absorption to be very weak, especially in the case of highly nitrogen contained type-Ib diamond [A.36]. The electron donors provide an efficient conversion of N-V into negative charged state. But, the graphitic related defects are possible electron trapper which can ionize the electron donors [A.37, A.38]. The Raman spectrum, which shows strong intensity of

SP² graphite demonstrates that there are much graphitic related defects in nitrogen-doped UNCD films. Although the microwave plasma treatment reduces the graphitic defects, there was still much graphite in nitrogen-doped UNCD films. Other than the graphite, the diamond grain size also effect the charge state of N-V center. In previous report [A.39], the ratio between [(N-V)⁻] and [(N-V)⁰] decreases with the reduction of the diamond size. That can explain our observation of higher intensity of the [(N-V)⁰] than that of [(N-V)⁻] in the PL results.

The PL results of sample B were slightly different from sample A. Other than the broad emission band between 550nm and 750nm, there were also two narrow peaks at 738nm and 757nm appeared in the PL spectrum. By comparing with earlier PL spectra reported in diamond, the peaks are originated from Si vacancy centers (Si-V) [A.21, A.40]. Si-V, whose zero phonon emissions appear at wavelength of 738nm and 757nm, is another constant color center in diamond. Both Si-V and N-V defects are composed by a single atom of an impurity and a vacancy located in a neighboring site of the diamond lattice. However, Si-V center shows numbers of advantage in optical properties over the N-V center. Si-V center, which is the very weak vibronic sideband of the Si-V defect at room temperature, provides narrow-band emission, as opposed to the board band emission from N-V center which is strong and board vibronic sideband.

It has been reported that the PL of Si-V was much stronger in synthetic diamonds with high concentration of nitrogen, but not in the nitrogen free diamond [A.21]. The isolated nitrogen atom act as donors in diamond and pin the Fermi-level to position near to conduction band. The Si-V is more positively charged state which is not optically active. The Si-V in optical inactive charged state has been reduced with higher position of the Fermi-level. So, the photoluminescence of Si-V can't be detected in semiconducting diamond with negligible nitrogen content [A.21]. According to the EDS spectra, sample B contains the Si impurities, however, sample A does not. We conclude that the different impurities in nitrogen-doped sample B lead to the generation of different vacancy centers after microwave plasma treatment.

In the previous research [A.19, A.20], the neutral vacancies can be generated by high energy irradiation such as focused ion-beam or electron beam. The vacancies can become mobile if annealed at 700°C. Some of these vacancies are subsequently trapped by substitutional nitrogen or silicon impurities and form stable N-V or Si-V centers. In our case, the microwave plasma generates the vacancies due to slightly etching of the diamond. Moreover, the ion gases in the plasma provide the heat and further mobilize the vacancies to combine with the impurities, which leads to the formation of the N-V or Si-V.

The conductivity of nitrogen-doped UNCD film treated with microwave plasma is

slightly decreased (about 0.1 to $1\Omega^{-1}\text{cm}^{-1}$). The Raman data indicate that the SP^2 carbon reduce after microwave plasma treatment. It means the grain boundaries may also reduce after microwave plasma treatment. The conductivity also decreases due to reduce to the grain boundaries. However, the Fermi level (E_f) which is pinned by the gap states produce from the vacancy related centers is closer to the conduction band E_c . The vacancy related defects play the role of donor centers that are responsible for n-type conductivity of UNCD films. It may explain that the conductivity was only slightly decreased after plasma treatment.

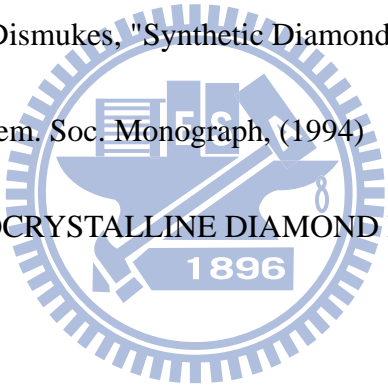
The distribution of generated fluorescent defect centers in the samples was checked by micro-PL mapping technology. The nitrogen-doped UNCD located at different depth in the film was exposed simultaneously by subsequently bombarding the film with different depths and along a fixed direction using a focus ion beam. Scanning electron microscopy (SEM) image of the openings at different depths is shown in Figure A-12(a). One dimension PL mapping is carried out along the red line indicated in Figure A-12(a). The PL intensity mapping was completed along a scanning distance of 7 μm with a step of 300nm. PL intensity of the Si-V related peak and N-V related peak as a function of the scanning distance are plotted in Figure A-12(b) Figure A-12(c). The PL mapping results proves that the plasma generated Si-V and N-V are uniformly distributed in the nitrogen-doped UNCD film.

A-5 Summary

In summary, nitrogen-doped UNCD thin films have been synthesized using microwave plasma CVD with CH₄/Ar gases mixture and 25% N₂ added. When nitrogen is introduced into the GBs, the associated carbon dangling-bond state is above the Fermi level and donates electron-to-carbon defect states near the Fermi level. The nearest-neighbor hopping or other thermally activated conduction mechanisms could occur in the GBs and result in greatly enhanced electron transport. Although the theoretical calculations and experiments in previous studies indicate that nitrogen is favored to be incorporated into the GB. The EDS spectra indicate that the nitrogen appears in both grain boundaries and grains. The optical properties and conductivity of the nitrogen-doped UNCD films are affected by the microwave plasma treatment. The low energy microwave plasma generates fluorescence defect centers in the N-doped UNCD films. The different types of impurities in the nitrogen-doped UNCD films lead to the generation of different color centers after microwave plasma treatment. In our case, the microwave plasma generates the vacancies due to slightly etching of the diamond. The ion gases in the plasma provide the heat and further mobilize the vacancies to combine with the impurities, which leads to the formation of the N-V or Si-V. The nitrogen incorporation into grains was also proved by the

generation of N-V and Si-V in diamond. The conductivity of the UNCD film also decreases due to the reduced grain boundaries. The PL mapping results shows that the plasma generated Si-V and N-V are uniformly distributed in the nitrogen-doped UNCD film. Fabrication of diamond light-emitting source can be further developed using electrically active color centers in the future.

A-6 Reference

- 
- [A.1] K. E. Spear and J. P. Dismukes, "Synthetic Diamond: Emerging CVD Science and Technology," Electrochem. Soc. Monograph, (1994)
- [A.2] D. M. Gruen, "NANOCRYSTALLINE DIAMOND FILMS." Annu. Rev. Mater. Sci., vol. 29, 211, (1999)
- [A.3] D. Zhou, A. R. Krauss, L. C. Qin, T. G. McCauley, D. M. Gruen, T. D. Corrigan, R. P. H. Chang, and H. Gnaser, "Synthesis and electron field emission of nanocrystalline diamond thin films grown from N₂/CH₄ microwave plasmas," J. Appl. Phys., vol. 82, 4546, (1997)
- [A.4] A. R. Krauss, O. Auciello, M. Q. Ding, D. M. Gruen, Y. Huang, V. V. Zhirnov, E. I. Givargizov, A. Breskin, R. Chechen, E. Shefer, V. Konov, S. Pimenov, A. Karabutov, A. Rakhimov, and N. Suetin "Electron field emission for ultrananocrystalline diamond films," J. Appl. Phys., vol. 89, 2958, (2001)

[A.5] O.A. Williams, S. Curat, J.E. Gerbi, D.M. Gruen, and R.B. Jackman, "n-type conductivity in ultrananocrystalline diamond films." *Appl. Phys. Lett.*, vol. 85, 1680, (2004)

[A.6] S. Bhattacharyya, O. Auciello, J. Birrell, J. A. Carlisle, L. A. Curtiss, A. N. Goyette, D. M. Gruen, A. R. Krauss, J. Schlueter, A. Sumant, and P. Zapol, "Synthesis and characterization of highly-conducting nitrogen-doped ultrananocrystalline diamond films," *Appl. Phys. Lett.*, Vol. 79, 1441, (2001)

[A.7] C. Zuiker, A. R. Krauss, D. M. Gruen, X. Pan, J. C. Li, R. Csencsits, A. Erdemir, C. Bindal, and G. Fenske, "Physical and tribological properties of diamond films grown in argoncarbon plasmas," *Thin Solid Films*, vol. 270, 154, (1995)

[A.8] T. Sharda, M.M. Rahaman, Y. Nukaya, T. Soga, T. Jimbo, and M. Umeno, "Structural and optical properties of diamond and nano-diamond films grown by microwave plasma chemical vapor deposition," *Diamond Relat. Mater.*, vol. 10, 561, (2001)

[A.9] Huang, B.R., Wu, T.H., Jou, S., Chen, W.R., Hsu, J.F. and Yeh, C.S., "Effect of triode structure on field emission properties of nanocrystalline diamond films," *Diamond Relat. Mater.*, vol. 18, 235, (2009)

[A.10] S. Pezzagna, D. Rogalla, D. Wildanger, J. Meijer, and A. Zaitsev, "Creation and nature of optical centres in diamond for single-photon emission—overview and

critical remarks," *New J. Phys.*, vol. 13, 035024, (2011)

[A.11] D. B. Laks, C. G. Van de Walle, G. F. Neumark, and S. T. Pantelides "Role of native defects in wide-band-gap semiconductors," *Phys. Rev. Lett.*, vol. 66, 648, (1991)

[A.12] S. Yamanaka, H. Watanabe, S. Masai, D. Takeuchi, H. Okushi and K. Kajimura "High-Quality B-Doped Homoepitaxial Diamond Films using Trimethylboron," *Jpn. J. Appl. Phys.*, vol. 37, L1129, (1998)

[A.13] T. Tshepe, C. Kasl, J. F. Prins, and M. J. R. Hoch, "Metal-insulator transition in boron-ion-implanted diamond," *Phys. Rev. B*, vol. 70, 245107, (2004)

[A.14] J. Wu, T. Tshepe, J. E. Butler, and M. J. R. Hoch, " $1/f$ noise in semiconducting and just-metallic boron-implanted diamond," *Phys. Rev. B*, vol. 71, 113108, (2005)

[A.15] S. Koizumi, M. Kamo, Y. Sato, H. Ozaki, and T. Inuzuka. "Growth and characterization of phosphorous doped {111} homoepitaxial diamond thin films." *Appl. Phys. Lett.*, vol. 71, 1065, (1997)

[A.16] J. F. Prins, "Ion implantation of diamond for electronic applications," *Semicond. Sci. Technol.*, vol. 18, S27, (2003)

[A.17] C. Uzan-Saguy, C. Cytermann, R. Brener, V. Richter, M. Shaanan, and R. Kalish, "Damage threshold for ion-beam induced graphitization of diamond," *Appl.*

Phys. Lett., vol. 67, 1194, (1995)

[A.18] R. Kalish, "Ion implantation in diamond; damage, annealing and doping," in The Physics of Diamond (A. Paoletti and A. Tucciarone, eds.), pp. 373–409, IOS Press, Amsterdam, (1997)

[A.19] J. Martin, R. Wannemacher, J. Teichert, L. Bischoff, B. Kohler, "Generation and detection of fluorescent color centers in diamond with submicron resolution," Appl. Phys. Lett., vol. 75, 3096, (1999)

[A.20] J. Meujer, B. Buchard, "Generation of single color centers by focused nitrogen implantation," Appl. Phys. Lett., vol. 87, 261909, (2005)

[A.21] A. T. Collins, M. Kamo, and Y. Sato, "A spectroscopic study of optical centers in diamond grown by microwave-assisted chemical vapor deposition," J. Mater. Res., vol. 5, pp. 2507, (1990)

[A.22] J. Martin, R. Wannemacher, J. Teichert, L. Bischoff and B. Kohler, "Generation and detection of fluorescent color centers in diamond with submicron resolution" Appl. Phys. Lett., Vol. 75, 3096, (1999)

[A.23] H. Sternschult, K. Thonke, R. Sauer, P. C. Munzinger, and P. Michler, "1.681-eV luminescence center in chemical-vapor-deposited homoepitaxial diamond films," Phys. Rev. B, vol. 50, 14554, (1994)

[A.24] Dieter M. Gruen, Paul C. Redfern, David A. Horner, Peter Zapol, and Larry A.

- Curtiss "Theoretical Studies on Nanocrystalline Diamond: Nucleation by Dicarbon and Electronic Structure of Planar Defects," J. Phys. Chem. B, vol. 103, 5459, (1999)
- [A.25] Peter Zapol, Michael Sternberg, Larry A. Curtiss, Thomas Frauenheim, Dieter and M. Gruen "Tight-binding molecular-dynamics simulation of impurities in ultrananocrystalline diamond grain boundaries," Phys. Rev. B, vol. 65, 045403, (2002)
- [A.26] James Birrell, J. A. Carlisle, O. Auciello, D. M. Gruen, and J. M. Gibson, "Morphology and electronic structure in nitrogen-doped ultrananocrystalline diamond," Appl. Phys. Lett., Vol. 81, 2235, (2002)
- [A.27] Somnath Bhattacharyya "Mechanism of high n-type conduction in nitrogen-doped nanocrystalline diamond," Phys. Rev. B, vol.70, 125412, (2004)
- [A.28] Kunjal V. Shah, Dmitry Churochkin, Zivayi Chiguvare, and Somnath Bhattacharyya "Anisotropic weakly localized transport in nitrogen-doped ultrananocrystalline diamond films," Phys. Rev. B, vol.82, 184206, (2010)
- [A.29] I. I. Vlasiv, V. G. Ralchenko, E. Goovaerts, A. V. Saveliev, M. V. Kanzyuba, "You have full text access to this content Bulk and surface-enhanced Raman spectroscopy of nitrogen-doped ultrananocrystalline diamond films," Phys. Status, Solidi A, vol. 203, 3028, (2006)
- [A.30] V. Baranauskas, B. B. Li, A. Peterlevitz, M. C. Tosin, and S. F. Durrant "Nitrogen-doped diamond films," J. Appl. Phys., Vol. 85, 7455 (1999)

[A.31] Ying Dai, Dadi Dai, Cuixia Yan, Baibiao Huang, and Shenghao Han "N-type electric conductivity of nitrogen-doped ultrananocrystalline diamond films," Phys.

Rev. B, vol.71, 075421, (2005)

[A.32] Igor I. Vlasov, Amanda S. Barnard, Victor G. Ralchenko, Oleg I. Lebedev, Mikhail V. Kanzyuba, Alexey V. Saveliev, Vitaly I. Konov, and Etienne Goovaerts

"Nanodiamond Photoemitters Based on Strong Narrow-Band Luminescence from Silicon-Vacancy Defects," Adv. Mater., vol. 21, 808, (2009)

[A.33] G. Davies and M. F. Hamer, "Optical Studies of the 1.945 eV Vibronic Band in Diamond," Proc. R. Soc. Lon. Ser.-A, vol. 348, 285, (1976)

[A.34] Y. Mita, "Change of absorption spectra in type-Ib diamond with heavy neutron irradiation," Phys. Rev. B, vol. 53, 11360, (1996)

[A.35] G. Davies, "Charge states of the vacancy in diamond," Nature. vol. 269, 498, (1997).

[A.36] Yoshimi Mita, "Change of absorption spectra in type-Ib diamond with heavy neutron irradiation," Phys. Rev. B, vol. 53, 11360 (1999)

[A.37] K.-M. C. Fu, C. Santori, P. E. Barclay, and R. G. Beausoleil, "Conversion of neutral nitrogen-vacancy centers to negatively charged nitrogen-vacancy centers through selective oxidation," Appl. Phys. Lett., vol. 96, 121907, (2010)

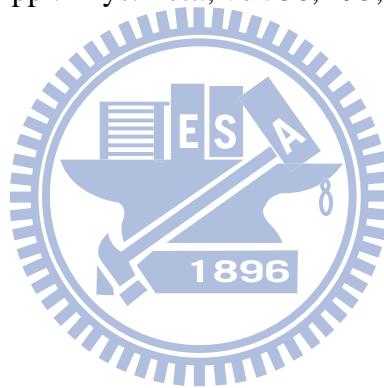
[A.38] C. Santori, P. E. Barclay, K.-M. C. Fu, and R. G. Beausoleil, "Vertical

distribution of nitrogen-vacancy centers in diamond formed by ion implantation and annealing," Phys. Rev. B, vol. 79, 125313, (2009)

[A.39] L. Rondin, G. Dantelle, A. Slablab, F. Grosshans, F. Treussart, P. Bergonzo, S. Perruchas, T. Gacoin, M. Chaigneau, H.-C. Chang, V. Jacques, and J.-F. Roch.

"Surface-induced charge state conversion of nitrogen-vacancy defects in nanodiamonds," Phys. Rev. B, vol. 82, 115449, (2010)

[A.40] J. Ruan, W. J. Choyke, W. D. Partelow, "Si impurity in chemical vapor deposited diamond films," Appl. Phys. Lett., vol. 58, 295, (1991)



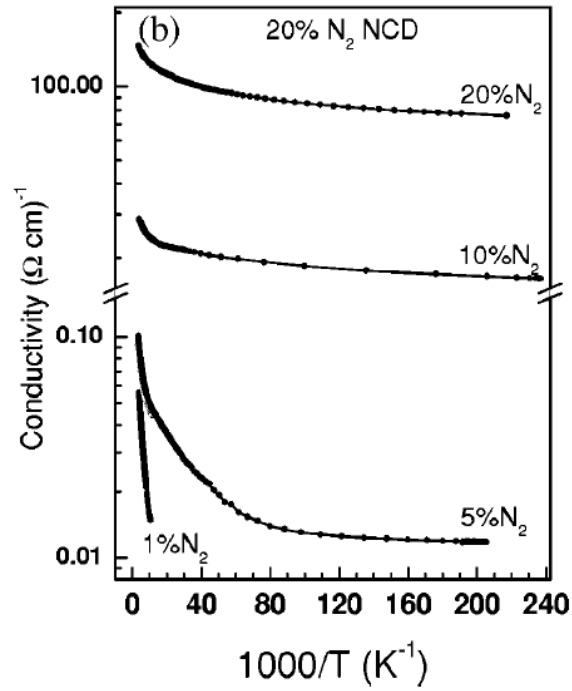


Figure A-1: Conductivity data obtained in the temperature range 300–4.2 K for a series of films synthesized using different nitrogen concentrations. [A.6]

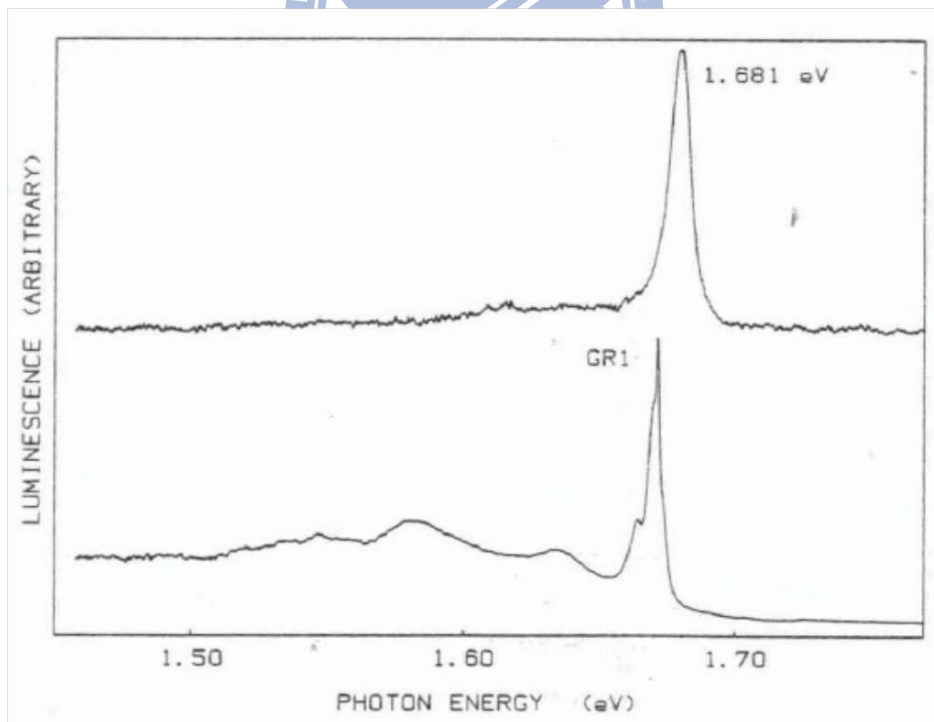


Figure A-3: Silicon vacancies generated by ion implantation [A.21]

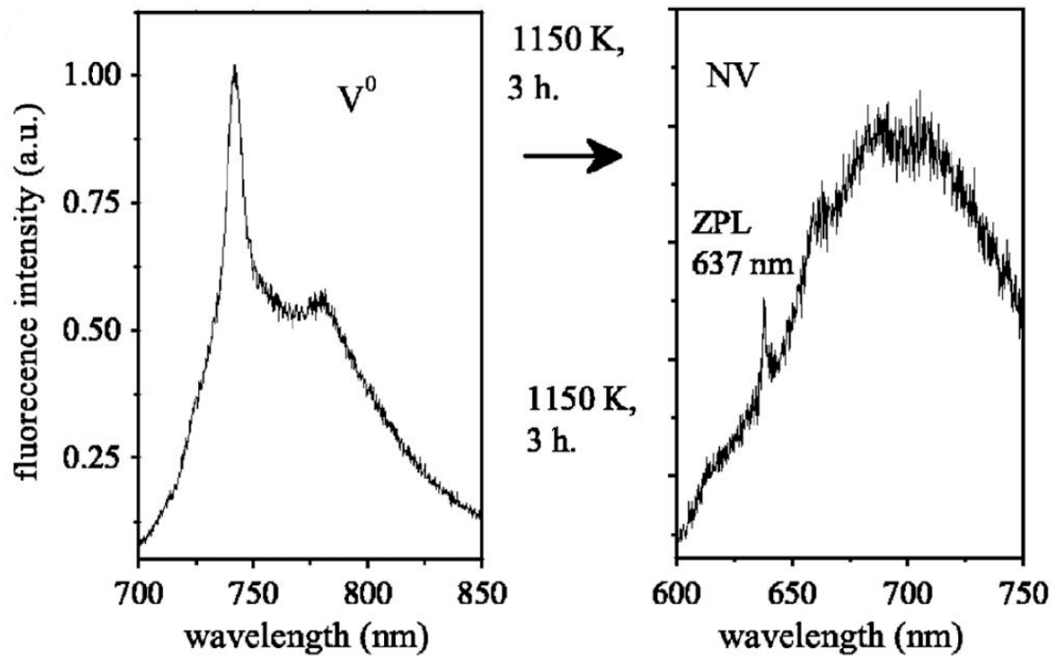
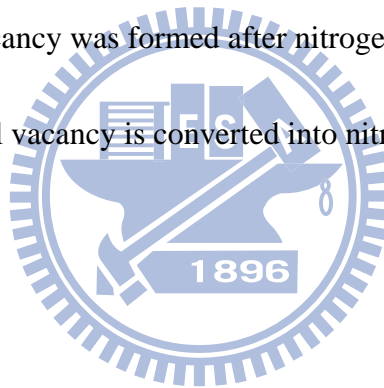


Figure A-3: Neutral vacancy was formed after nitrogen ion implantation. Then annealing the neutral vacancy is converted into nitrogen vacancy. [A.20]



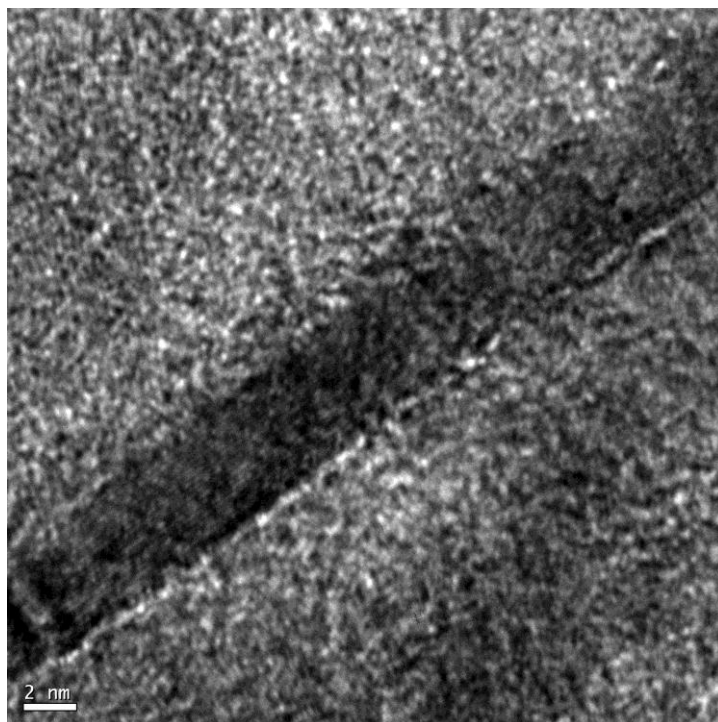


Figure A-4: HRTEM image of the N-doped UNCD

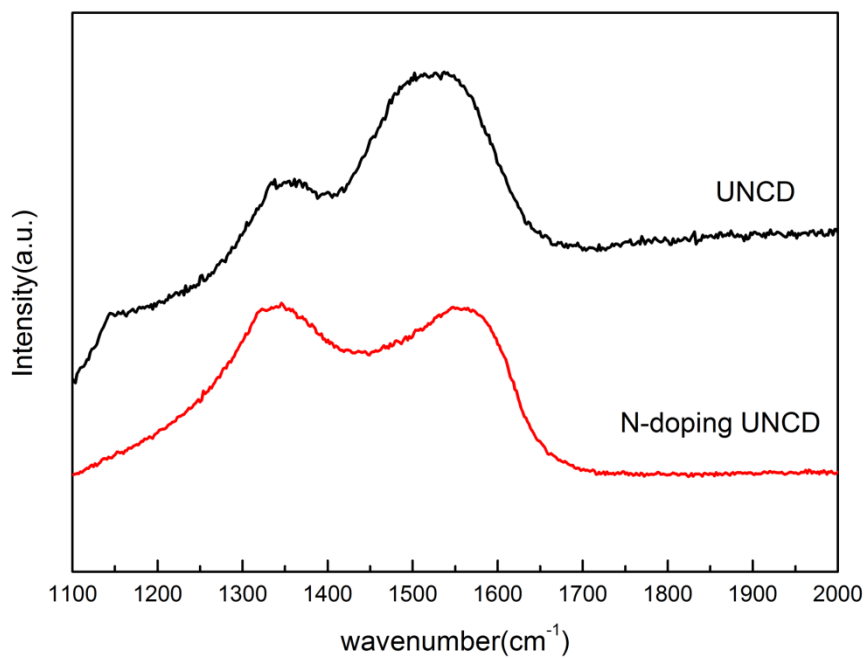


Figure A-5: Raman spectra of UNCD and nitrogen doping UNCD

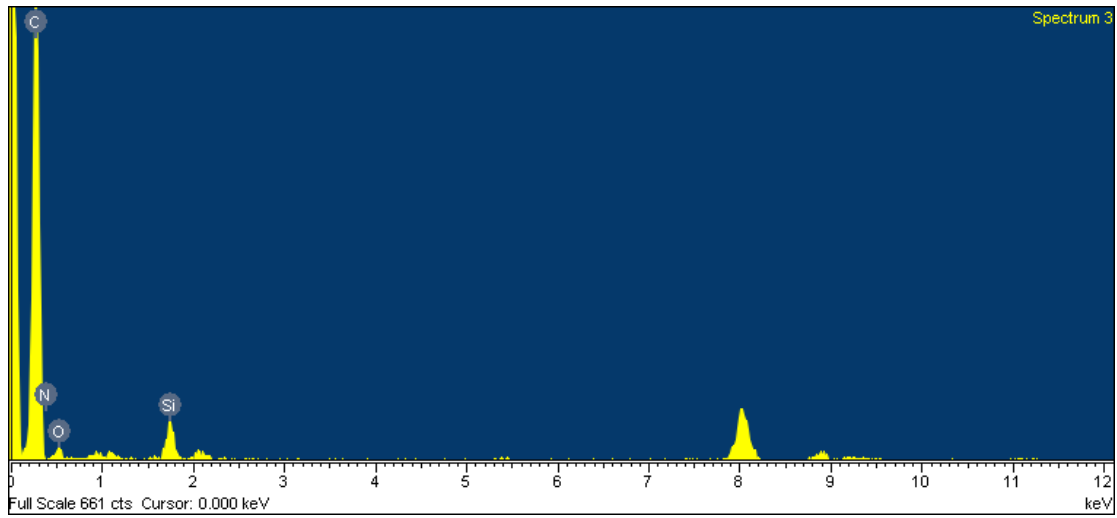


Figure A-6(a): EDS spectrum which the electron beam aims at the grain boundaries

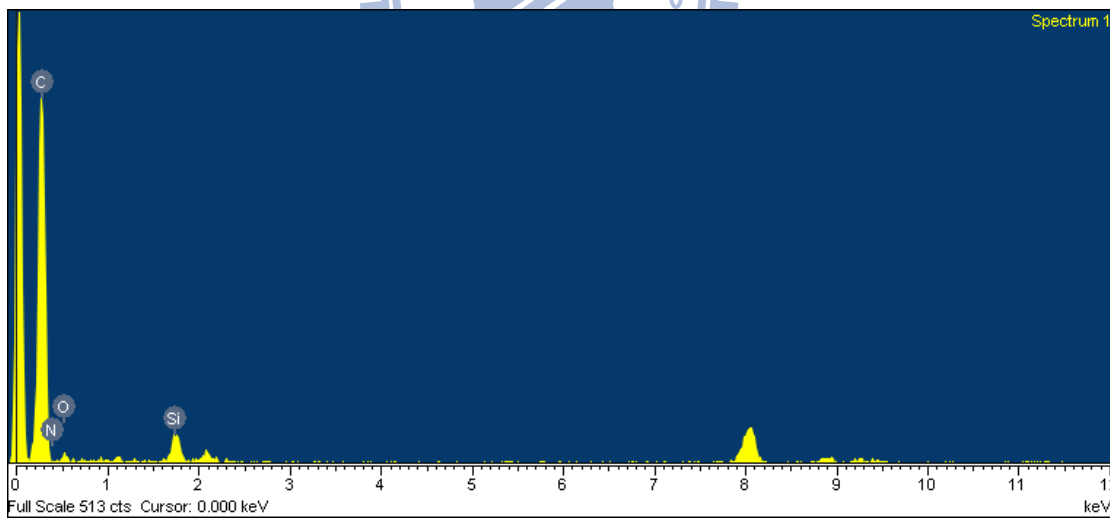


Figure A-6(b): EDS spectrum which the electron beam aims at the grains

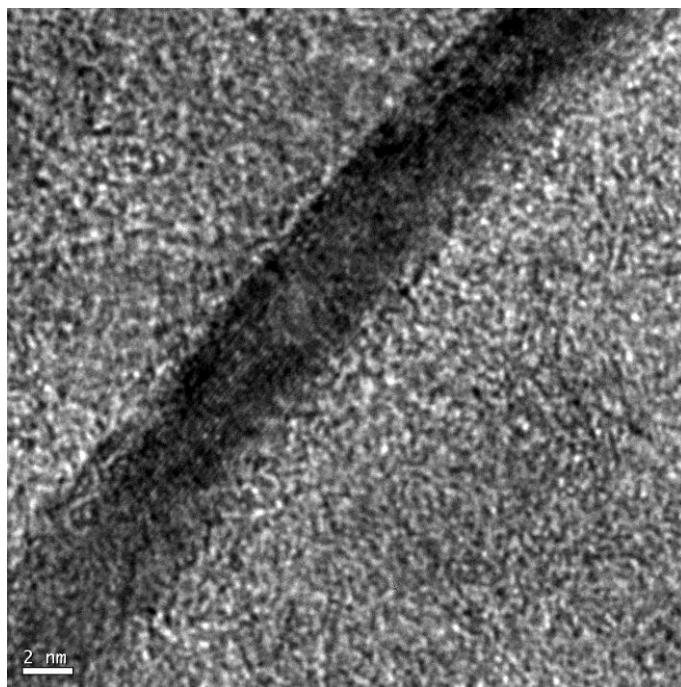


Figure A-7: TEM image of the nitrogen doping UNCD after treated by microwave

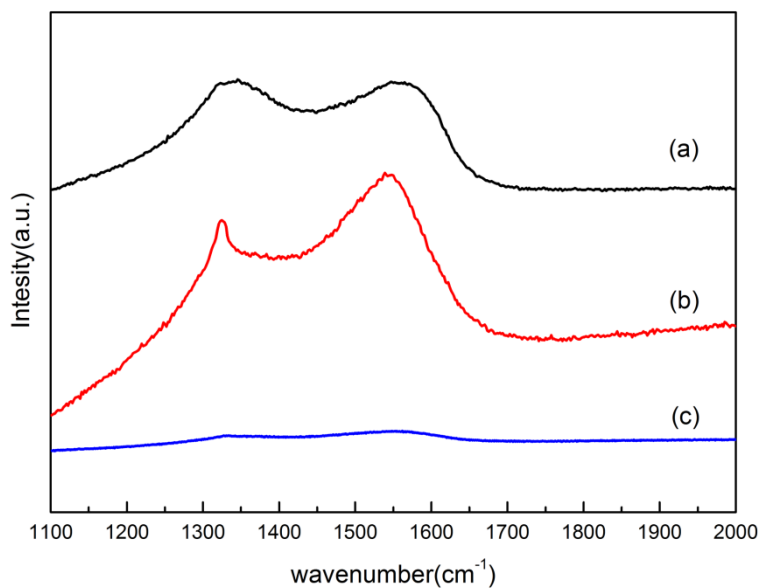
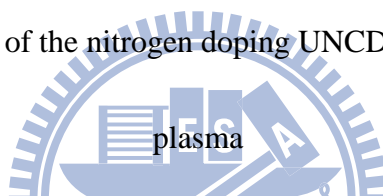


Figure A-8: Raman spectra of (a) nitrogen doping UNCD and nitrogen doping UNCD treated by microwave plasma with (a) microwave power of 800W and total pressure of 10Torr (b) over high microwave power and total pressure

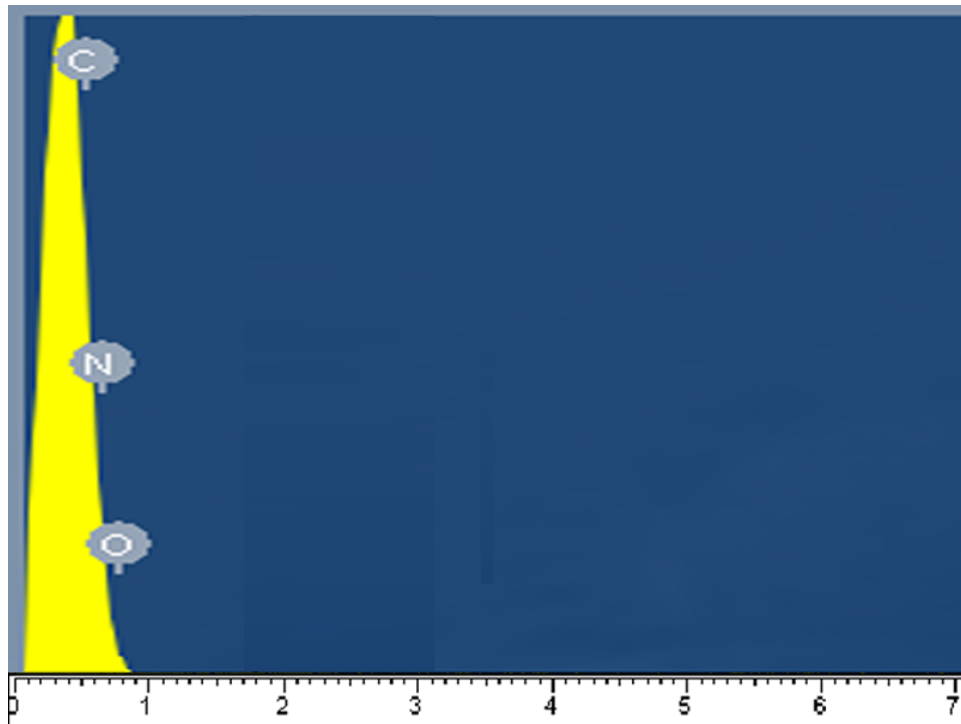


Figure A-9(a): EDS spectrum of sample A

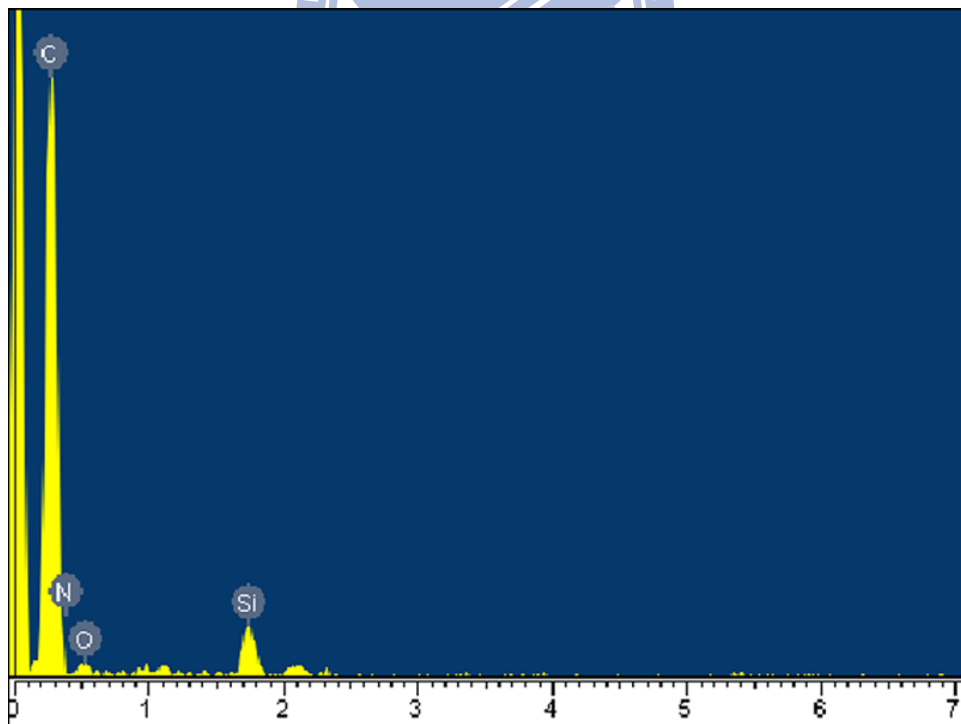


Figure A-9(b): EDS spectrum of sample B

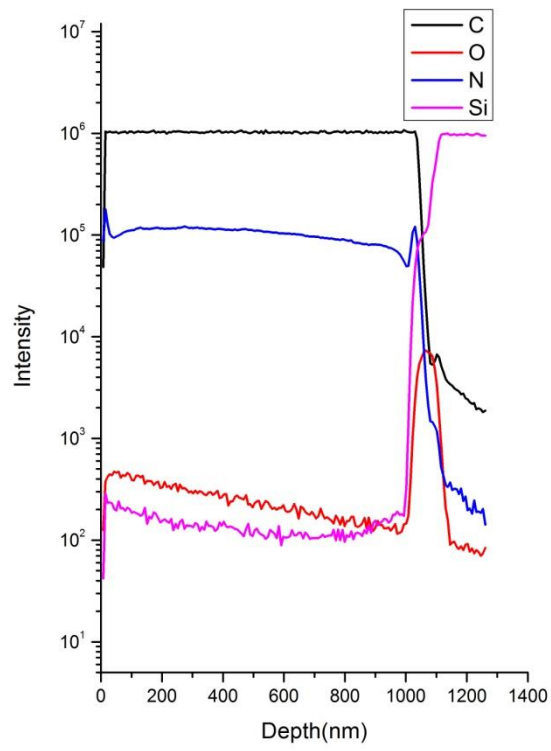


Figure A-10(a): SIMS spectrum of sample A

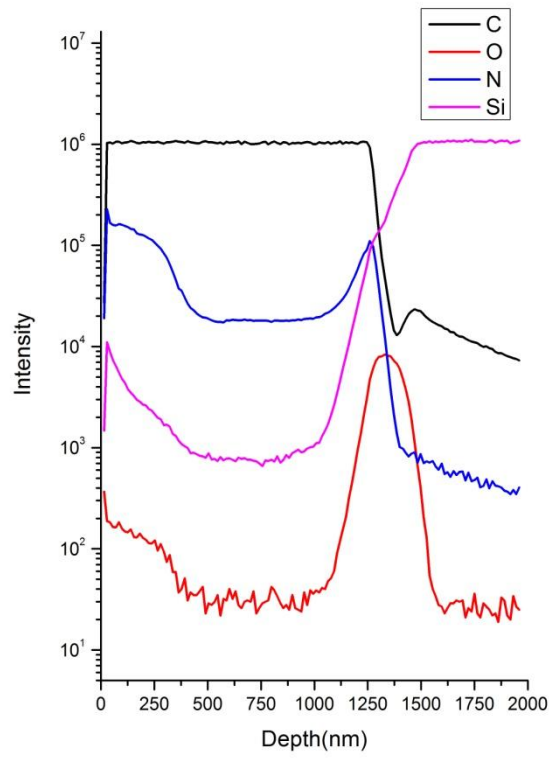


Figure A-10(b): SIMS spectrum of sample B

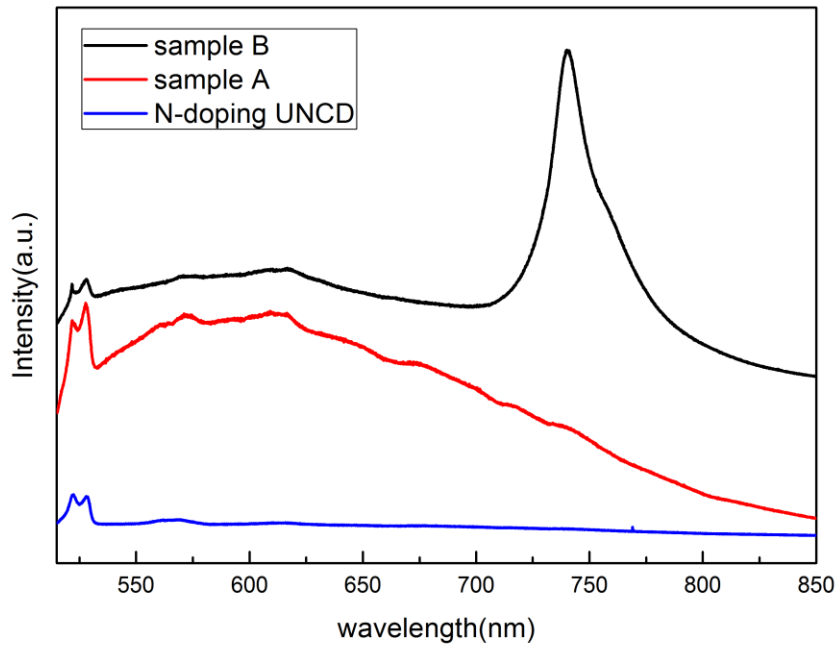


Figure A-11: Photoluminescence spectra of nitrogen doping UNCD, sample A. and sample B which both treated by microwave plasma

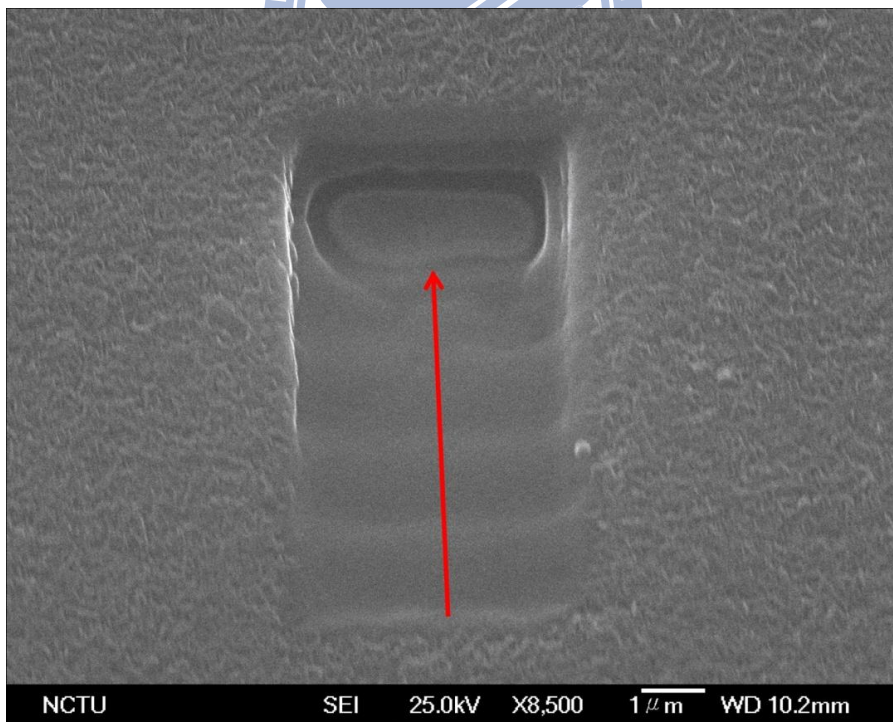


Figure A-12 (a): SEM image of the slope generated by Focus ion beam

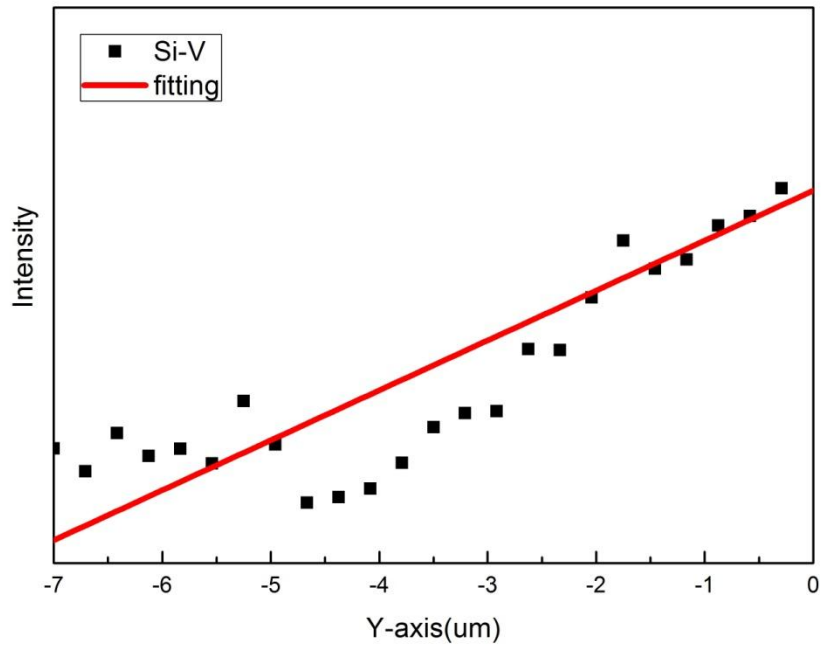


Figure A-12 (b): Photoluminescence intensity of Si-V traced at 738nm

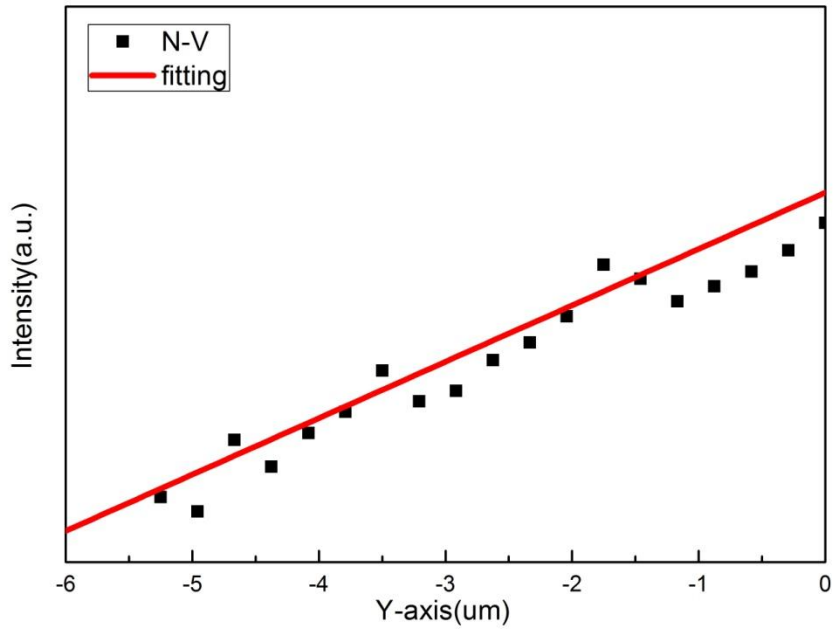


Figure A-12 (c): Photoluminescence intensity of Si-V traced between 550nm and

650nm